UNDERSTANDING AND ADVANCING SHAPE MEMORY IN SEMI-CRYSTALLINE POLYMER NETWORKS

Qiaoxi Li

A dissertation submitted to the faculty at the University of North Carolina at Chapel Hill in partial fulfillment of the requirements for the degree of Doctor of Philosophy in Materials Science in the University of North Carolina at Chapel Hill.

Chapel Hill
2017

Approved by:

Sergei Sheiko

Daphne Klotsa

Rene Lopez

Sean Washburn

Wei You

ABSTRACT

Qiaoxi Li: Understanding and advancing shape memory in semi-crystalline polymer networks
(Under the direction of Sergei Sheiko)

Semi-crystalline polymer networks are widely used as shape memory materials, given that there are two distinctive networks each in charge of a distinctive shape: a chemical network dictating the as-prepared primary shape, and a crystalline scaffold fixing the programmed secondary shape. The two networks are under constant competition, and delicate balance is required to achieve desirable shape memory pathways. One-way irreversible shape memory can be easily realized by fixing the secondary shape upon cooling and recovering back to the primary shape upon complete removal of crystals. However, to achieve two-way reversible shape memory is very challenging for most semi-crystalline elastomers.

We have discovered and established a universal mechanism of reversible shape memory in conventional semi-crystalline elastomers. This mechanism relies on a new partial melting procedure and self-seeding crystallization. At partial melting state, the molten network strands are confined by both the chemical crosslinks and the remaining crystals. Upon cooling, the molten strands undergo self-seeding crystallization, readily restoring the secondary shape. This mechanism can be potentially applied to any types of semi-crystalline elastomers. It enables a novel two-way reversible, free-standing, multiple-times and reprogrammable shape shifting pathway of the conventional irreversible semi-crystalline elastomers.

We have further investigated the effect of various chemical network topologies on reversible shape memory performance. We optimized the reversibility, the repeatability, and durability over time. It is shown that only with sufficient chemical crosslinks (crosslinking densities), would there be enough network confinements to ensure a two-way reversible shape memory behavior.

We have explored new applications using this new mechanism in semi-crystalline elastomers, including a dynamic optical grating. With the primary shape being a flat surface, we programmed grating structure as the secondary shape on the surface. Therefore by applying partial melting and reversible shape memory protocol, we realized a reversible change in grating's height, which result in a reversible change in diffraction intensity. The optical reversibility is sufficiently high (>95%), and can be repeated for many cycles (>10).

So far, most semi-crystalline shape memory elastomers consist of linear network strands. However, there is an intrinsic lower modulus limit for essentially all linear networks, which is on the order of 10^5 Pa. To break this lower boundary, and to better mimic soft biological tissues which are usually on the order of 10^3 Pa, we adopt a new network architecture: bottlebrush network. The resulting modulus change of the semi-crystalline bottlebrush network is unprecedentedly high, covering from GPa at crystalline state, all the way down to kPa or ever lower at amorphous state (six orders of magnitude change). At the rigid state, the material is easy to handle and sharp to penetrate; at the soft state, the material is tunable to mimic the exact modulus of surrounding tissues, even for soft tissues such as brain. We are targeting at two practical applications, brain implant and microneedles drug-delivery.

In all, semi-crystalline polymer networks show great potential as a versatile shape memory material, which can incorporate both one-way irreversible and two-way reversible shape

shifting at the same time. In terms of application, it brings significance in fields such as robotics, actuators, dynamic surface and optics. Also, with the help of bottlebrush network architecture, the semi-crystalline elastomers can possess huge modulus change, which provides a promising candidate for bio-medical implants.

To my friends and family whom I received so much love from.

ACKNOWLEDGEMENTS

There are a lot of people who had given me great help during the course of my PhD study, and who certainly deserve to be acknowledged. First, I would like to thank my mentor Dr. Sheiko with all my heart. Thank you for being a great and passionate scientist who teaches me valuable knowledge and research methodology. Thank you for being a wise advisor who guides me through puzzles and obstacles. Thank you for being a generous friend who constantly helps me, inspires me and supports me. I will be forever thankful to your mentorship. Also, I'd like to thank all Sheiko group members for your kind help and company. Especially, I want to thank Mohammad for believing in me when I doubt myself. Thank you for your rich knowledge, unconditional trust and "let's we do it" golden friendship. Also, I want to thank Maria for always being kind and thoughtful to me. Thank you for your warm company and countless lunch-date together. I want to thank Ke Hu, for always being cheerful and zealous. I would also like to thank my committee members for their precious guidance throughout the years. Moreover, I want to express my sincere gratitude to CFN scientists Dmytro and Oleg at Brookhaven National Lab, thank you for your kind help and sense of humor. I also want to acknowledge CHANL staff Amar for his help. I would also like to thank all my friends and family. Miao Lei, thank you for being such a nice roommate and my friend of life. Xuan, Xiaomeng, Lu Lu, thank you for your warm friendship and company. Specially, I want to thank my husband, Rulin, thank you for your love, trust, faith, encouragement and support all these years. And my parents, thank you for providing me with endless care and love. Thank you for standing by my side.

TABLE OF CONTENTS

LIST OF TABLES

LIST OF FIGURES

LIST OF ABBREVATIONS AND SYMBOLS

AFM	Atomic force microscopy
$CHCl_3$	Chloroform
CH_2Cl_2	Dichloromethane
DBTDL	Dibutyltin dilaurate
DEAP	2, 2-diethoxyacetophenone
DMA	Dynamic mechanical analysis
DSC	Differential scanning calorimetry
FWHM	Full-width-at-half-maximum
NMR	Nuclear magnetic resonance spectroscopy
OA	Octyl adipate
OR	Optical reversibility
PCL	Poly(ε-caprolactone)
PDMS	Polydimethylsiloxane
POA	Poly(octyl adipate)
PTFE	Polytetrafluoroethylene
RSM	Reversible shape memory
SAXS	Small angle X-ray scattering
SM	Shape memory
SMP	Shape memory polymer
THF	Tetrahydrofuran
WAXS	Wide angle X-ray scattering

Xlink	Crosslink
G	Shear modulus
E	Young's modulus
DP (*n*)	Degree of polymerization
T	Temperature
f	Branching functionality of network crosslinks
ν	Crosslinking density
λ	Extensibility
M_x	Molecular weight of network strand between network crosslinks
ϕ	Crystallinity
ΔH	Enthalpy
L (in Xray)	Long period
L	Length
ε_p	Programming strain
ε_0	Initial strain
ε_f	Fixed strain
ε_r	Recovered strain upon complete melting
ε_i	Intermediate strain at partial melting
ε_{rev}	Reversed strain upon cooling in RSM
γ	Strain recovery rate
T_m	Melting peak temperature
T_c	Crystallization peak temperature

T_g	Glass transition temperature
T_p	Partial melting temperature
δ	NMR shift

CHAPTER 1: SHAPE MEMORY AND DISCOVERY OF REVERSIBLE SHAPE MEMORY IN SEMI-CRYSTALLINE ELASTOMERS[1]

1.1 Significance in shape memory polymers (SMPs)

Desirable and functional shapes play an essential role in the properties of objects and devices, dominating aesthetics design, mechanical engineering, and even our daily life. As new generation of technologies and markets evolves, materials are no longer needed to be static, but instead to be expected to carry dynamic functions and properties upon environmental cues. Especially, dynamic shape change plays a crucial role in the development of motion-generating devices, such as robotics. There are many systems that can shift shape in response to changes in temperature, pH, magnetic field, or irradiation.[1-11] For example, gel swelling; thermal expansion. However, these shape-shifts usually follow an intrinsic pathway, from shape A to B, with neither A nor B being able to be altered after synthesis. This fixed pathway significantly limits materials practical applications.

In order to achieve programmable shape shifting, tremendous amount of efforts have been made to develop shape memory polymers (SMPs). In general, SMPs possess a primary shape (B) dictated by synthesis, and unlimited programmable secondary shapes (A, A', A''…). Upon triggered, the shape shifting process can occur in multiple pathways, from A to B, from A' to B, or from A'' to B. The development in SMPs widens materials applications greatly. For

[1]This chapter previously appeared as an article in Macromolecules. The original citation is as follows: J. Zhou, S. A. Turner, S. M. Brosnan, Q. Li, J. Y. Carrillo, D. Nykypanchuk, O. Gang, V. S. Ashby, A. V. Dobrynin and S. S. Sheiko, Shapeshifting: Reversible Shape Memory in Semicrystalline Elastomers. *Macromolecules*, **2014**, 47, 1768−1776.

example, in biomedical applications, Lendlein *et al* have developed heat-sensitive biodegradable SMPs as wound-closing sutures.[12] Behl *et al* fabricated heat-sensitive SMP 2D sheets which fold into 3D cubic for aerospace applications.[13] Xie *et al* demonstrated multiple shape memory by use of a broad glass transition, with multiple shapes that can be memorized and recovered sequentially upon melting.[14] These functional shape shifts can be realized in the same object due to SMPs outstanding programmability in their shape-shifting pathways.

In order to fix a programmed secondary shape, it is necessary to have a second network that is stronger than the primary network. There are different mechanisms that have been developed. For example, semi-crystalline polymers employ a crystallites scaffold;[15-18] glassy polymers employ glass transition;[14] hydrogel polymers utilize phase transition, pH or ionic interactions.[4, 9-10, 19] In this dissertation, we will only focus on the semi-crystalline type of SMPs. Shape memory semi-crystalline polymer networks have a synthetically tunable combination of chemical and physical networks, wherein each network is designed to secure a different shape. Chemical crosslinks hold the memory of the primary shape (Figure 1c), while the physical network of crystallites constructs a scaffold which fixes the programmed secondary shape (Figure 1a). Upon complete melting of the crystalline scaffold, the secondary shape would recover to primary but cannot reverse back to the secondary shape. Therefore, a major bottleneck for most semi-crystalline SMPs is the irreversibility in their shape shifting process. After a single shape transition, the 'memory' is lost and additional programming is required.

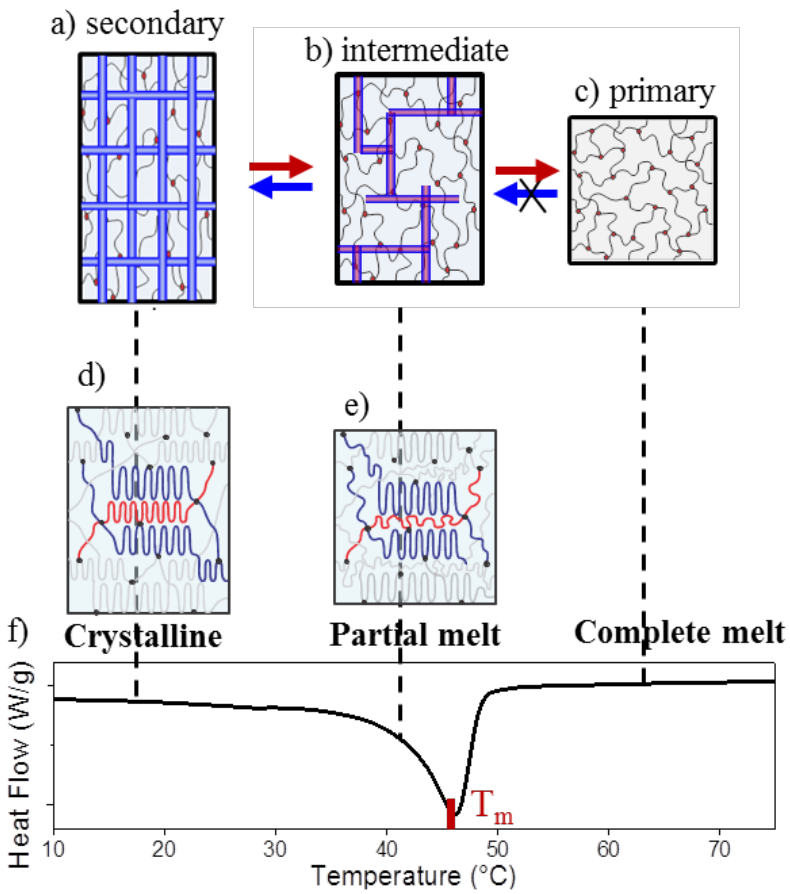

Figure 1.1 Macroscopic shape and mesoscopic crystalline scaffold transformations. a) A programmed secondary shape was fixed by a percolated crystalline scaffold. **b)** Upon heating to a partial melt state, crystals start to melt partially, leaving behind remaining crystals serving as a template for self-seeding recrystallization. Upon cooling, Even though network relaxation is favored thermodynamically, crystallization of cross-linked strands follows kinetically preferred pathways imposed by the partially molten scaffold of the programmed shape. The intermediate shape at partial melt state can reverse back to the programmed shape, enabling RSM. **c)** At complete amorphous state, the primary shape can be recovered. **d)** and **e)** show the mesoscopic self-seeding crystallization process. At partial melt state **e)**, the molten chains (shown in red) are confined by remaining crystallites and chemical crosslinks, therefore upon cooling, the molten chains recrystallize back to its original scaffold **d)**, restoring the macroscopic shape. **f)** A DSC curve shows the melting transition: from crystalline state, to a partial melt state, then to a complete melt state. T_m is the position of the melting peak.

1.2 Discovery of reversible shape memory (RSM) in semi-crystalline SMPs

In order to conquer the irreversible challenge, new materials and strategies have been developed recently. For example, composites built of oppositely strained elements,[20] liquid-crystal elastomers with synthetically encoded alignment of mesogens [21-25] and mechanically assisted SMPs.[18, 26-27] Our research group has discovered a new mechanism of a conventional semi-crystalline elastomers. These elastomers are found to be irreversible, however, by applying a unique protocol, we have shown reversible shape memory (RSM), without applying any external force or additional synthetic modification.[28-30] This behavior is ascribed to counteraction of thermodynamic-driving relaxation of strained polymer chains in the partial-melt phase (Figure 1.1b and 1.1e) and kinetically-preferred pathways self-seeding crystallization in a confined cross-linked network (Figure 1.1d). The detailed mechanism will be discussed later. This new mechanism of semi-crystalline SMPs allows the reversible shape shifting and greatly expands the range of practical applications such as actuators, artificial muscles, hands-free packaging and haptic robots.[13, 23, 31-32]

1.3 Mechanism of semi-crystalline RSM

Traditionally, polymer crystallites have been viewed as mechanical constructs embedded in amorphous networks that hold a temporary shape. And, those morphological constraints merely disappear on melting. We have reconsidered this simple picture of semi-crystalline elastomers and demonstrate that the network of crystallites plays an essential steering role in shape-memory behavior. In addition to counterbalancing the entropic elasticity of the amorphous network, crystallites encode an architectural scaffold within the semi-crystalline polymer. Reversibility of shape transformations is achieved through partial melting of this scaffold,

leaving a latent template behind, that in turn, causes recovery of the original shape on cooling by steering crystallization to replicate the scaffold. By controlling the melting and recrystallization processes, we can shift and expand the reversibility range without the need to change the elastomer's chemical structure. Our strategy integrates two different shape memory (SM) behaviors: conventional one-way SM, two-way reversible SM. Details will be discussed in the next chapter.

1.4 Synthesis of poly(octylene adipate) (POA) elastomers

To prove this concept and demonstrate its universality, we have synthesized a series of poly(octylene adipate) (POA) semi-crystalline elastomers with systematically varied degree of crosslinking (ν) and melting temperature (T_m).[33] Chemical structure is shown in Figure 1.2a. A dry flask was charged with adipic acid (3.000 g, 20.53 mmol), 1,8-octanediol (3.242 g, 22.17 mmol), and scandium triflate catalyst (0.303 g, 0.62 mmol). The flask was nitrogen purged before heating the reaction to 80 °C. After 5 h, vacuum was lowered slowly to 40 torr, and remained at that pressure for 24 h at which time it was pulled to 3 torr for an additional 6 h. The polymerization was terminated by dissolving the polymer in $CHCl_3$, filtering, and precipitating in cold methanol (-78 °C). Final yield was 4.378 g (DP=10, M_n=2563 g/mol) of white solid. Endgroup functionalization was performed according to procedures described elsewhere.[34]

To fabricate semi-crystalline POA elastomers, endcapped POA (1.500g, 0.55 mmol) was mixed with 1mL chloroform in a dry vial, then a drop (~0.2 μL) of 2,2-diethoxyacetophenone was added into the mixture. The vial was vortexed for 1min then sonicated for 0.5 h. The mixture was poured into the mold and UV exposed for 5 min. Then the thermoset elastomer was taken out of the mold and put in the oven (70 °C, 20 torr) overnight. Materials properties are summarized in (Table 1.1).

Table 1.1 Material properties of POA polymers.

Sample	n [a]	T_m (°C) [b]	H_m (J/g) [b]	$E_{80\,°C}$ (MPa) [c]	ν (mol/m^3) [c]	gel% [d]
1	6.3	23	21	7.9	900	0.99
2	10.0	44	34	7.1	790	0.97
3	11.1	47	44	5.3	610	0.97
4	12.5	41	41	5.4	620	0.98
5	13.3	50	55	4.2	470	0.98
6	20.0	59	70	1.5	170	0.93

[a] Determined by NMR. [b] Determined by DSC, second heat, 5 °C/min. [c] Young's modulus, determined by tensile test from DMA, frequency of 1 Hz. Crosslinking density is calculated by $\nu = E/3RT$. [d] Determined by Soxhlet extractor, $CHCl_3$ as the extracting solution, extraction time is 24 h and solvent is evaporated in vacuum oven for 24 h. Gel fraction is calculated using $G = m_d/m_0$, m_d is the weight of sample after washing and drying, m_0 is the initial weight.

1.5 Results and discussion

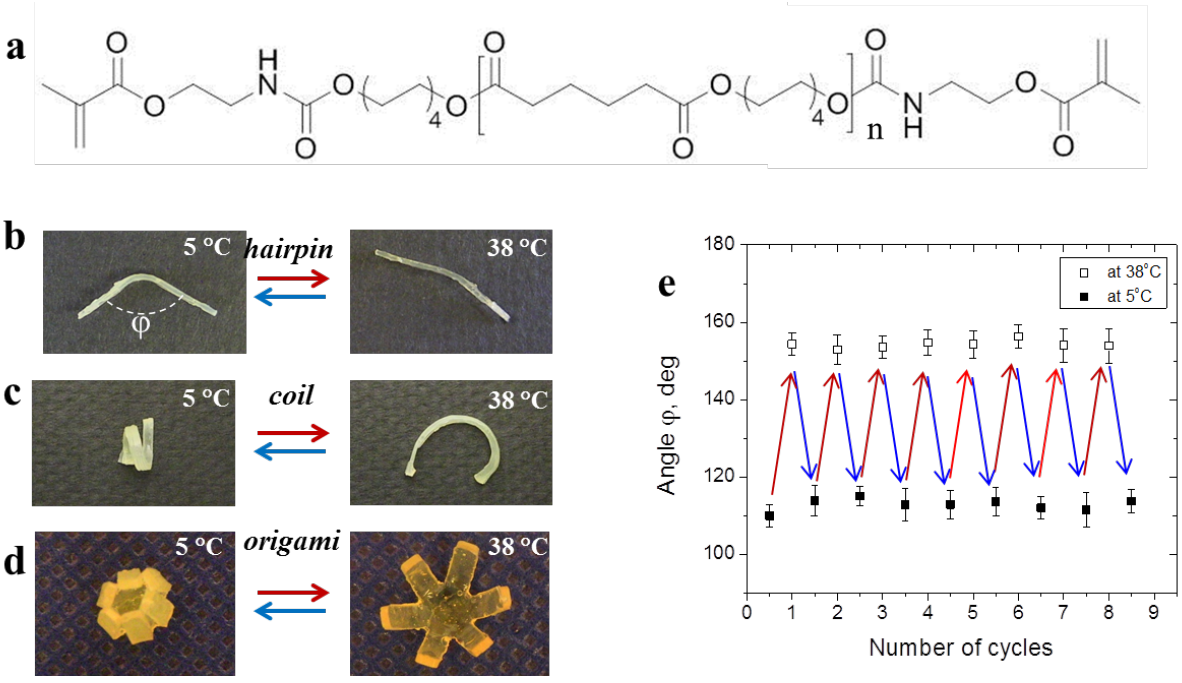

Figure 1.2 Macroscopic shape and mesoscopic crystalline scaffold transformations. a) Chemical structure of poly(octylene adipate) (POA) oligomers used for the synthesis of shape-memory elastomers. Their crosslinking density was controlled by varying the degree of

polymerization n of the oligomers, i.e. polymeric strands. **b-e)** Examples of two-way reversible shape memory demonstrated for three different shape transformations upon heating to 38 °C and subsequent cooling to 5 °C. **e)** Reversible oscillations of the hairpin angle in b during eight consecutive heating-cooling cycles within the 5-38 °C range.

All POA elastomers demonstrate conventional one-way irreversible SM observed upon complete melting. This behavior is relatively well understood.[16, 35] Figure 1.2 shows an experimental demonstration of RSM concept using sample #2 in Table 1.1. In Figure 1.2 b, a straight bar of the semi-crystalline POA elastomer was programmed as a hairpin temporary shape by deforming the sample at 60 °C and then fixing it by crystallization at 5 °C. Subsequent heating to 38 °C and cooling to 5 °C resulted in reversible shape transformations of the hairpin between 115° and 155° angles, which occurred spontaneously without applying any external force. The angle oscillations were highly repeatable: upon consecutive heating and cooling cycles, the sample shape changed reversibly multiple times without losing memory of both angular shapes (Figure 1.2 e). Similar reversible behavior was accomplished for a polymer coil (Figure 1.2 c) and for the folding–unfolding of origami-like polymer sheets (Figure 1.2 d). Note that the upper temperature 38 °C corresponds to partial melting of the crystalline phase as shown in Figure 1.3. As discussed below in more detail, partial melting allows for memory of the temporary shape to be preserved, so it may be restored upon subsequent cooling and recrystallization.

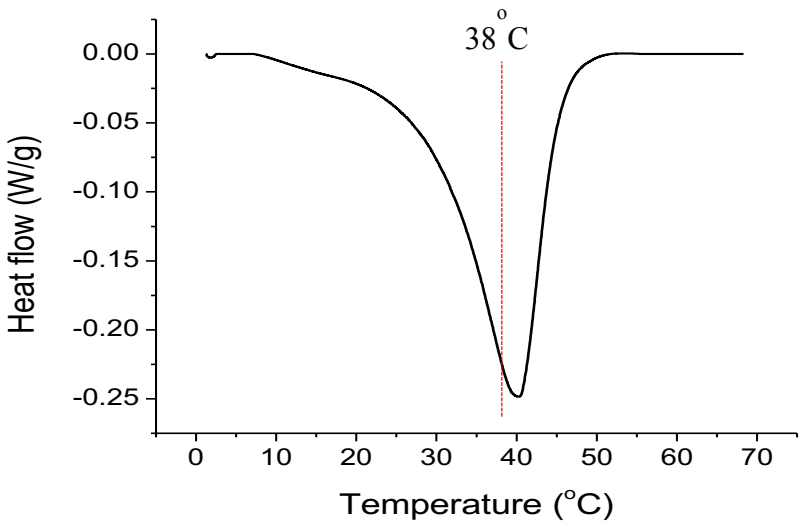

Figure 1.3 Melting of POA semi-crystalline elastomers (sample #2). Second heating curve of POA sample from DSC measurement, heating and cooling rate of 5 °C/min. At 38°C the sample #2 was only partially melted.

To achieve RSM, an experimental protocol with partial melting has been adopted, as shown in Figure 1.4. Three equations are used to investigate RSM performance:

$$Fixation\ ratio = \frac{\varepsilon_f}{\varepsilon_p} \quad (1)$$

$$Recovery\ ratio = \frac{\varepsilon_r - \varepsilon_f}{\varepsilon_0 - \varepsilon_f} \quad (2)$$

$$Reversibility = \frac{\varepsilon_{rev} - \varepsilon_i}{\varepsilon_f} \quad (3)$$

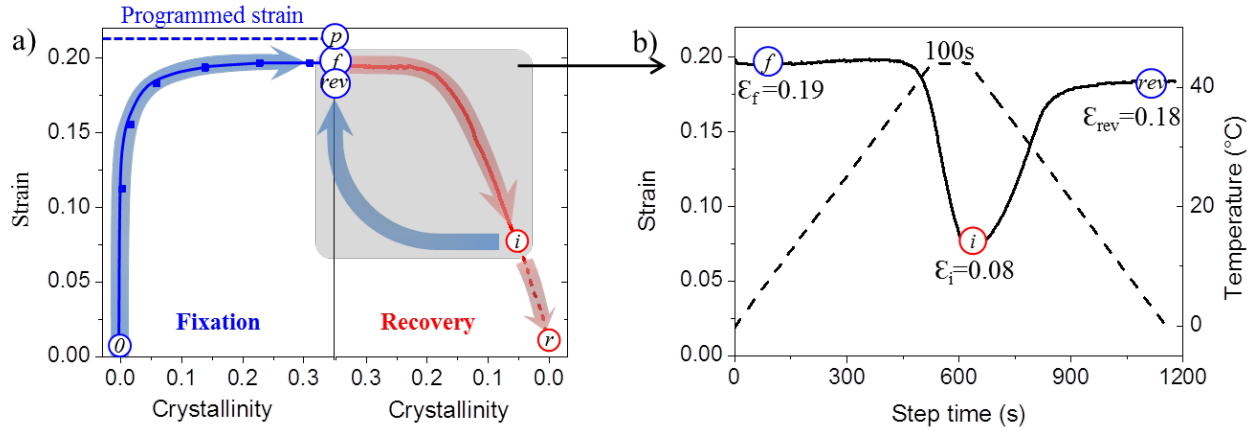

Figure 1.4 Experimental protocol. a) Shape programming, fixation, and recovery. A programing strain of ε_p = 20% (dashed blue line) is applied at 80 °C and then fixed by quenching to 0 °C. Each data point in the fixation panel corresponds to a strain fixed by quenching at a given stage of the crystallization process. A percolated crystalline scaffold is developed. Crystals in black color indicate early stage (critical) in fixation, blue color indicate the rest 'redundant' crystals in fixation. At final stage of fixation, sample is fixed to the programmed strain ε_p. Upon melting, the crystalline scaffold is melted into percolated clusters. At any stage of the melting process, heating can be switched to cooling and reverse the shape transformation from ε_i to ε_r. **b)** After programming, a sample with programmed strain ε_p is heated to $T_{partial}$ (ε_i). Upon cooling, strain returns to ε_{rev}.

Starting with a completely molten sample, we applied uniaxial programming strain ~20% (ε_p) and upon cooling, crystallization occurs and crystallinity increases. As crystallinity increases, more programmed strain can be fixed. In fact, around 5% crystallinity, the fixation ratio is already sufficiently high >80%. Upon reaching to the maximum crystallinity ~35%, more than 95% of the programmed strain can be fixed. At this state, the sample is at its secondary shape (ε_f) (corresponds to Figure 1.1a). Upon subsequent heating of the sample, the secondary shape starts to melt partially, with a tendency to recover towards its primary shape, which leads to sample contraction to ε_i (corresponds to Figure 1.1b). From this state, the sample can be

further altered in two different ways. First, we can continue heating the sample to complete the melting process and reach nearly 100% recovery of the original shape (ε_r) along with complete relaxation of the strained chemical network (corresponds to Figure 1.1c). This process is conventional one-way SM, which is irreversible. Second, we can cool the sample to prompt recrystallization of the molten polymer strands confined between the latent crystallites. This step causes two-way reversible elongation to ε_{rev}, which can be repeated multiple times similar to the shape transformations displayed in Figures 1.2b-d. Here, the crystallites serve both as seeds and templates for recrystallization, restoring the architectural scaffold of the secondary shape.[36-37] The reversibility of the SM processes depends greatly on the extent of melting, i.e. the temperature reached within the melting interval (Figure 1.4b). This dependence has been thoroughly studied for all synthesized materials (Figure 1.5). With increasing $T_{partial}$, the reversibility or the contribution of $(\varepsilon_{rev} - \varepsilon_i)$ first increases, reaching a maximum at $T_{partial} = T_m$ (T_m is the melting peak determined from a DSC curve, such as in Figure 1.1f), and then decreases to zero. This can be explained from the aspect of chemical network and crystalline scaffold competition. At around T_m, there are sufficient amount of crystals becoming molten, releasing network strands to recover and contract towards sample's primary shape, meanwhile, there are still enough crystals leaving behind, providing seeds and templates to restore the original crystalline scaffold upon cooling. Only at a balanced point, which is proven to be near T_m, can a sample reach its maximum capability to be reversible.

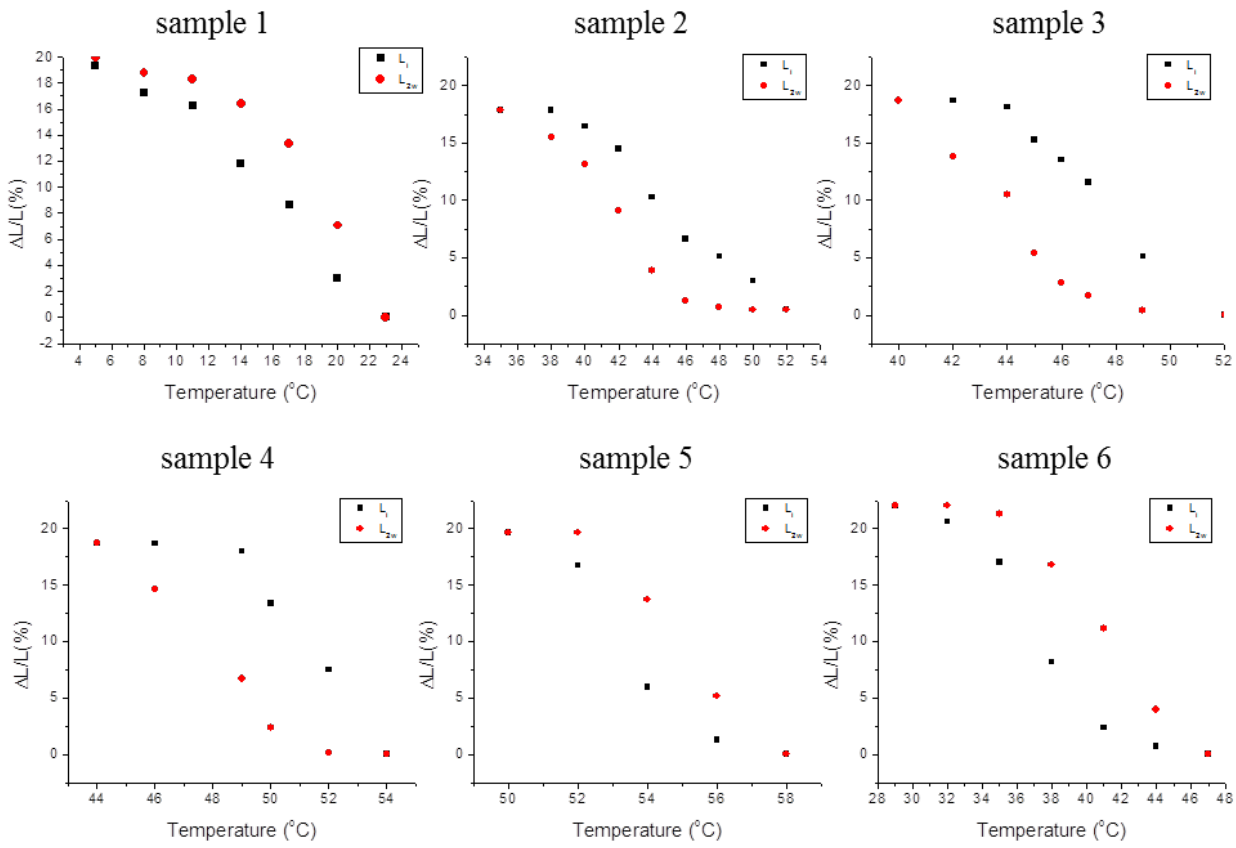

Figure 1.5 Reversibility at different partial melting temperatures $T_{partial}$. For all six samples, the maximum reversibility were found near the peak position of melting transition T_m. Lower or higher than T_m, the reversibility would decreased correspondingly.

After discussing the melting temperature effect, we shall then discuss the effect of crosslinking densities of POA elastomers. To understand this issue in a quantitative fashion, each of six samples' maximum reversibility is plotted against their crosslinking densities (Figure 1.6). In general, chemical crosslinks have a dual effect on shape-memory properties: First, the elastic modulus of an elastomer increases with crosslinking density, and a higher modulus favors recovery of the original shape upon melting. Second, chemical crosslinks frustrate the crystallization process and lower the degree of crystallinity, hence, impeding the ability of crystallites to encode the temporary shape. The result of these competing effects is demonstrated

in Figure 1.6, which shows maximum reversibility increasing up to almost 70% as the crosslinking density reaches ca. 700 mol/m^3 followed by a decline for strongly cross-linked samples. The initial increase in reversibility is due to enhancement of the templating effect of the latent crystallites: molten polymer strands in strongly crosslinked elastomers exhibit slow relaxation and upon heating, they largely remain in place, and thus they are available to template recrystallization (on typical experimental time scales $t < 1\ h$). The decrease in reversibility in strongly crosslinked materials is simply due to the inability of sparse crystallites to secure a temporary shape due to the lack of percolation of the crystalline domains across the sample.

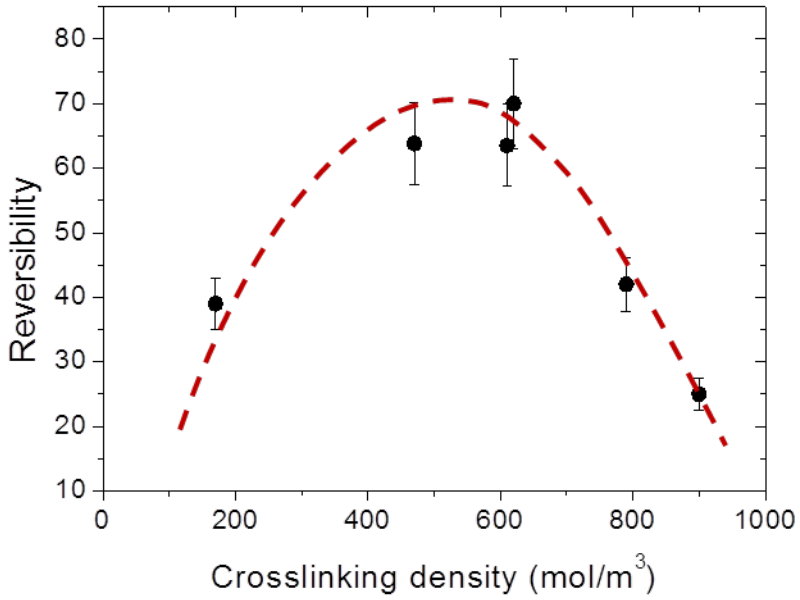

Figure 1.6 Trend of maximum reversibility with crosslinking densities. The maximum two-way reversible for each sample initially increases with crosslinking density, reaching a maximum value of ca. 70% at $\nu \cong 600$ mol/m^3 (sample #3 and #4) and then decreases in highly crosslinked samples. Dashed line is drawn to show a trend.

1.6 Application of RSM as robotic gripper

As mentioned in the introduction, reversible shape memory is very appealing for many practical applications. Applications of two-way reversible SMPs are quite straight forward and in line with other stimuli responsive systems like hydrogels and electrically active polymers.[4, 38-39] The advantage of shape memory polymers over other shape-responsive systems is the ability to adopt and routinely control complex shapes. An additional advantage of the two-way reversible systems discussed here is their ability to perform a nearly infinite number of shape-transformation cycles completely autonomously, i.e. without application of an external force. The origami in Figure 1.2d, was used as a gripper to move objects between cold (10°C) and warm (36°C) water reservoirs (Figure 1.7), and a complete movie of this process can be viewed online (http://pubs.acs.org/doi/abs/10.1021/ma4023185). The objects varied in mass from 3 to 10 grams, while the gripper was weighed 0.1 g. In other words, the gripper can lift and hold objects that 100 times heavier than itself, i.e. the maximum achieved payload-to-weight ratio is 100, which is higher than many industrial robotic grippers. For example, the payload-to-weight ratio of ROBOTIQ robotic grippers is lower than 5.[17]

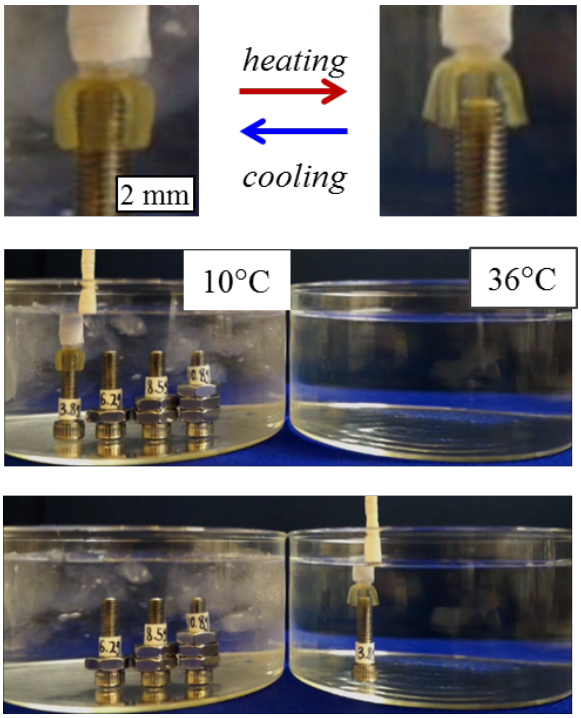

Figure 1.7 Robotic gripper. A soft gripper was designed from a shape-memory polymer which was programmed to perform two-way reversibility. The griper closes and opens during cooling-heating cycles respectively. The gripper was used to move different weights (bolt & nut assemblies) from cold (10 °C) to warm (36 °C) water reservoirs.

1.7 Conclusion and outlook

In summary, we have developed a universal picture of reversible shape memory in semi-crystalline elastomers, which integrates two conceptually different shape memory protocols: (i) one-way irreversible, (ii) two-way reversible shape transformations. Semi-crystalline elastomers with a synthetically tunable combination of chemical and physical crosslinks may be viewed as dual-network materials, wherein each network is designed to secure a different shape. Chemical crosslinks hold the memory of the original shape, while the physical network of crystallites constructs a scaffold of the temporary shape. While thermodynamics drives relaxation of the chemical network towards the original shape, crystallization of confined and constrained

polymer chains is biased towards fastest pathways during cooling guided by the remaining crystallites to the opposite direction. Maximum performance of each individual protocol can be achieved by tuning the crosslinking density and the degree of crystallinity of semi-crystalline elastomers. We have shown that the two-way reversible shape memory behavior is a consequence of interplay between the thermodynamics of the chemical network and kinetics of crystallization within a semi-crystalline elastomer. Further optimization of the reversible shape memory may be achieved by tuning chemical composition and widening the melting temperature interval, but the variety of the RSM behaviors studied obeys the same universal mechanism as discussed above.

1.8 REFERENCES

1. Ono, T.; Sugimoto, T.; Shinkai, S.; Sada, K., Lipophilic polyelectrolyte gels as super-absorbent polymers for nonpolar organic solvents. *Nature materials* **2007,** *6* (6), 429-433.

2. Kobatake, S.; Takami, S.; Muto, H.; Ishikawa, T.; Irie, M., Rapid and reversible shape changes of molecular crystals on photoirradiation. *Nature* **2007,** *446* (7137), 778-781.

3. Mitsumata, T.; Gong, J. P.; Osada, Y., Shape memory functions and motility of amphiphilic polymer gels. *Polymers for Advanced Technologies* **2001,** *12* (1-2), 136-150.

4. Osada, Y.; Matsuda, A., Shape memory in hydrogels. *Nature* **1995,** *376* (6537), 219.

5. Kohlmeyer, R. R.; Javadi, A.; Pradhan, B.; Pilla, S.; Setyowati, K.; Chen, J.; Gong, S., Electrical and dielectric properties of hydroxylated carbon nanotube− elastomer composites. *The Journal of Physical Chemistry C* **2009,** *113* (41), 17626-17629.

6. Thévenot, J.; Oliveira, H.; Sandre, O.; Lecommandoux, S., Magnetic responsive polymer composite materials. *Chemical Society Reviews* **2013,** *42* (17), 7099-7116.

7. Lu, H.; Huang, W.; Yao, Y., Review of chemo-responsive shape change/memory polymers. *Pigment & Resin Technology* **2013,** *42* (4), 237-246.

8. Lendlein, A.; Jiang, H.; Jünger, O.; Langer, R., Light-induced shape-memory polymers. *Nature* **2005,** *434* (7035), 879-882.

9. Ma, C.; Li, T.; Zhao, Q.; Yang, X.; Wu, J.; Luo, Y.; Xie, T., Supramolecular Lego Assembly Towards Three-Dimensional Multi-Responsive Hydrogels. *Advanced Materials* **2014,** *26* (32), 5665-5669.

10. Wu, Z. L.; Moshe, M.; Greener, J.; Therien-Aubin, H.; Nie, Z.; Sharon, E.; Kumacheva, E., Three-dimensional shape transformations of hydrogel sheets induced by small-scale modulation of internal stresses. *Nature communications* **2013,** *4*, 1586.

11. Zhou, J.; Sheiko, S. S., Reversible shape-shifting in polymeric materials. *Journal of Polymer Science Part B: Polymer Physics* **2016,** *54* (14), 1365-1380.

12. Lendlein, A.; Langer, R., Biodegradable, elastic shape-memory polymers for potential biomedical applications. *Science* **2002,** *296* (5573), 1673-1676.

13. Behl, M.; Razzaq, M. Y.; Lendlein, A., Multifunctional Shape-Memory Polymers. *Advanced materials* **2010,** *22* (31), 3388-3410.

14. Xie, T., Tunable polymer multi-shape memory effect. *Nature* **2010,** *464* (7286), 267-270.

15. Xie, T., Recent advances in polymer shape memory. *Polymer* **2011,** *52* (22), 4985-5000.

16. Lendlein, A.; Sauter, T., Shape-Memory Effect in Polymers. *Macromolecular Chemistry and Physics* **2013,** *214* (11), 1175-1177.

17. Pandini, S.; Passera, S.; Messori, M.; Paderni, K.; Toselli, M.; Gianoncelli, A.; Bontempi, E.; Ricco, T., Two-way reversible shape memory behaviour of crosslinked poly (ε-caprolactone). *Polymer* **2012,** *53* (9), 1915-1924.

18. Chung, T.; Romo-Uribe, A.; Mather, P. T., Two-way reversible shape memory in a semicrystalline network. *Macromolecules* **2008,** *41* (1), 184-192.

19. Han, Y.; Bai, T.; Liu, Y.; Zhai, X.; Liu, W., Zinc ion uniquely induced triple shape memory effect of dipole–dipole reinforced ultra-high strength hydrogels. *Macromolecular rapid communications* **2012,** *33* (3), 225-231.

20. Westbrook, K. K.; Mather, P. T.; Parakh, V.; Dunn, M. L.; Ge, Q.; Lee, B. M.; Qi, H. J., Two-way reversible shape memory effects in a free-standing polymer composite. *Smart Materials & Structures* **2011,** *20* (6).

21. Lehmann, W.; Skupin, H.; Tolksdorf, C.; Gebhard, E.; Zentel, R.; Krüger, P.; Lösche, M.; Kremer, F., Giant lateral electrostriction in ferroelectric liquid-crystalline elastomers. *Nature* **2001,** *410* (6827), 447-450.

22. Thomsen, D. L.; Keller, P.; Naciri, J.; Pink, R.; Jeon, H.; Shenoy, D.; Ratna, B. R., Liquid crystal elastomers with mechanical properties of a muscle. *Macromolecules* **2001,** *34* (17), 5868-5875.

23. Shenoy, D. K.; Thomsen III, D. L.; Srinivasan, A.; Keller, P.; Ratna, B. R., Carbon coated liquid crystal elastomer film for artificial muscle applications. *Sensors and Actuators A: Physical* **2002,** *96* (2), 184-188.

24. Ware, T. H.; McConney, M. E.; Wie, J. J.; Tondiglia, V. P.; White, T. J., Voxelated liquid crystal elastomers. *Science* **2015,** *347* (6225), 982-984.

25. Hiraoka, K.; Sagano, W.; Nose, T.; Finkelmann, H., Biaxial shape memory effect exhibited by monodomain chiral smectic C elastomers. *Macromolecules* **2005,** *38* (17), 7352-7357.

26. Li, J.; Rodgers, W. R.; Xie, T., Semi-crystalline two-way shape memory elastomer. *Polymer* **2011,** *52* (23), 5320-5325.

27. Pandini, S.; Baldi, F.; Paderni, K.; Messori, M.; Toselli, M.; Pilati, F.; Gianoncelli, A.; Brisotto, M.; Bontempi, E.; Ricco, T., One-way and two-way shape memory behaviour of semi-crystalline networks based on sol–gel cross-linked poly (ε-caprolactone). *Polymer* **2013,** *54* (16), 4253-4265.

28. Zhou, J.; Turner, S. A.; Brosnan, S. M.; Li, Q.; Carrillo, J.-M. Y.; Nykypanchuk, D.; Gang, O.; Ashby, V. S.; Dobrynin, A. V.; Sheiko, S. S., Shapeshifting: reversible shape memory in semicrystalline elastomers. *Macromolecules* **2014,** *47* (5), 1768-1776.

29. Behl, M.; Kratz, K.; Noechel, U.; Sauter, T.; Lendlein, A., Temperature-memory polymer actuators. *Proceedings of the National Academy of Sciences of the United States of America* **2013,** *110* (31), 12555-12559.

30. Zhou, J.; Li, Q.; Turner, S. A.; Ashby, V. S.; Sheiko, S. S., Isothermal programming of triple shape memory. *Polymer* **2015,** *72*, 464-470.

31. Ashley, S., Artificial muscles. *Scientific American* **2003,** *289* (4), 52-59.

32. Behl, M.; Kratz, K.; Noechel, U.; Sauter, T.; Lendlein, A., Temperature-memory polymer actuators. *Proceedings of the National Academy of Sciences* **2013,** *110* (31), 12555-12559.

33. Brosnan, S. M.; Brown, A. H.; Ashby, V. S., It is the outside that counts: chemical and physical control of dynamic surfaces. *Journal of the American Chemical Society* **2013,** *135* (8), 3067-3072.

34. Yang, Z.; Huck, W. T.; Clarke, S. M.; Tajbakhsh, A. R.; Terentjev, E. M., Shape-memory nanoparticles from inherently non-spherical polymer colloids. *Nature materials* **2005,** *4* (6), 486-490.

35. Heuchel, M.; Sauter, T.; Kratz, K.; Lendlein, A., Thermally induced shape-memory effects in polymers: Quantification and related modeling approaches. *Journal of Polymer Science Part B: Polymer Physics* **2013,** *51* (8), 621-637.

36. Fillon, B.; Wittmann, J.; Lotz, B.; Thierry, A., Self-nucleation and recrystallization of isotactic polypropylene (α phase) investigated by differential scanning calorimetry. *Journal of Polymer Science Part B: Polymer Physics* **1993,** *31* (10), 1383-1393.

37. Xu, J.; Ma, Y.; Hu, W.; Rehahn, M.; Reiter, G., Cloning polymer single crystals through self-seeding. *Nature materials* **2009,** *8* (4), 348-353.

38. Yoshida, R.; Uchida, K.; Kaneko, Y.; Sakai, K.; Kikuchi, A.; Sakurai, Y.; Okano, T., Comb-type grafted hydrogels with rapid deswelling response to temperature changes. *Nature* **1995,** *374* (6519), 240-242.

39. Camacho-Lopez, M.; Finkelmann, H.; Palffy-Muhoray, P.; Shelley, M., Fast liquid-crystal elastomer swims into the dark. *Nature materials* **2004,** *3* (5), 307-310.

CHAPTER 2: ADVANCING REVERSIBLE SHAPE MEMORY BY TUNING THE POLYMER NETWORK ARCHITECTURE[2]

2.2 Introduction and objectives

In the previous chapter, it is shown that due to counteraction of a chemical network and a crystalline scaffold, semi-crystalline polymer networks exhibit a peculiar behavior- reversible shape memory (RSM), which occurs naturally without applying any external force and particular structural design.[1] The goal of the present study is to explore structure-property correlations of semi-crystalline octylene-adipate polymer networks and expand the RSM limits with respect to (i) range of reversible strain, (ii) rate of reversed strain recovery, and (iii) decay of the reversibility with time. For this purpose, we have prepared po1.lymer networks with different topologies, including irregular network, clicked regular network, and loose network with dangles. Additionally, using oligomers with different degree of oligomerizations, we control crosslinking density in a broad range of ca. 50-1000 mol/m^3. While controlling the crosslink density, we ensure that the densest network has sufficient amount of crystals to fix a programmed shape and the loosest network has enough elasticity to recover its original state. In this paper, we show that the RSM properties display significant shifts with increasing crosslink density, whereas network topology does not cause any specific impact on RSM. The crosslink density has dual effect on the network properties. It controls both elasticity of the chemical network, which provides a

[2]This chapter previously appeared as an article in Macromolecules. The original citation is as follows: Q. Li, J. Zhou, M. Vatankhah-Varnoosfaderani, D. Nykypanchuk, O. Gang, S. S. Sheiko, Advancing Reversible Shape Memory by Tuning the Polymer Network Architecture. *Macromolecules*, **2016**, 49, 1383-1391.

restoring force towards the original shape, and dimensions of the crystalline scaffold, which secures memory of the programmed shape. By managing the interplay between the chemical and crystalline networks, we achieved nearly 80% recovery of the programmed strain at a high rate of 0.05 K^{-1} and less than 15% decay of reversibility after isothermal annealing for 2 h.

2.3 Experimental section

2.3.1 Synthesis of octylene-adipate (OA) oligomers

All chemicals were used as purchased from Sigma-Aldrich. In a 100 mL dried two-way round bottom flask that connected to a condenser, 1,8-octane diol (4.0 g, 2.74 mmol) was dissolved in 40 mL anhydrous CH_2Cl_2 under mild heating condition (35 °C). Triethylamine (0.5 g, 5.04 mmol) was added into the mixture. Adipoyl chloride (4.6 g, 2.52 mmol) was injected into the flask using a syringe pump at a rate of 1 mL/h while the mixture was stirring. After injection, the reaction was left for an additional hour. The oligomerization was terminated by filtering the salt triethylamine hydrochloride and then extracting excess of solvent followed by precipitation with methanol in ice bath. Precipitates were filtered and then dissolved in 40 mL dichloromethane and dried by adding anhydrous magnesium sulfate. The product solution was filtered and solvent was removed by rotary evaporator followed by drying under vacuum at room temperature overnight. Based on theory of step growth polymerization, oligomers have the same end-group of the excess monomer. In this study, we used excess amount of diol monomer. The molecular weight of oligomers can be controlled by the ratio of two monomers (1,8-octane diol and adipoyl chloride). Different monomers ratios and the corresponding degree of oligomerization *n* (including theoretical *n* predicted by Carothers equation and experimental *n* measured from 1H-NMR) are summarized in Table 2.1. 1H-NMR (400 MHz, $CDCl_3$): δ (ppm) = 4.07 (t, 4*n* H), 3.66 (t, 4H), 2.34 (t, 4*n* H), [1.68 & 1.63] (broad, -$OCOCH_2$-($C\mathbf{H}_2$)$_2$-), 1.34 (broad,

-$COOCH_2$-($C\mathbf{H}_2$)$_6$-). Degree of oligomerization *n* was calculated as the ratio of area of peaks in δ = 4.07 ppm / δ = 3.66 ppm (Figure 2.1).

Table 2.1 Relationship between monomer ratio and degree of oligomerization.

r [a]	*n*_cal. [b]	Integral (δ = 3.66 ppm) [c]	Integral (δ = 4.07 ppm) [c]	*n*_NMR [d]
0.50	1.8	0.37	1.0	2.7
0.89	8.8	0.15	1.0	6.7
0.91	10.3	0.10	1.0	9.7
0.92	12.3	0.068	1.0	14.7
0.93	14.0	0.066	1.0	15.1
0.95	19.8	0.043	1.0	23.1

[a] Monomer ratio *r* of [adipoyl chloride] to [1,8-octanediol]. $r = \frac{[\text{adipoyl chloride}]}{[1,8-\text{octanediol}]} < 1$. [b] The degree of oligomerization calculated based on Carothers equation. [c] The integrated area of 1H-NMR peaks at δ = 3.66 ppm (-$C\mathbf{H}_2$OH) and δ = 4.07 ppm (-$C\mathbf{H}_2OCOCH_2$-). [d] The degree of oligomerization was calculated as the ratio of integral (δ = 4.07 ppm) / integral (δ = 3.66 ppm).

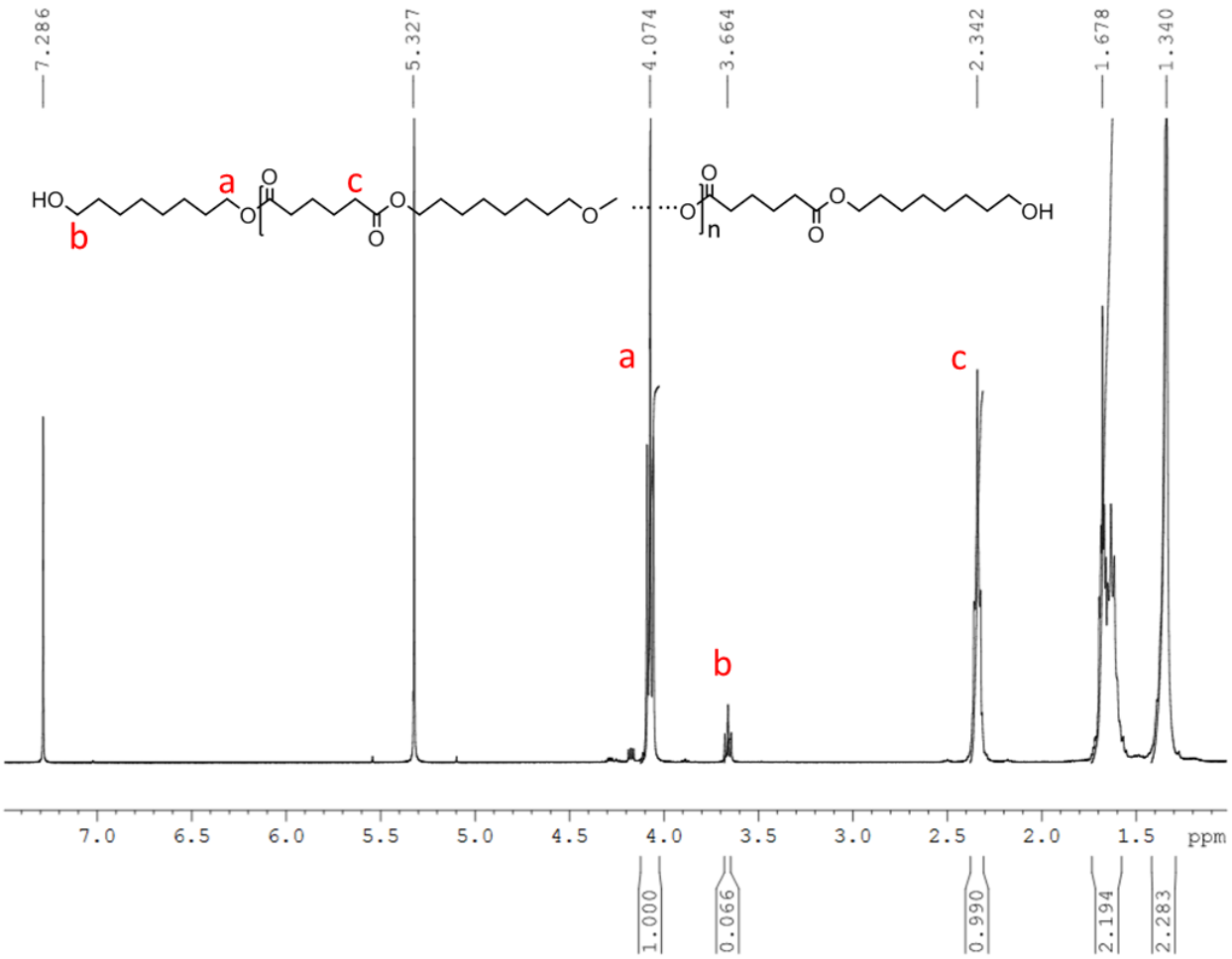

Figure 2.1 1H-NMR (400 MHz, $CDCl_3$) of OA oligomer before end-capping (r = 0.93). δ (ppm) = 4.07 (t, 4n H), 3.66 (t, 4H), 2.34 (t, 4n H), [1.68 & 1.63] (broad), 1.34 (broad). The degree of oligomerization n = integral (δ = 4.07 ppm) / integral (δ = 3.66 ppm) = 1 / 0.066 ≅ 15.1. Peak at δ (ppm) = 5.32 belongs to solvent dichloromethane.

2.3.2 End functionalization of OA oligomers

Mono-end functionalized oligomers were synthesized by the reaction of dissolved OA oligomers (2.0 g, 0.68 mmol) in 20 mL anhydrous CH_2Cl_2 with slowly added 2-isocyanatoethyl methacrylate (0.1 g, 0.68 mmol) in the presence of dibutyltin dilaurate (DBTDL) (0.01 g, 0.016 mmol) as a catalyst in a 100 mL dried round bottom flask. After injection, the reaction was left overnight. The reaction was terminated by extracting excess of solvent and precipitated with

methanol in ice bath. Precipitates were filtered and dried under vacuum at room temperature overnight to extract any remaining solvent. 1H-NMR (400MHz, $CDCl_3$): δ (ppm) = 6.15 (s, 4H), 5.62 (s, 4H), 4.25 (t, 8H), 4.07 (t, 12*n* H), 3.66 (q, 4H), 3.52 (q, 8H), 2.34 (t, 12*n* H), 1.97 (s, 12H), [1.68 &1.63] (broad, -$OCOCH_2$-($C\mathbf{H}_2$)$_2$-), 1.34 (broad, -$COOCH_2$-($C\mathbf{H}_2$)$_6$-). The ratio of mono-end capped chains (dangles) and both-end capped chains has been calculated as the ratio of δ = 3.52 ppm / δ = 3.66 ppm, which is equal to 2/1. Therefore, the mol% of dangles is determined as 67 mol% (Figure 2.2).

To functionalize both end of OA oligomers with methacrylate group, excess amount of 2-isocyanatoethyl methacrylate (0.3 g, 1.7 mmol) was added into OA oligomers (2.0 g, 0.68 mmol) in 20 mL CH_2Cl_2. 1H-NMR (400MHz, $CDCl_3$): δ (ppm) =6.15 (s, 2H), 5.62 (s, 2H), 4.25 (t, 4H), 4.07 (t, 4*n* H), 3.52 (q, 4H), 2.34 (t, 4*n* H), 1.97 (s, 6H), [1.68 & 1.63] (broad, -$OCOCH_2$-($C\mathbf{H}_2$)$_2$-), 1.34 (broad, -$COOCH_2$-($C\mathbf{H}_2$)$_6$-). Disappearance of δ = 3.66 ppm and appearance of capped methacrylate peaks proved full conversion of hydroxyl groups into methacrylate groups at chain ends (Figure 2.3).

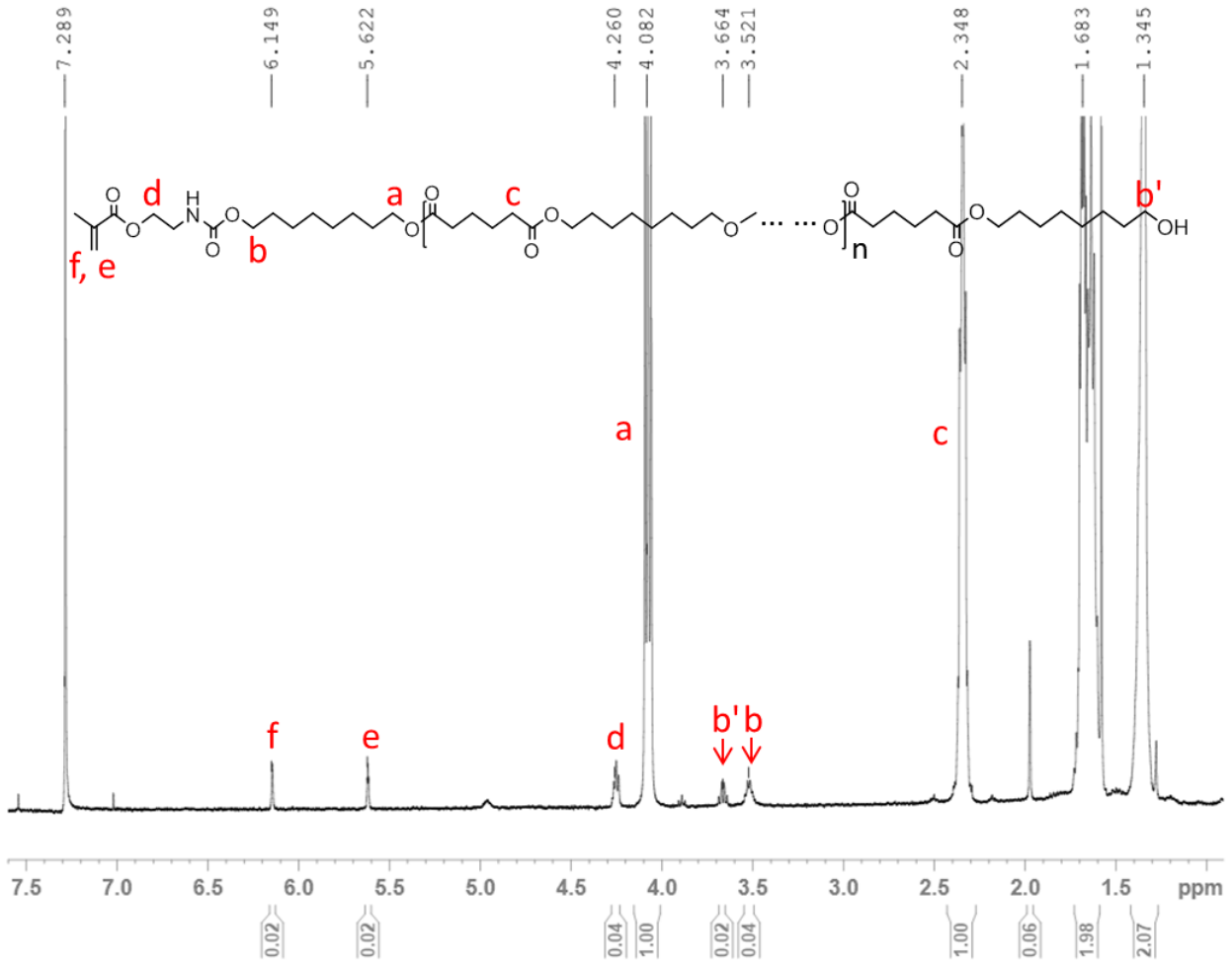

Figure 2.2 1H-NMR (400 MHz, $CDCl_3$) of OA oligomer partially capped by methacrylate group (*n* = 15.1). δ (ppm) = 6.15 (s, 4H), 5.62 (s, 4H), 4.25 (t, 8H), 4.07 (t, 12*n* H), 3.66 (q, 4H), 3.52 (q, 8H), 2.34 (t, 12*n* H), 1.97 (s, 12H), [1.68 & 1.63] (broad), 1.34 (broad). The ratio of dangling chains with free hydroxyl group and both-end capped chains has been calculated as follows:

Assuming x mol of both-end capped chains and y mol of mono-end capped chains,

$$\frac{Free\ hydroxyl\ group}{Reacted\ hydroxyl\ group} = \frac{\text{Integral}\ (\delta\ =\ 3.66\ \text{ppm})}{\text{Integral}\ (\delta\ =\ 3.52\ \text{ppm})} = \frac{1}{2} = \frac{y}{2x+y}$$

$$\text{Therefore}\ y = 2x.$$

So the mol% of dangling chains can be estimated as $\frac{2x}{2x+x} \cong 67\%$.

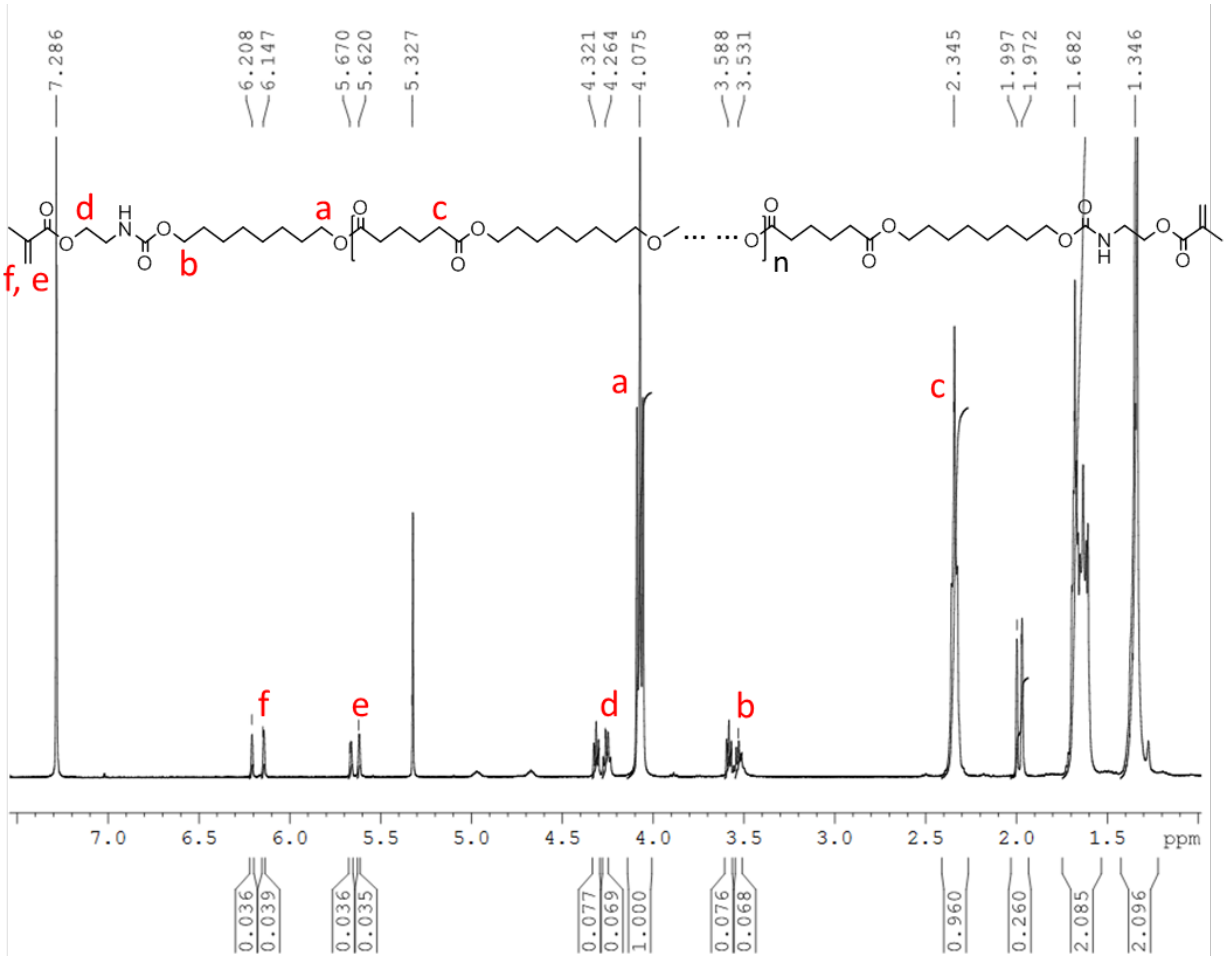

Figure 2.3 1H-NMR (400 MHz, $CDCl_3$) of OA oligomer both-end capped by methacrylate group (*n* = 15.1). δ (ppm) = 6.15 (s, 2H), 5.62 (s, 2H), 4.25 (t, 4H), 4.07 (t, 4*n* H), 3.52 (q, 4H), 2.34 (t, 4*n* H), 1.97 (s, 6H), [1.68 &1.63] (broad), 1.34 (broad). Peaks at δ (ppm) = 6.20, 5.66, 4.31, and 3.58 belong to unreacted excess amount of end-capper 2-isocyanatoethyl methacrylate. Peak at δ (ppm) = 5.32 belongs to solvent dichloromethane.

2.3.3 Networks fabrication by photo-induced free-radical polymerization

A series of poly(octylene adipate) (POA) networks with different crosslink densities was prepared by UV-crosslinking of OA oligomers with different degrees of oligomerization *n*. In a dry vial, bi-functionalized OA oligomers were dissolved in $CHCl_3$ at 50 wt% ratio. 1 wt% of 2, 2-diethoxyacetophenone (DEAP) was added into the mixture and vortex was used to thoroughly

mix all components. The mixture was transferred into a syringe and injected into a PTFE mold covered with a quartz slide on top to prevent solvent evaporation. The filled mold was exposed to UV-365 nm for 5 minutes under nitrogen to form fully cured network. The fabricated network was then taken out and dried in vacuum oven at 80 °C overnight. Due to uncontrolled radical activation, the resulting network has a dense and irregular topology.

In addition, dangling chain ends were introduced into the above network by using mixture of bi-functionalized oligomers and mono-functionalized oligomers. These networks were fabricated in different mole ratios of bi-functionalized oligomers to mono-functionalized oligomers: 100/0 (0% dangles), 60/40 (40% dangles), 33/67 (67% dangles). All molecular parameters of the irregular networks prepared by free-radical polymerization are summarized in Table 2.2.

2.3.4 Networks fabrication by thiol-ene click reaction

Stoichiometric tri-thiol cross-linker, trimethylolpropane tris (3-mercaptopropionate) was mixed with bi-functionalized OA oligomers at different mole ratios of -SH/-methacrylate: 1/1 (100% SH), 0.5/1 (50% SH). UV curing was applied in the same way. Note that reactivity of the click reaction decreases with oligomer size due to viscosity enhancement, which increases the contribution of free-radical polymerization. As will be shown later in Figure 2.4c, for a short oligomer n = 6.7, the crosslink density of 6.7-100% SH sample nearly drops to 1/3 of 6.7-0% SH sample, while the longer oligomer n = 23.1 exhibits a much less decrease in crosslink density due to kinetic domination of the free-radical polymerization. The molecular parameters of the "clicked" networks are summarized in Table 2.2.

The sol-gel fraction of all prepared networks has been measured using Soxhlet extractor in $CHCl_3$ at 65 °C overnight. All samples show gel fraction >95%.

Table 2.2 Molecular structure and physical properties of POA networks.

n [a]	mol% SH [b]	mol% dangle [c]	E [d]	T_m [e]	T_c [e]	ΔH_m [e]	$T_{partial}^{max}$ [f]	ν [g]	λ_{max} [h]	L_{SAXS} [i]	dL_{SAXS} [j]	L_{AFM} [k]	M_0 [l]	M_x [m]
			MPa	°C	°C	J/g	°C	mol/m^3		nm	(FWHM)	nm	kg/mol	kg/mol
2.7	0	0	7.5	27	-2	36	26	842	1.3	13.4	0.027	n/a	1.2	.4
6.7	0	0	5.6	39	13	42	39	630	1.6	14.0	0.024	n/a	2.3	.8
6.7	50	0	4.0	46	24	51	44	450	1.7	16.1	0.023	n/a	2.4	1.6
6.7	100	0	2.7	48	28	50	46	304	1.8	16.4	0.022	n/a	2.5	2.5
9.7	0	0	4.8	47	25	53	45	540	1.7	15.0	0.022	18	3.1	1.0
9.7	50	0	3.6	50	30	54	49	405	2.0	16.5	0.022	n/a	3.2	2.1
9.7	100	0	2.7	56	32	60	50	304	2.5	16.6	0.021	n/a	3.3	3.3
14.7	0	0	4.2	54	30	64	51	472	1.7	15.7	0.024	20	4.4	1.5
14.7	50	0	3.6	55	31	65	53	405	1.7	16.8	0.022	n/a	4.6	3.0
14.7	100	0	2.8	56	34	65	53	315	2.7	17.5	0.021	n/a	4.7	4.7
23.1	0	0	2.3	60	37	73	58	259	1.8	18.5	0.022	22	6.7	2.2
23.1	50	0	2.2	61	41	73	59	248	3.3	18.2	0.021	n/a	6.8	4.6
23.1	100	0	2.0	62	41	75	n/a	225	4.8	18.5	0.021	n/a	7.0	7.0
15.1	0	0	3.8	54	32	64	51	428	1.6	16.1	0.023	n/a	4.6	1.5
15.1	0	40	1.9	59	38	72	52	214	2.5	17.3	0.021	n/a	4.6	2.5
15.1	0	67	0.6	63	43	82	n/a	68	4.0	18.0	0.020	n/a	4.6	4.6

[a] Degree of polymerization of functionalized OA oligomers (Figure 2.4a). [b] Molar fraction of trimethylolpropane tris (3-mercaptopropionate) (Figure 2.4a). [c] Molar fraction of monofunctional OA oligomers (Figure 2.4a). [d] Storage modulus measured by DMA using oscillation mode at 1 Hz, $\varepsilon = 0.001$, T = 80 °C. [e] Melting peak, crystallization peak, and melting enthalpy (integration of melting peak) measured by DSC at 5 K/min. [f] The optimum partial melting temperature at which the maximum reversibility was obtained. Samples 23.1-100% SH and 15.1-67% dangles showed no reversibility. [g] Crosslink density $\nu = G_{80°C}/RT = E_{80°C}/3RT$, $G_{80°C}$ is shear modulus. [h] Extensibility $\lambda_{max} = L_{max}/L_0$. L_{max} is length at break, L_0 is original length. [i] Average long period of lamellae $L_{SAXS} = 2\pi/q_{max}$. q_{max} is peak position of SAXS profile. [j] Distribution of lamellae long period determined by the full width at half maximum of SAXS peak. [k] Average spacing of lamellae on AFM height profile. [l] Molecular weight of functionalized oligomers based on chemical structure. [m] Average molecular weight of network strand depends on the network topology as $M_0/3$ for 0% SH, $2M_0/3$ for 50% SH, M_0 for 100% SH, $(M_0/3)/(1-\text{mol\% dangles})$ for networks with dangled chains. All samples have gel fraction >95%, fixation ratio and recovery ratio >95%.

2.3.5 Differential scanning calorimetry

A heat/cool/heat cycle with a ramp rate of 5 K/min from 0 °C to 80 °C was used for all samples by DSC 220 from Seiko Instruments, Inc. Second heating was used to determine the melting transition, while cooling was used to characterize the crystallization transition. The crystallinity was calculated by the ratio of the integration of heating or cooling transition to the heat of fusion of octylene-adipate polymers, which is close to 150 J/g.[2]

2.3.6 Dynamic mechanical analysis

RSA-G2 dynamic mechanical analyzer from TA Instruments was used for mechanical tests. Storage modulus was measured in oscillation mode at 1 Hz, 0.1% strain. Extensibility was measured at 80 °C with a linear elongation rate of 0.5 mm/s.

In a conventional shape-memory test (the same as in the previous chapter), a targeted programming strain of $\varepsilon_p = 20\%$ is applied to a sample with original shape ε_o at 80 °C (typically, $\varepsilon_o = 0$). Then the sample is cooled (5 K/min) to 0 °C, while maintaining the same programming strain ε_p. After releasing the load and annealing for 1 min at 0 °C, strain relaxes from ε_p to a fixed strain ε_f − programmed shape. Upon heating the sample to 80 °C (5 K/min), the shape recovers strain to ε_r, which is irreversible. To quantify shape fixation and recovery, we use the same parameters defined in Chapter 1:

$$Fixation\ ratio = \frac{\varepsilon_f}{\varepsilon_p} \qquad (1)$$

$$Recovery\ ratio = \frac{\varepsilon_r - \varepsilon_f}{\varepsilon_o - \varepsilon_f} \qquad (2)$$

All samples in this study have fixation ratio and recovery ratio > 95%, therefore we simplify the notations: the fixed shape is the same as programmed shape ($\varepsilon_f = \varepsilon_p$), whereas the

irreversibly recovered shape is the same as original shape ($\varepsilon_r = \varepsilon_o$), which is typically zero ($\varepsilon_o = 0$).

To conduct RSM, a sample of a programmed shape (ε_p), was heated to a partial melting temperature $T_{partial}$, which was close to the melting peak T_m on DSC curves. Upon heating (5 K/min), the programmed shape relaxed to an intermediate state characterized by strain ε_i. After short annealing time Δt at $T_{partial}$ (no less than 100 s to assure uniform temperature distribution), subsequent cooling induced reverse shape transformation towards its programmed shape resulting in a strain increase from ε_i to ε_{rev} − reversed strain. To quantify RSM, we introduce the following parameter:

$$Reversibility = \frac{\varepsilon_{rev} - \varepsilon_i}{\varepsilon_f} \qquad (3)$$

2.3.7 Atomic force microscopy

Oligomers were dissolved in $CHCl_3$ (1 wt%) followed by addition of DEAP (0.01 wt%). The solution was spin-coated onto a mica surface at 1500 rpm for 1 min, then placed on a hot plate (80 °C) to keep oligomers in a melt state. Then the film was cured by UV-365 nm for 5 minutes under nitrogen. AFM images were taken using NanoScope V controller in PeakForce QNM mode (Bruker).

2.3.8 Small angle x-ray scattering.

Measurements were conducted at Brookhaven National Lab, Center for Functional Nanomaterials, using a Bruker Nanostar U instrument equipped with Vantec 2000 area detectors and Copper rotating anode as a source. Scattering patterns from the samples were measured at 0 °C and collection time was set as 30 s for all samples. A polynominal decay function with Savitzky-Golay filter was used for baseline fitting. After baseline subtraction, the peaks were

fitted using Lorentz function to determine the full-width-at-half-maximum (FWHM). All mechanical and morphological characteristics of the POA networks are summarized in Table 2.2.

2.4 Results and discussion

Different formulations of dimethacrylates, monomethacrylates, tri-thiol crosslinkers were utilized to prepare three distinct network topologies (Figure 2.4). In all three synthetic protocols, we varied degree of oligomerization *n* of the oligomers (from 2.7 to 23.1) to cover a wide range of crosslink density (Table 2.2). We did not pursue higher crosslink densities as they imped the crystallization process and disallow shape fixation. We also did not study lower crosslink densities since this would lead to reduction of the restoring force and disable shape memory. Photo-induced free-radical polymerization of bi-functional oligomers (**1**) resulted in an irregular network **I** (Figure 2.4b) and high crosslink density (Figure 2.4c). For example, sample 2.7-0% SH (n = 2.7 of **1** and 0% of **3**) shows the highest crosslink density (842 mol/m^3) and lowest values in T_c (−2 °C) and ΔH_m (36 J/g), which indicates constrained crystallization within a dense network yielding lower crystallinity and smaller crystallites. Additionally (network **II**), we mixed bi- and mono-functional oligomers (**1** + **2**) to introduce dangling chains, which do not support external stress and act as diluents decreasing the crosslinking density. Dangles also enhance crystallization, which is evidenced by rise of T_c from 32 °C to 43 °C and ΔH_m from 64 J/g to 82 J/g with increasing mol% of dangles (Table 2.2). To enable better control of the network topology, we applied thiol-ene click chemistry (**1** + **3**), which allows much faster reaction rate between methacrylate-SH than methacrylate self-polymerization.[3-4] This synthetic approach yields networks **III** with better mesh uniformity, which resulted in lower modulus (Figure 2.4c) and significant enhancement in extensibility (Figure 2.4d).

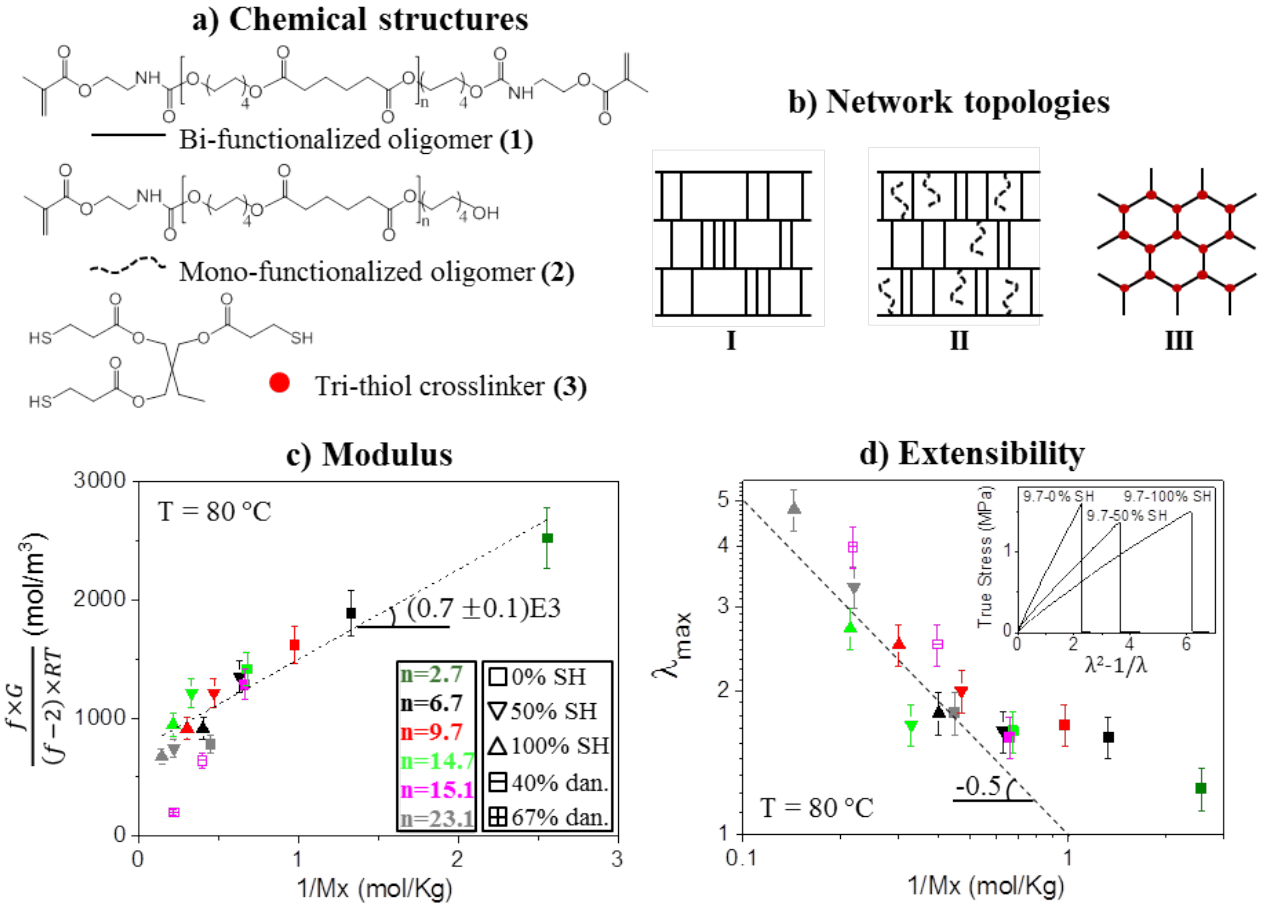

Figure 2.4 Network design and control parameters. a) Bi- (**1**) and mono- (**2**) end-functionalized octylene-adipate (OA) oligomers with an average degree of oligomerization n varied from 2.7 to 23.1 (Table 2.2), and (**3**) tri-thiol cross-linkers. **b)** Irregular topology prepared by free-radical polymerization of **(1)**; dangling chains incorporated by free-radical co-polymerization of **(1)** and **(2)**; uniform topology prepared by click reaction of **(1)** and **(3)**. **c)** The temperature-normalized shear modulus $\frac{f}{f-2}\frac{\mathrm{G}}{\mathrm{RT}}$ increases upon decreasing the average molar mass of network strand M_x. This modulus corresponds to molar crosslink density ν (number of moles of mechanically active network strands per unit volume), where $f = 3$ - branching functionality of network junctions and G - shear modulus measured at T = 80 °C. The dashed line is a linear fit consistent with the classical crossover equation for an entangled polymer network $\nu \cong \nu_e + \frac{\rho}{\mathrm{M}_x}$,[5] excluding samples with dangles that are described by a different model with 'loose-end' correction[6]), where ν_e is the density of chain entanglements. **d)** Extensibility $\lambda_{max} = \mathrm{L}_{max}/\mathrm{L}_0$

measured at T = 80 °C decreases with $1/\mathrm{M}_x$. Samples with **(1+3)** topology follow a linear trend with a slope of -0.5, which is consistent with $\lambda_{max} \sim \sqrt{\mathrm{M}_x}$, theoretically expected for ideal networks. The inset shows true stress-true strain curve until break.

Shear modulus G of polymer networks was measure in a melt state at T = 80 °C. Figure 2.4c depicts the average molar crosslinking density $\nu \cong \frac{f}{f-2}\frac{\mathrm{G}}{\mathrm{RT}}$ versus the number-average molar mass of the strands M_x for different network topologies with $f = 3$ (functionality of the crosslink junctions). The slope $0.7 \cdot 10^3$ kg/m^3 of the linear fit (dashed line) is in good agreement with the polymer mass density $\rho \cong 10^3$ kg/m^3, whereas the intercept $\nu_e = 200$ mol/m^3 and the corresponding shear modulus of $\mathrm{G}_e \cong \frac{f-2}{f}\nu_e \mathrm{RT} \cong 1.7 \cdot 10^5$ Pa are consistent with the respective characteristics of a typical entangled network ($\nu_e \sim 100$ mol/m^3 and $\mathrm{G}_e \sim 10^5$ Pa).[7] These agreements, along with the characteristic slope in Figure 2.4d, indicate good synthetic control of the network topology and the crosslink density.

Network topology exhibits significant effect on samples' extensibility (λ_{max}), which was measured in a melt state at T = 80 °C. As seen in Figure 2.4d, the irregular dense networks (**I**) demonstrate poor extensibility ($\lambda_{max} < 2$) due to highly non-uniform stress distribution over the network strands. In contrast, the more uniform networks (**III**) and the network with dangling chains (**II**) allow extensions up to 5-times. Three samples with the same $n = 9.7$ exhibit almost the same stress-at-break (~ 1.5 MPa), while the strain-at-break increases up to three times as SH% increases. These loose networks show excellent shape memory behavior (~ 100% shape fixity and recovery) at high programming strains exceeding 100%. However, as discussed below, the shape reversibility decreases upon lowering crosslink density. In fact, one of the most irregular

and dense networks studied in this paper (2.7-0% SH) exhibits the best reversibility (ca. 80% of the programmed strain), while possessing the highest modulus and worst extensibility.

Network topology and crosslink density greatly affect organization of the crystalline scaffold in semi-crystalline polymer networks. To study these effects, we used a combination of techniques including Atomic Force Microscopy (AFM), Small and Wide Angle X-ray Scattering (SAXS and WAXS), and Differential Scanning Calorimetry (DSC). AFM height micrographs in Figure 2.5a show morphology of three samples with different crosslink densities, where we see a characteristic organization of spherulite branches, composed of lamellae stacks (insets). With decreasing crosslink density, both size of the bundles and spacing between the stacked lamellae inside a bundle increase. This observation is attributed to the effect of crosslinking, which exerts both topological and dynamic constraints on network strands hindering the crystal growth.

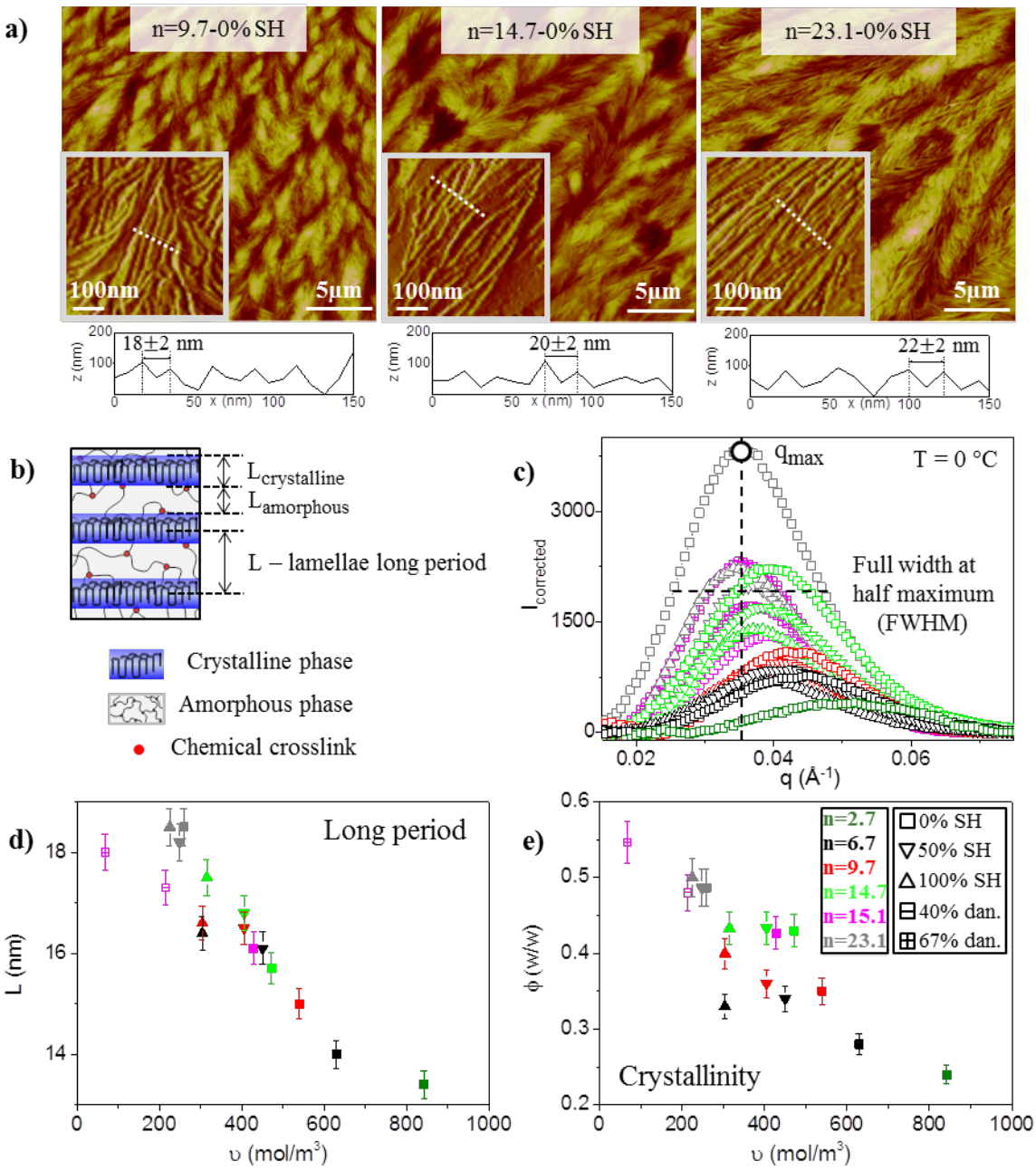

Figure 2.5 Constrained crystallization: long period and crystallinity. a) AFM height micrographs of spin-coated films of POA networks with three different crosslink densities, determined by degree of oligomerization *n* as indicated. The micrographs show spherulite branches composed of lamellae stacks (insets). Cross-sectional profiles (along dashed lines in the insets) display an increase of spacing between lamellae with *n*. The spacing was averaged over 100 lines in a chosen area. **b)** Molecular interpretation of stacks of folded-chain lamellae separated by an amorphous phase composed of chain folds, crosslink junctions, uncrystallized

strand sections. **c)** SAXS spectra after subtracting the polynominal decay function-fitted baseline were measured at 0 °C. Peaks were fitted using Lorentz function. Position q_{max} and peak full-width-at-half-maximum (FWHM) were determined. **d)** Lamellae long period $L = 2\pi/q_{max}$ and **e)** crystallinity $\phi = \Delta H/\Delta H_m^0$ decrease with crosslink density. The crystallinity numbers were obtained by DSC ($\Delta H_m^0 = 150$ J/g) and calibrated with WAXS as described elsewhere.[8]

More quantitative information about the crystalline structure was provided by X-ray scattering and DSC. From SAXS intensity profile in Figure 2.5c, we determined the long period as $L = 2\pi/q_{max}$, which includes both crystalline and amorphous fractions (Figure 2.5b). We have also calculated the full-width-at-half-maximum (FWHM) as a rough indication of the crystalline structure's dispersity, assuming negligible contribution of crystallite size to peak broadening.[9-10] As shown in Figure 2.5d, the long period decreases almost linearly with crosslink density, resulting in nearly 6 nm reduction in *L* between the highest and lowest crosslink density samples. This is consistent with the corresponding decrease of the melting temperature (Table 2.2) as predicted by the Gibbs-Thomson equation, assuming that the long period is proportional to crystal size. Figure 2.5e shows that the increase of the crosslink density also results in a significant decrease of crystallinity, which was measured by DSC and then calibrated by WAXS [8] as shown in Figure 2.6. As an example, sample 2.7-0% SH with the highest crosslink density shows the smallest crystal size (L), lowest melting temperature (T_m), and least amount of crystallinity (ΔH_m). Besides crosslink density, the effect of network topology (controlled by SH%) is also significant. As shown in Figure 2.7, the dispersity of crystal size reduces with increasing SH%. This is ascribed to a less constrained crystallization of more uniform networks exert.

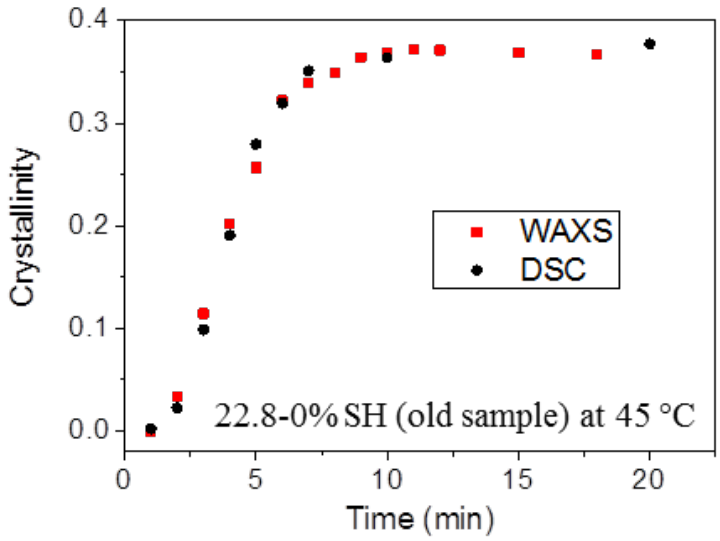

Figure 2.6 Crystallinity measurements using DSC and WAXS. Using Differential Scanning Calorimetry (DSC), we calculated the integral of melting peak (enthalpy ΔH) and crystallinity was calculated as $\phi = \Delta H/\Delta H_m^0$, $\Delta H_m^0 = 150\ J/g$. WAXS was used to calibrate the crystallinity measured by DSC. By taking the ratio of integral of crystalline peak and amorphous background on a WAXS curve (data shown previously in reference[8]), we can calculate the crystallinity based on WAXS profile. The two techniques have shown >98% agreements with each other. In this study, all crystallinities are calculated using DSC.

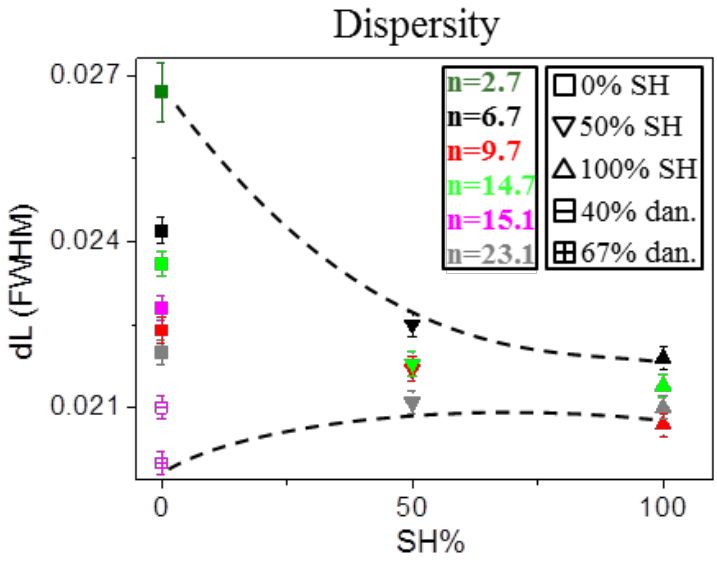

Figure 2.7 Dispersity of crystal size. SAXS profile was measured at 0 °C and subtracted by the polynominal decay function with Savitzky-Golay filter fitted baseline. Then peaks were fitted using Lorentz function. Peak's full-width-at-half-maximum (FWHM) were measured and decreased with SH%, indicating a narrower distribution of crystal size of a uniform mesh network.

All structural data are summarized in Table 2.2, which demonstrates consistent variations of the molecular and morphological characteristics. This provides a good foundation for quantitative studies of correlations between network architecture, crystalline morphology, and reversible shape memory (RSM). Some discrepancy in the long period (L) values determined by AFM and SAXS is ascribed to the surface effect on the crystallization process and 2D AFM-imaging of a 3D structure. Although the AFM study is less accurate than SAXS with respect to measurements of crystalline dimensions, it provides visual verification of the lamellae morphology.

Figure 2.8a depicts basic steps of reversible shape memory: fixation and recovery. The original (equilibrium) shape is controlled by entropic elasticity of a percolated polymer network secured by chemical crosslinks. To balance the network elasticity and fix a desired strain, a crystalline scaffold is introduced upon cooling (programming step). This scaffold may be viewed as a physical network, which also percolates through the entire sample with a mesh size larger than that of the chemical network. The percolation is essential as it enables fixation of the programmed shape. The left panel of the plot in Figure 2.8a demonstrates that less than 5% crystallinity is required for nearly 100% shape fixation. This observation is consistent with other shape persistent objects and organisms such as jelly fish supported by ca. 2 wt% of an organic scaffold.[11] Subsequent crystallization generates an additional substantial fraction of the crystalline phase of ca. 30 wt%. Although these extra crystals are not required for shape fixation,

they greatly contribute to the sample rigidity as the Young's modulus increases from the MPa to GPa range during crystallization (Figure 2.9). On heating (right panel of the plot in Figure 2.8a), the scaffold melts resulting in shape recovery. The shape alteration suggests that the scaffold percolation is interrupted, which presumably yields percolated clusters. The existence of such clusters was indirectly confirmed by measurements and modeling of shear modulus ($G \sim \phi^3$) of a semi-crystalline polymer network as a function of crystallinity (ϕ) during melting.[1] On complete melting, the original shape is recovered and stays irreversible upon cooling. All samples in this study have high fixation ratio and recovery ratio ranging within 95-99%, which suggests an effective balance between elasticity of the chemical network and rigidity of the crystalline scaffold.

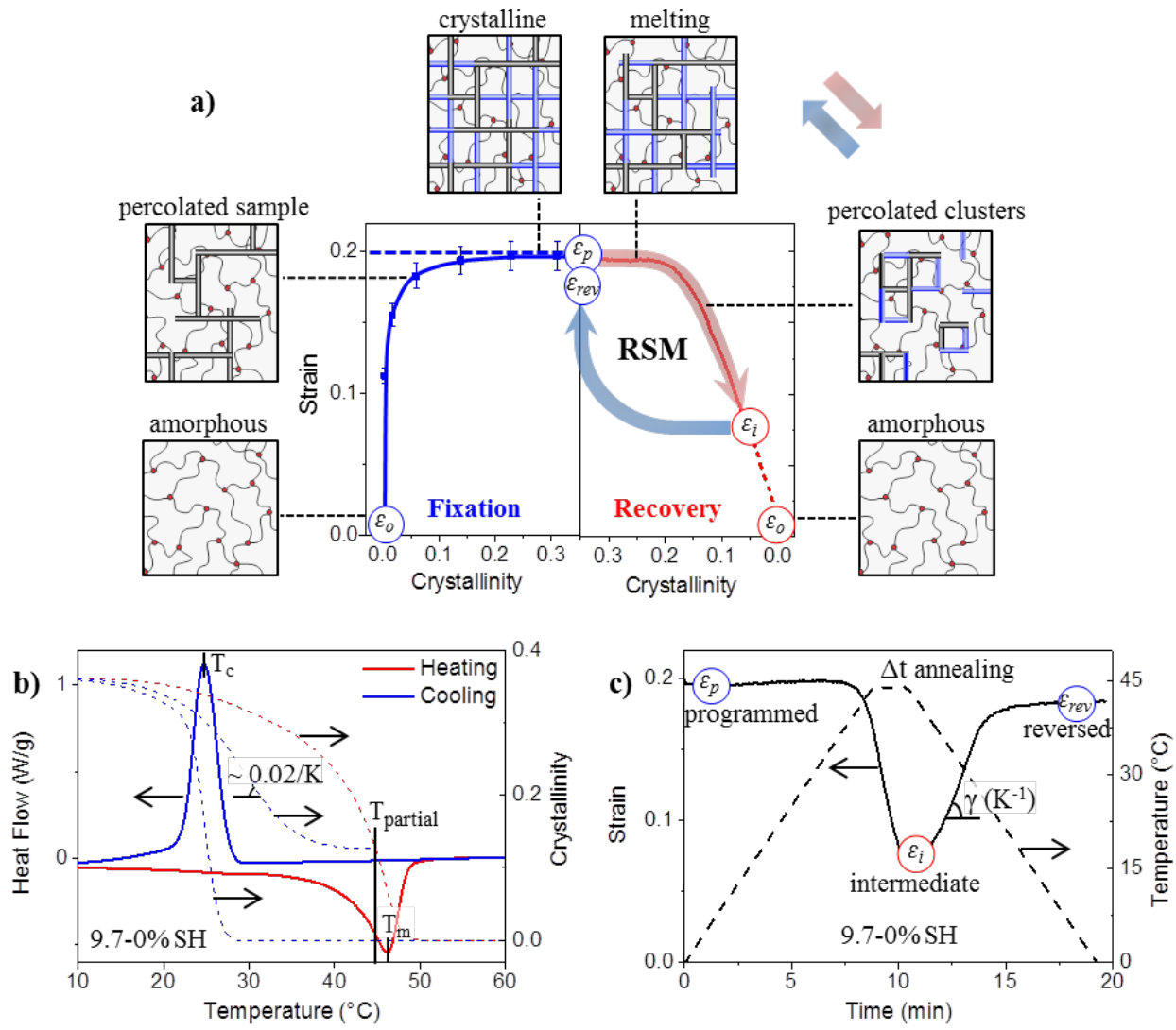

Figure 2.8 Concept and protocol of reversible shape memory (RSM). a) Shape programming, fixation, and recovery. A programing strain of ε_p = 20% (dashed blue line) is applied to sample 9.7-0% SH at 80 °C and then fixed by quenching to 0 °C. Each data point in the fixation panel corresponds to a strain fixed by quenching at a given stage of the crystallization process. A percolated crystalline scaffold is developed. Crystals in black color indicate early stage (critical) in fixation, blue color indicate the rest 'redundant' crystals in fixation. At final stage of fixation, sample is fixed to the programmed strain ε_p. Upon melting, the crystalline scaffold is melted into percolated clusters. At any stage of the melting process, heating can be switched to cooling and reverse the shape transformation from ε_i to ε_r. **b)** A DSC curve of sample 9.7-0% SH showing melting T_p and crystallization transition T_c, using 5 K/min heating/cooling ramp rate. Partial

melting temperature $T_{partial}$ is chosen near T_m. The integration of melting and crystallization peak (enthalpy) divided by the heat of fusion (~ 150 J/g) is calculated as crystallinity, shown in dashed lines. The crystallization rate after cooling from $T_{partial}$ is about 2% crystallinity per K (Figure 2.13). **c)** The strain reversibility is studied as a function of $T_{partial}$ and annealing time Δt at $T_{partial}$. After programming, a sample with programmed strain ε_p is heated to $T_{partial}$ ($T_{partial}^{max}$ = 45 °C). Upon cooling, strain returns to ε_{rev}. The rate of strain recovery γ (K^{-1}) is measured as the linear slope multiplying the ramp rate 5 K/min.

To achieve reversible shape shifting, a programmed sample (ε_p), is heated to a partial melt state causing partial shape recovery to an intermediate strain (ε_i). When cooled back, the sample undergoes recrystallization resulting in reverse strain variation towards the programmed shape (ε_{rev}). As discussed previously,[1] the reversed shape transformation upon cooling is caused by self-seeding recrystallization of molten chains in the presence of the remaining crystalline scaffold. The extent of reversibility (eq. 3) is controlled by the interplay of two networks: (i) the chemical network, which is partially relaxed at $T = T_{partial}$ and (ii) the crystalline scaffold, which is partially degraded at $T = T_{partial}$. While counteracting, both networks provide topological constraints for the molten strands and direct the recrystallization process. If $T_{partial}$ is too low ($T_{partial} < T_m$) and the crystalline fraction is still high, sample is prone to stay at its programmed state without any, or just marginal shape change. If $T_{partial}$ is too high ($T_{partial} > T_m$), the crystalline scaffold is largely destroyed allowing for random pathways for polymer crystallization. By measuring reversibility (eq. 3) as a function of $T_{partial}$ (Figure 2.10), we determined an optimum temperature $T_{partial}^{max}$, which allowed for the greatest reversibility. Table 1 summarizes $T_{partial}^{max}$ values determined for each sample and shows that this temperature is near T_m ($T_{partial}^{max} \approx T_m$). The counteraction of the chemical and physical networks depends on the

crosslink density, which determines both restoring force of the chemical network and recrystallization of the crystalline scaffold. As shown in Figure 2.11a, reversibility initially increases with crosslink density (ν) and then levels off at ca. 80% as it reaches $\nu > 600\ \mathrm{mol/m^3}$. This range of crosslink density corresponds to the irregular networks of Type **I** (Figure 2.4b) with shortest strands.

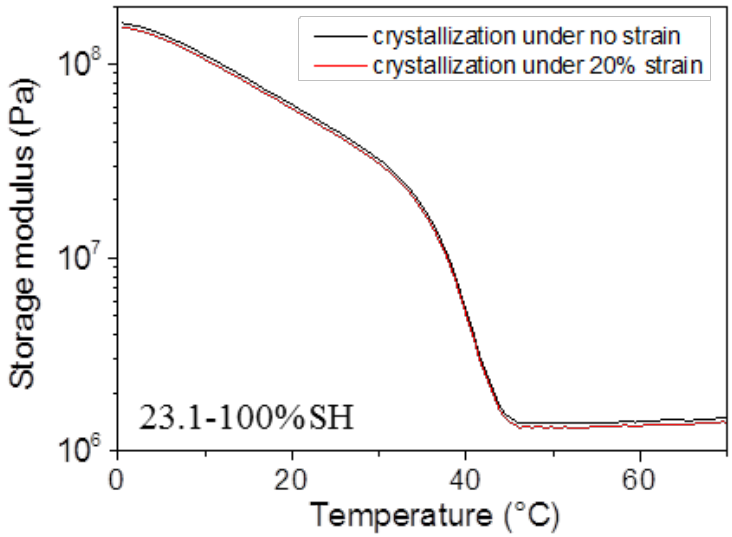

Figure 2.9 Strain effect on storage modulus. DMA measured storage modulus upon cooling at 5 K/min using oscillation mode at 1 Hz but different strains. By applying different strains (0% and 20%), the modulus varies slightly, indicating small difference in crystallinity. In this study, the programming strain was kept as 20%, therefore the strain effect can be neglected. The sample shown is 23.1-100% SH.

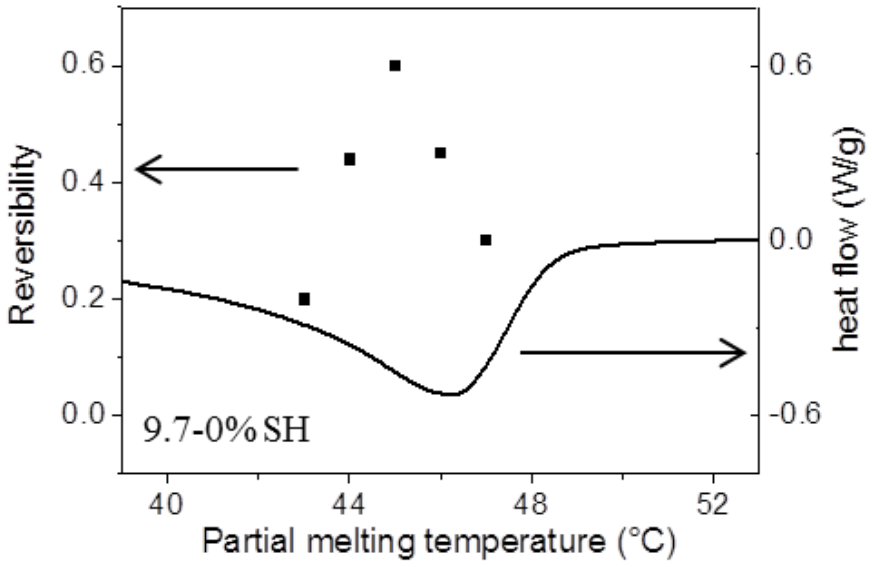

Figure 2.10 Reversibility dependence on the partial melting temperature. After shape programming with ~ 20% strain, the sample was heated to various partial melting temperatures at a heating rate of 5 K/min. The strain was partially recovered to ε_i. Then apply cooling at 5 K/min, the strain recovered to ε_{rev}. By calculating reversibility at different $T_{partial}$ using equation (3), an optimum $T_{partial}^{max}$ with the maximum reversibility can be determined. This optimum $T_{partial}^{max}$ locates near the melting peak on a DSC curve. Sample shown here is 9.7-0% SH.

A similar effect was observed for the recovery rate $\gamma = d\varepsilon/dT$, which is defined in Figure 2.10c as strain recovered on 1 K cooling from the partial melt state. As shown in Figure 2.11b, sample 2.7-0% SH with the highest crosslink density (ν = 842 mol/m^3) recovers 5% of its programmed strain per 1 K of temperature decrease, while the looser networks demonstrate progressively slower recovery. In this study, we have applied 5 K/min cooling rate. For faster cooling, the recovery process takes only a few seconds, which has been useful the design of a robotic gripper.[1] It is also instructive to examine correlation between the recovery rate and crystal size. Using the L vs. ν plot in Figure 2.5d, we can plot the recovery rate (γ) in Figure 2.12b as a function of the lamellae long period (L) (see inset of Figure 2.12a). The log-log plot

shows strong decay of the recovery rate as $\gamma \sim \mathrm{L}^{-4}$. A physical interpretation of this scaling relation can be developed by expressing the recovery rate as function of crystallinity $\phi \cong n\mathrm{L}^3$ as $\gamma = \frac{d\varepsilon}{dT} = \frac{d\varepsilon}{d\phi}\frac{d\phi}{dT} \cong \frac{d\varepsilon}{dn}\frac{\dot{\phi}}{L^3}$, where n – number of crystallites per unit volume, $\dot{\phi} = d\phi/dT$ – crystallization rate, and L is proportional to the average crystal size. Experimentally, we have measured and shown that the crystallization rate weakly depends on the crosslink density and equal $\dot{\phi} = 2 \pm 0.1$ wt%/K (Figure 2.11). By equating the experimentally measured $\gamma \sim \mathrm{L}^{-4}$ and the above scaling relation $\gamma \sim \frac{d\varepsilon}{dn}\mathrm{L}^{-3}$, we obtain that the amount of strain secured by one crystal increase with decreasing the crystal size as $\frac{d\varepsilon}{dn} \sim \mathrm{L}^{-1}$. In other words, materials with smaller crystals allow for higher efficiency of shape fixation.

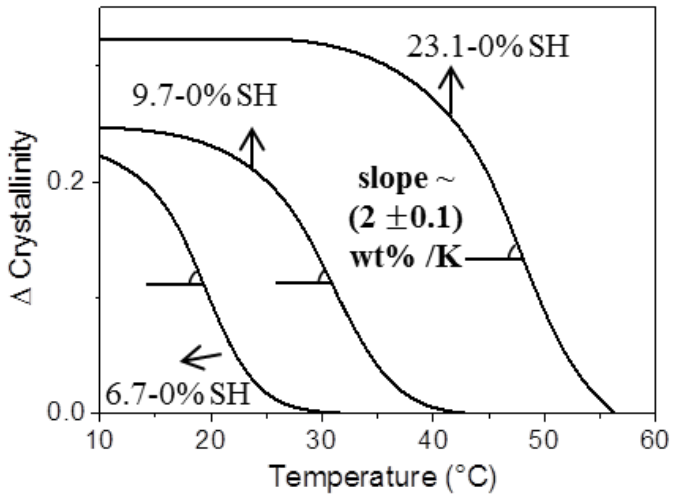

Figure 2.11 Crystallization rate. Upon cooling from a partial melting temperature at 5 K/min, we calculated crystallinity change with temperature. Crystallization rate was then determined as the linear slope on the crystallinity-temperature curve. The rate was similar for different degrees of oligomerization *n*, therefore it can be treated as a constant (2 wt% crystal /K) for all samples for approximate calculations.

The slower shape response of the loose networks is ascribed to faster stress relaxation in the network strands upon melting. To verify this conclusion, we have studied the decay of reversibility during annealing in the partial melt state, when chain relaxation and recrystallization occur simultaneously. While relaxation of molten chains reduces their correlation with the programmed shape leading in a decrease of ε_{rev}, isothermal recrystallization causes spontaneous increase in the intermediate strain ε_i towards the programmed shape ε_p. As such, the reversible strain fraction $\Delta\varepsilon = \varepsilon_{rev} - \varepsilon_i$ decrease from both sides, i.e. due to decreases of ε_{rev} and increase of ε_i, resulting in the decay of reversibility (eq. 3). However, the decay of reversibility is much lower in the samples with higher crosslink density. For example, 9.7-0% SH can maintain more than 85% of its initial reversibility after relaxing for Δt = 2 h at $T = T_{partial}^{max}$. For short time variations (minutes), no measurable decay of reversibility was observed (Figure 2.13).

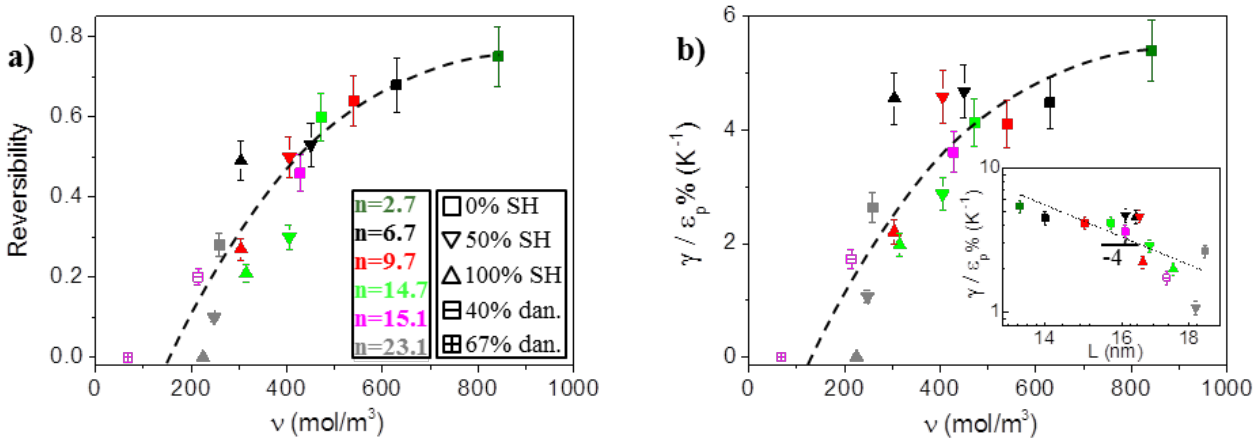

Figure 2.12 Reversibility and recovery rate: the effect of crosslink density and crystal size. **a)** Reversibility (eq 3) increases with crosslink density within a range of ca. 50-1000 mol/m^3. Reversibility varies from 0% to nearly 80%. **b)** The strain recovery rate γ normalized by ε_p, increases with crosslink density and decreases with lamellae period L ~ crystal size. A characteristic slope of −4 in the inset has shown great efficiency of smaller crystals.

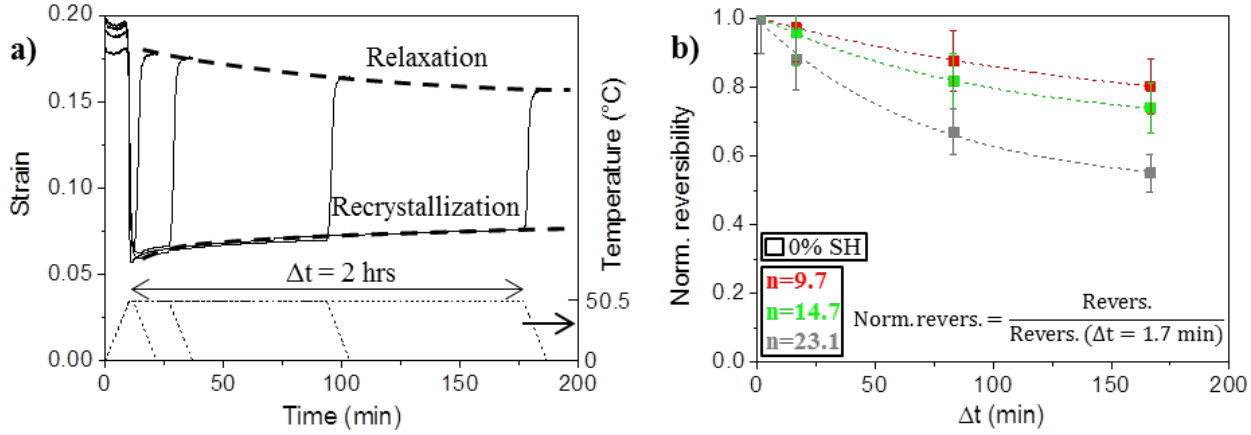

Figure 2.13 Relaxation and recrystallization. a) Sample 14.7-0% SH was used to show the effect of annealing time Δt at a partial melt state. A series of temperature ramps (5 K/min) was applied including heating to $T_{partial}^{max} = 50.5\,℃$, followed by isothermal annealing at $T = 50.5\,℃$ for a controlled duration of Δt and cooling to 0 °C. As Δt increases, from 1.7 min to 120 min, the lower dashed line (the strain of partial melt state ε_i) goes up because of the strain increased by isothermal recrystallization; the upper line (the strain of reversed state ε_{rev}) goes down because of the relaxation of molten chains. Overall, the recoverable portion ($\varepsilon_{rev} - \varepsilon_i$) decreases with the annealing time Δt. **b)** Fraction of reversible strain (eq 3) decreases with upon relaxation during Δt and higher crosslink-density samples show slower decay of reversibility. The Y-axis corresponds to normalized reversibility, i.e. fraction of reversible strain (eq 3) at different relaxation times Δt is divided by the corresponding fraction at Δt = 1.7 min.

2.5 Conclusion and outlook

Our understanding of reversible shape memory (RSM) has been advanced through accurate tuning of the architecture of semi-crystalline poly(octylene adipate) networks. Systematic variation of the network-strand length along with molar fractions of dangling chains and tri-thiol cross-linkers provided valuable correlations between the network topology, crosslink density, and mechanical properties (extensibility, modulus) of polymer network in a melt state. These variations of the network architecture directly affect the crystalline scaffold properties

(crystallinity and crystal size), as chemical crosslinks exert significant constraints on the crystallization process. Even though, the irregular and dense polymer networks generate smaller crystals with broader size distribution, they are more effective for shape control. The RSM properties (degree of reversibility and shape recovery rate) are shown to be mainly controlled by crosslink density, whereas the network topology plays a minor role for RSM. The developed structure-property correlations provide guidelines for network design targeting different RSM applications. For example, dense irregular network are suitable for fabrication of actuators that require small strain and fast cyclic motion, whereas loose networks allow for large-strain, yet, one-time actuation (Figure 2.14).

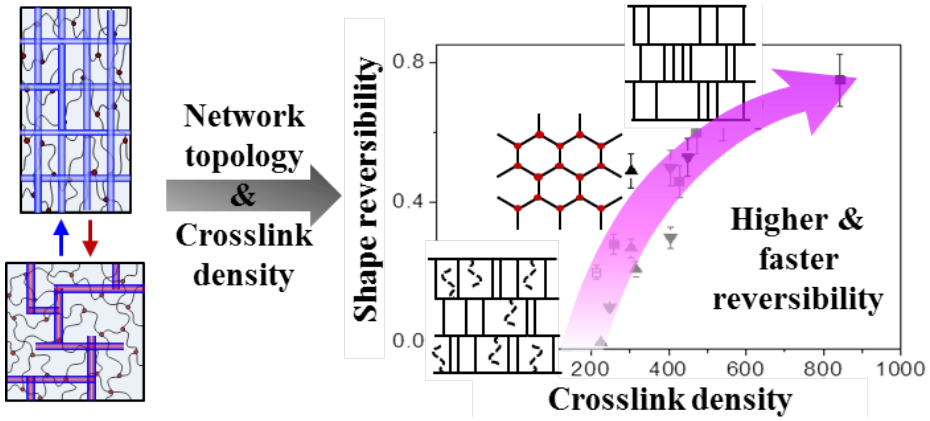

Figure 2.14 Network topology and crosslinking density effect on reversibility. Irregular network with highest crosslinking density shows the best reversibility. Reversibility is mainly controlled by network crosslinking density, whereas network topology plays a minor role.

2.6 REFERENCES

1. Zhou, J.; Turner, S. A.; Brosnan, S. M.; Li, Q.; Carrillo, J.-M. Y.; Nykypanchuk, D.; Gang, O.; Ashby, V. S.; Dobrynin, A. V.; Sheiko, S. S., Shapeshifting: reversible shape memory in semicrystalline elastomers. *Macromolecules* **2014,** *47* (5), 1768-1776.

2. Flory, P.; Garrett, R.; Newman, S.; Mandelkern, L., Thermodynamics of crystallization in high polymers. Cellulose trinitrate. *Journal of Polymer Science* **1954,** *12* (1), 97-107.

3. Hoyle, C. E.; Bowman, C. N., Thiol–ene click chemistry. *Angewandte Chemie International Edition* **2010,** *49* (9), 1540-1573.

4. Lewis, C. L.; Meng, Y.; Anthamatten, M., Well-Defined Shape-Memory Networks with High Elastic Energy Capacity. *Macromolecules* **2015,** *48* (14), 4918-4926.

5. Colby, R.; Rubinstein, M., Polymer physics. *New-York: Oxford University* **2003**, 274-281.

6. Treloar, L. R. G., *The physics of rubber elasticity*. Oxford University Press, USA: 1975.

7. Patel, S. K.; Malone, S.; Cohen, C.; Gillmor, J. R.; Colby, R. H., Elastic modulus and equilibrium swelling of poly (dimethylsiloxane) networks. *Macromolecules* **1992,** *25* (20), 5241-5251.

8. Zhou, J.; Li, Q.; Turner, S. A.; Ashby, V. S.; Sheiko, S. S., Isothermal programming of triple shape memory. *Polymer* **2015,** *72*, 464-470.

9. Tsao, C.-S.; Chen, H.-L., Concurrent transformation of copolymer domain morphology induced by the order-disorder transition of comb block in supramolecular comb-coil block copolymer. *Macromolecules* **2004,** *37* (24), 8984-8991.

10. Loo, J.; Ooi, C. P.; Boey, F., Degradation of poly (lactide-co-glycolide)(PLGA) and poly (L-lactide)(PLLA) by electron beam radiation. *Biomaterials* **2005,** *26* (12), 1359-1367.

11. Lowndes, A., Percentage of water in jelly-fish. *Nature* **1942,** *150*, 234-235.

CHAPTER 3: DYNAMIC OPTICAL GRATINGS ACCESSED BY REVERSIBLE SHAPE MEMORY[3]

3.1 Introduction and objective

Technological advances increasingly require optical components to be adaptable and multifunctional. Standard photonic components are typically crafted from rigid materials, with photonic structures often fabricated using ruling processes and copied with other rigid materials.[1] This rigidity allows photonic components to have only a single designed function, while in some cases switchable micro-optics components are desirable. Advances in soft lithography have allowed for the production of adaptable optical elements that use polydimethylsiloxane (PDMS) elastomers to mold photonic shapes.[2-5] These photonic replicas can be stretched or compressed to induce a tunable optical response, and thus have shown a promising ability for use in optical setups, but the need for constant loads to be applied limits the application of these devices.

Shape memory polymers (SMPs) are polymer networks capable of switching from one programmed shape to another. Two programming steps are necessary to prepare a semi-crystalline elastomer for shape memory actuation. First, a primary shape is obtained via physical or chemical crosslinking.[6] The secondary shape is then programmed by heating the crosslinked sample above its melting temperature (T_m), applying a force, and cooling below the T_m with the force still in place. When the force is removed, the secondary shape is maintained until a suitable

[3]This chapter previously appeared as an article in *ACS Appl. Mater. Interfaces*. The original citation is as follows: - Q. Li,[#] C. Tippets,[#] Y. L. Fu, E. Donev, J. Zhou, S. A. Turner, A-M. Jackson, V. S. Ashby, S. S. Sheiko and R. Lopez, Dynamic Optical Gratings Accessed by Reversible Shape Memory. *ACS Appl. Mater. Interfaces*, **2015**, 7 (26), 14288-14293.

external stimulus of heat, sound, light, or electricity is applied.[7-10] However, without external forces or designed structural constrains, most shape memory processes are irreversible.[11-13] Recent studies have shown that it is possible to reversibly "shape-shift" between two programmable shapes without applying external forces or reprogramming in a process called reversible shape memory (RSM). This approach offers a new route to hands-free multi-functionality,[14-16] and is a consequence of the interplay of the crystalline scaffold and chemical crosslinks, which are each capable of encoding a distinct shape. Partial melting of the crystalline scaffold leaves behind a latent crystalline template, and the programmed shape is recovered upon cooling by self-seeded crystallization along kinetically preferred pathways to replicate the scaffold. The reversibility is controlled by tuning the chemical crosslinking density as well as the partial melting temperature. At a macroscopic scale, the maximum reversibility of tensile strain has been reported as 75% for poly(octylene adipate) elastomers.[16]

Compared to rigid optical components, SMP optics can be tunable with no external force needed to maintain a secondary shape. At smaller scales, SMPs have been explored for their ability to memorize micrometer and sub-μm features as well.[17-19] For example, Xu et al. crafted deformable micro-optic surface structures from SMPs for use as dynamic optical components.[19] However, the advantages of SMP micro optics are often hampered by the irreversibility of most shape memory processes. Previous studies have demonstrated microstructured surfaces can be modulated via RSM to change surface effects including adhesion and wetting.[18]

Here we report on the utilization of RSM at a sub-μm scale to create a reversibly tunable optical element. The ridge-type grating was chosen as a simple proof-of-principle model due to the straightforward relationship between ridge height and diffraction intensity. Understanding the reversible behavior of this photonic structure can then be extended to other grating geometries,

e.g. tooth-shaped, sawtooth shaped and triangle shaped.[20-22] We have programmed a sub-μm ratio optical grating that exhibits reversible magnitude changes of its diffraction intensity (up to about 36% modulation) when subjected to alternating changes in temperature. We have verified that this result is attributable to reversible modulation in the grating's ridge height and that it is repeatable over multiple cycles. Through melting all crystalline regions within the sample, the grating structure can be erased, recovering the primary flat surface, which can then be reprogrammed to a new shape.

3.2 Experimental section

3.2.1 Material fabrication

For this experiment we sought to fabricate the reversible optical element in a representative semi-crystalline polymer poly(octylene adipate) (POA) as reported previously.[16] The chemical structure of end-functionalized POA is shown in Figure 2.4a. In order to utilize the best RSM behavior of POA, we synthesized POA with a number average degree of polymerization (DP) of $n = 13$ ($M_n = 3500\ \mathrm{g/mol}$), which is known to exhibit significant shape reversibility.[16] In the previous work, we used the condensation polymerization between adipic acid and octylene diol to produce POA,[16] while in the present paper we have improved this synthesis by adipoyl chloride reacting with octylene diol. The new route faster reaction and more accurate control of molecular weight distribution. This resulted in a higher T_m 58 °C compared to previous synthesis which has T_m around 50 °C. Under the experimental ramping condition, a strain reversibility of 41% was observed when the shape-memory polymer was subjected to 15% uniaxial strain deformation (Figure 3.1). Figure 3.2b displays a two-step thermosetting procedure which has been used to make an optical grating with reversible control over grating height. First, POA was mixed with 10 wt% $CHCl_3$ and 1 wt% 2,2-

diethoxyacetophenone (DEAP). The mixture was then injected into a Teflon mold, covered with a glass slide and crosslinked with 365 nm UV light for 5 minutes. This produced a RSM substrate with an optically flat surface as the primary shape. The substrate was then annealed free-standing at 70 °C overnight to extract the remaining solvent and thermal history. Next, the substrate was heated to 70 °C and the optically flat surface was pressed against a perfluoropolyether (PFPE) grating (pitch 750 nm, ridge height 250 nm, ridge width 250 nm) followed by quenching in an ice bath. On separation of the substrate and the PFPE mold, the surface was in its secondary grating shape, which accurately replicated the PFPE grating.

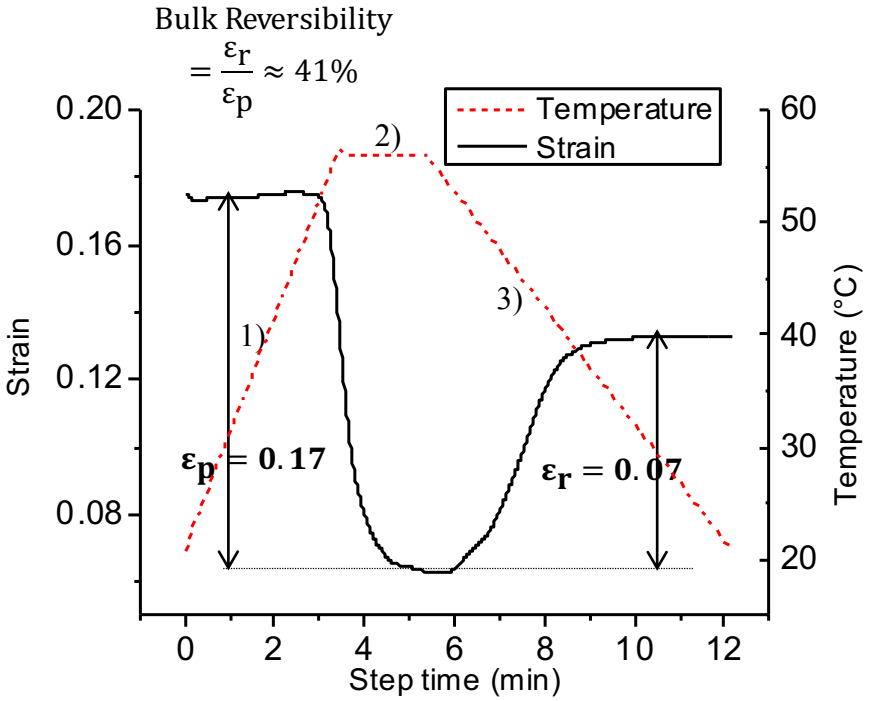

Figure 3.1 Bulk reversibility. A dogbone bulk sample's maximum reversibility was characterized by DMA tensile test as 41%, where ε_p was defined as programmed strain and ε_r as recovered strain. Partial melting temperature T_p was near T_m = 56 °C. The temperature ramp has similar rate as the optical experimental set up: 1) Heat from 20 °C to 56 °C (10 °C/min); 2) Wait 2 min at 56 °C; 3) Cool from 54 °C to 20 °C (5 °C/min).

3.2.2 Optical measurements

Experimental measurements of the grating diffraction intensity were taken under illumination using a light from a 633 nm He-Ne laser, which was incident at a 5° angle with respect to the sample normal, the experimental set up is shown in Figure 3.3. The 750 nm grating pitch was chosen, such that only the M = +1 diffraction order will be measured, with sufficient angular space between the specular reflection (M = 0). Planar diffused Silicon photodiodes (United Detector Technology) with a spectral sensitivity from 400-1100 nm and a responsivity of ~0.4 A/W at 633 nm were used to monitor the intensity of the 1st order diffraction mode and the intensity of the incident beam in order to correct for power fluctuations, and the temperature of the sample was controlled using a thermoelectric stage. Incident beam intensity was monitored by splitting the initial beam with a 50/50 beam splitter and measured with a diffused planar silicon detector. Simultaneously the 1st order diffracted light was monitored and relative intensity was calculated by normalizing the diffracted beam intensity with the incident beam intensity. In order to achieve RSM performance, instead of complete melting, the POA gratings were brought to a partial melting temperature (T_p) (Figure 3.2c) at a heating rate of 1 °C /s, and then held for at least a minute before natural cooling at a slower rate dictated by the thermal equilibration at room temperature (RT).

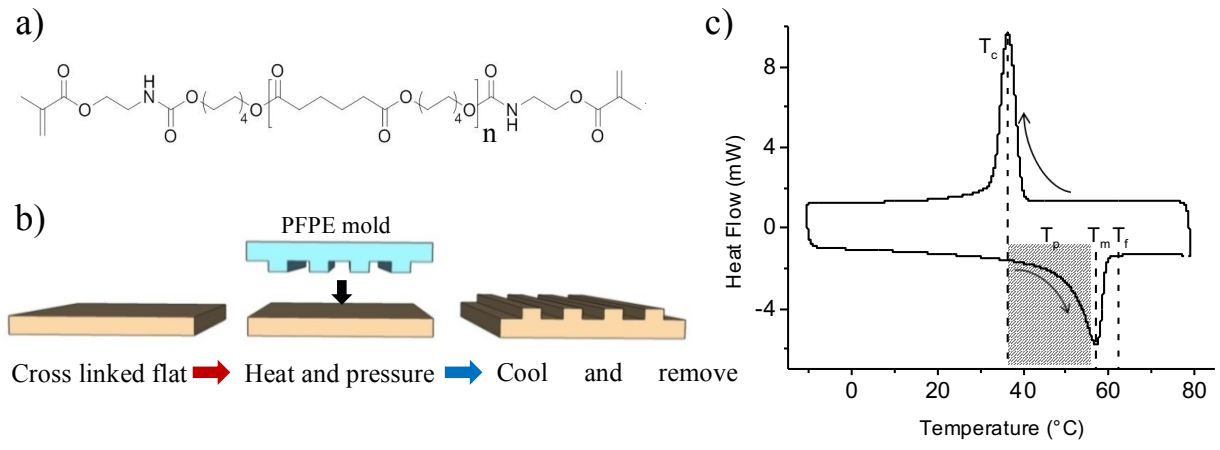

Figure 3.2 Synthesis and fabrication. a) Chemical structure of methacrylate-terminated poly(octylene adipate) (DP ≈ 13). **b)** The molding process: a glass slide is used to cure an optically flat surface of poly(octylene adipate). A 750 nm pitch perflouropolyether (PFPE) grating is used as a mold to emboss the heated flat surface. After cooling the mold is removed and the grating structure remains on the SMP surface. **c)** A differential scanning calorimetry (DSC) thermogram of a crosslinked POA sample indicates the temperature range of partial melting temperatures (T_p ,hatched region), the melting peak (T_m = 56 °C), the temperature of complete melting (T_f= 64 °C), and the crystallization peak (T_c = 37 °C) (arrows indicate ramping direction).

3.3 Results and discussion

3.3.1 Microscopic and morphological characterization

Temperature-triggered variations of the grating topography were monitored *in situ* using an atomic force microscope (AFM) equipped with a heating-cooling stage. In previous work, the maximum reversibility of POA was achieved when the partial melting temperature T_p was close to the melting peak T_m.[16] In the present work, we have therefore recorded AFM measurements for the same maximum reversibility cycle ranging from RT to T_p = 56 °C. The ridge height was found to vary with temperature, while all other grating parameters remained constant. Figure 3.3a-c shows the first heat-cool cycle from an as-prepared grating structure, Figure 3.3d-e shows the second heat-cool cycle, indicating a good repeatability. Average line profiles of the sample at 56 °C and after cooling to RT are shown in Figure 3.3f. Average ridge height analysis (Figure 3.4) of the line profiles shows the height reversibility is around 26% (Figure 3.3g). This microscopic reversibility of the grating feature is less than the bulk reversibility (~ 41%) of a polymer film when subjected to 15% uniaxial strain deformation. The discrepancy between bulk and microscopic reversibility may be due to plastic deformation and crystallization. We ascribe the observed plastic deformation to the non-uniform strain distribution generated by the

embossing process used for shape programming, which possibly induced the non-erasable grating artifacts present in a few locations even after complete sample melting at 80 °C (Figure 3.5). In addition, we know from previous work that freshly molten chains tend to recrystallize into large spherulites (~ 10 μm),[16] which interfere with crystallization in the nanoscale confinement of the grating and form an imperfect surface structure.

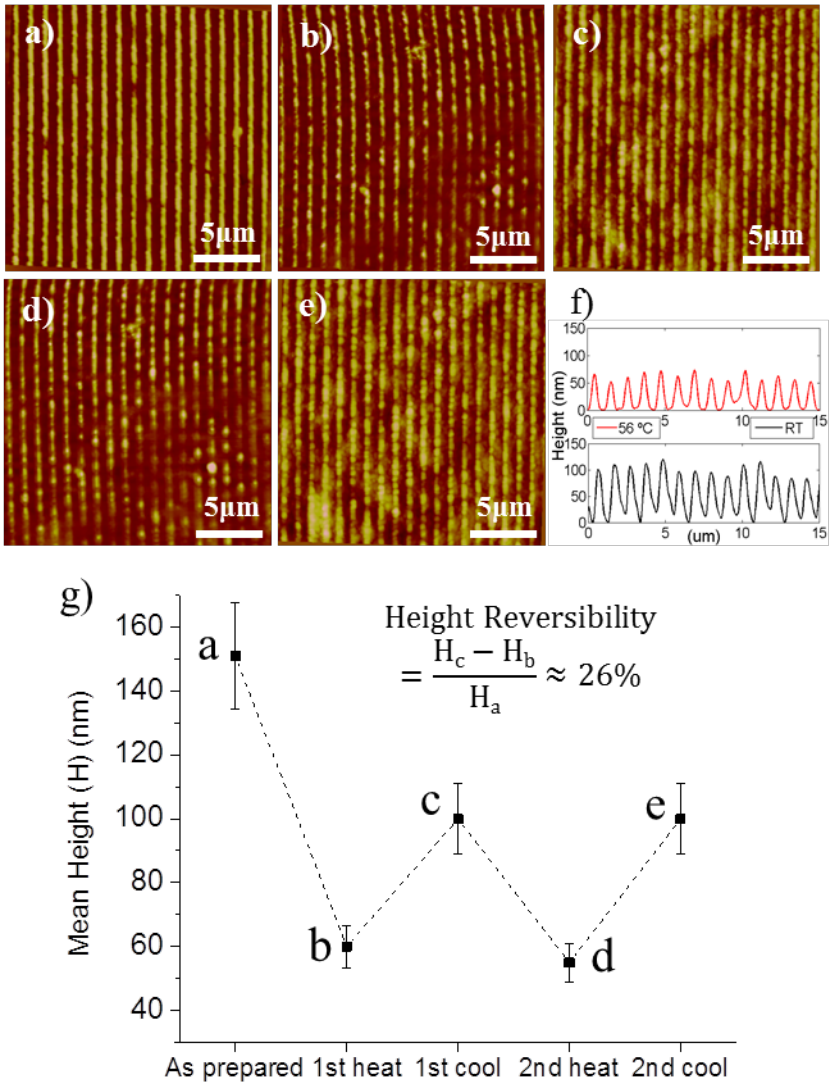

Figure 3.3 AFM morphological studies. AFM images **a)** as prepared and at room temperature, **b)** after heating to 56 °C at 1 °C/s and **c)** after cooling back to room temperature. **d)** Second heating to 56 °C at 1 °C/s **e)** and after subsequent cooling back to room temperature. (all scale bars are 5 μm) **f)** Height averaged line profile of the sample during one heating cycle, (top) at

56 °C and (bottom) cooled to RT. **g)** The corresponding AFM mean ridge height was averaged over 180 line profiles per AFM image. The height reversibility is calculated using the mean heights of corresponding AFM images.

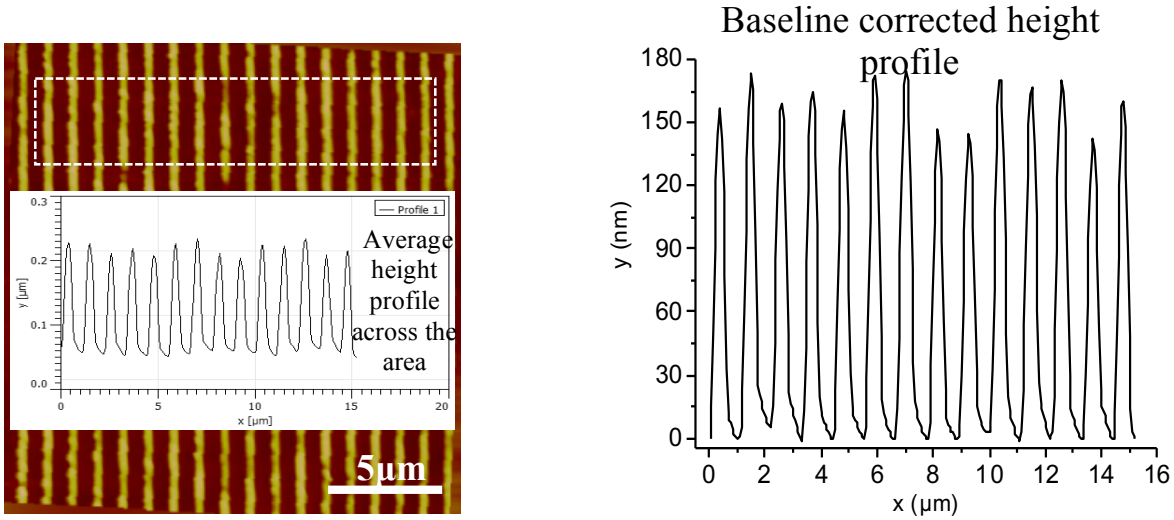

Figure 3.4 AFM height analysis of grating topology. A cross-sectional area was chosen to be averaged and from this area 180 line profiles are averaged to compile the averaged line profile. The averaged line profile is then baseline corrected and the average ridge height is calculated.

3.3.2 Reversible optical properties

Variations in the optical properties of the RSM grating due to the observed change in surface topography were explored. Figure 3.6a depicts a reversible change in diffraction intensity upon the corresponding variation in substrate temperature (Figure 3.2a, Region 1). Before reaching 40 °C, the change in intensity is minimal. This finding agrees with the previous results indicating that the onset of shape recovery occurs only after melting of at least ~ 10% wt/wt of the initial crystallinity.[16] Above 40 °C, the diffraction intensity begins to decrease due to the onset of shapeshifting (Figure 3.3b). Upon continued heating to a partial melting temperature T_p = 42 °C, the diffraction intensity continues to decrease. Upon cooling, the intensity recovers towards its initial value at RT (Figure 3.5a), indicating good optical reversibility (Figure 3.5b).

When a POA grating is heated to a higher temperature (T_p = 52 or 56 °C), the observed intensity modulation increases as well (Figure 3.5b). For each T_p, we heated and cooled a single POA grating sample multiple times between RT and T_p, and observed that the intensity change was repeatable over multiple cycles. Typical experiments included 2-3 cycles per temperature, with less than 5% variation in optical intensity. Further cycling at a single T_p resulted in a loss of ~10% of optical intensity over 25 cycles. In Figure 3.6a, only one cycle for each T_p is shown for clarity. By varying T_p, we located the optimal melting temperature to maximize reversibility: The maximum optical reversibility is ~ 36% and is found when partial melting T_p = 56 °C, which is near the T_m (Figure 3.2c), and is consistent with previous a RSM study.[14] As we will explain later, when a sample is heated to $T_p > T_m$ the grating is largely erased and the shapeshifting process is non-reversible.

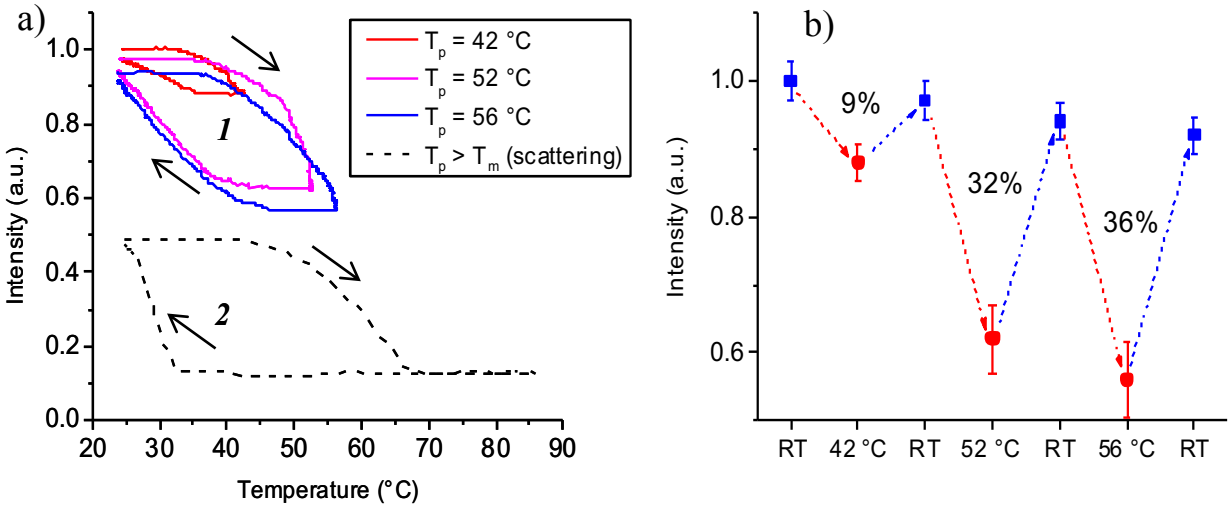

Figure 3.5 Optical reversibility. a) Optical intensity of a diffraction spot as temperature was varied (arrows showing ramping direction). Region 1: Optical intensity can be reversibly controlled within different cycles with T_p kept below T_m. Region 2: When T_p is increased above T_m, the grating is greatly erased and non-recoverable. The intensity drops significantly as the temperature increases to T_f. Now the surface returns to its flat primary shape and the intensity

changes upon cycling are due to melting/crystallization-induced scattering. **b)** Optical reversibility was calculated for three T_p cycles. A maximum optical reversibility of 36% was achieved when T_p was set at 56 °C, which is close to T_m.

The optical reversibility (OR) (Figure 3.5b) is calculated using the following equation:

$$OR = \frac{I_{RT,end} - I_{T_p,partial\ melt}}{I_{RT,start}} \quad (1)$$

Where $I_{RT,start}$ is the intensity of diffracted light (1st diffraction order) by the grating at room temperature before heating; $I_{T_p,partial\ melt}$ is the intensity of the diffracted light at a temperature of partial melting (T_p); $I_{RT,end}$ is the intensity after cooling back to room temperature. The 1st diffraction order was measured at 68° from the grating normal, and it was more than 10 times brigther than light detected in other directions due to some minor random scattering. Therefore, the observed optical reversibility is mainly attributable to changes in height of the grating ridges as a result of RSM behavior. As the temperature increases, a sufficient amount of crystalline scaffold has melted, which causes the grating to return towards its flat primary shape., Within the range $T_p < T_m$, enough crystallites remain to recover the embossed secondary shape upon cooling through self-seeded recrystallization, and the diffraction efficiency shows excellent reversibility and good repeatability over multiple cycles. Therefore by referring to T_m, as an upper temperature and lower grating height limit, a proper programing protocol can be determined for a desired reversible photonic actuation. The intensity never returns completely to the as-prepared programmed shape due to partial relaxation of the chemical network during recrystallization after each heat-cool cycle. Note that the strained chemical network always tends to return to its equilibrium unperturbed state (primary shape). However, the natural trend of thermodynamic equilibration is reversed by the kinetics of biased

recrystallization of the constrained network strands, which is biased by the remaining crystallites carrying the memory of the programmed secondary shape.

When $T_p > T_m$, the POA grating enters a new behavior regime: the optical intensity decreases below Region 1 and enters the curve of Region 2 (Figure 3.5a). In this regime a majority of the crystallites have melted, allowing the chemical network to relax to its thermodynamically preferred shape dictated by the chemical crosslinks and causing the sample to return towards its flat, primary shape. The grating is largely destroyed and non-recoverable. Upon heating to T = 85 °C, the programmed grating feature is largely destroyed with only some small residues of grating structure (less than 10 µm x 10 µm over a 50 µm x 50 µm scan window) (Figure 3.6) and the surface returns to its original flat morphology. The optical intensity drops to a minimum value dictated by intrinsic scattering in the substrate.

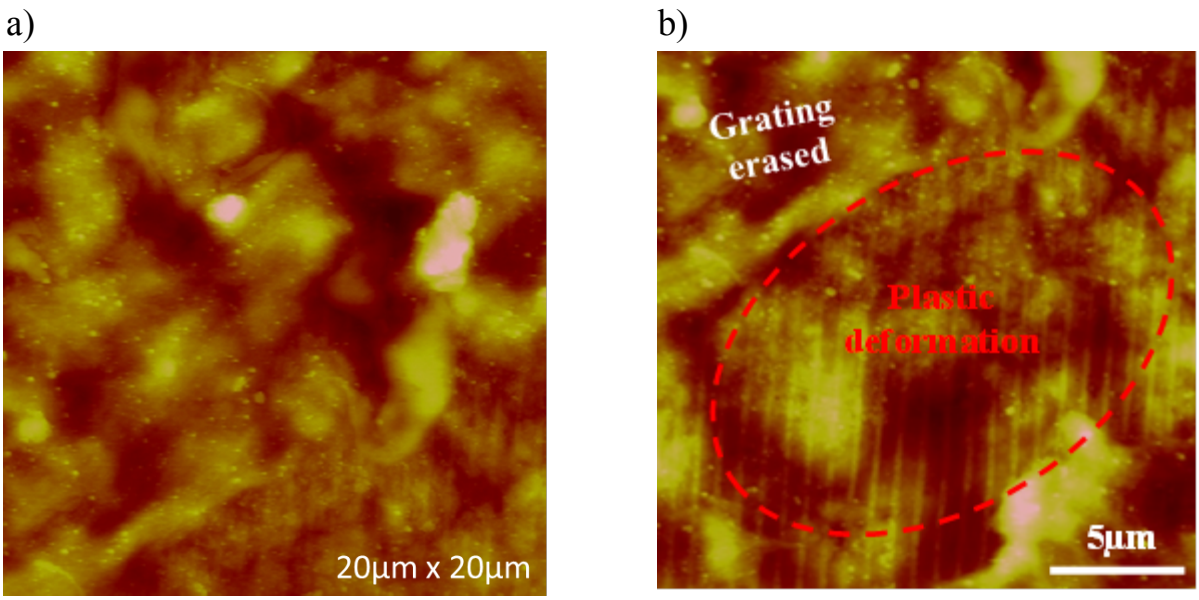

Figure 3.6 AFM morphology upon complete melting. An SMP piece was heated to 80 °C, a complete melting temperature, then cooled back to RT. Most gratings structures were erased and surface returned to the original shape **a)**, however a few spots turned out to remain grating

structure due to plastic deformation **b)**. The crystallization induced random roughness on the erased area was also observed.

3.3.3 Separation of diffraction and scattering

In Figure 3.5a Region 2, the optical response appears to be comparable in magnitude to that of Region 1, but the distribution of the detected light is different for both regions. In Region 2, the sample has been heated beyond T_m and the periodic grating is completely destroyed, so the majority of the light is simply reflected by a flat melted surface in a specular fashion, missing the detector still located where the 1st diffraction order used to propagate (Figure 3.7c). When the sample is cooled from its fully melted state, the intensity increases when $T_c = 37$ °C is reached, and the sample undergoes a random crystallization without trace of any shape memory effect. This random crystallization gives rise to pronounced light scattering in all directions including that of the detector (Figure 3.7d). As the surface becomes optically rough, the light that was previously diffracted and reflected now contributes to the scattered light. Intensity contributions from residual grating due to plastic deformation are minor, as the areas are randomly distributed over the entire sample and constitute a small percentage of surface (<10%). It should be noted that this behavior is in distinct contrast with the modulation in Region 1, where the grating exists at all times and the bulk of the detected light is the 1st diffraction order with a minimal contribution from scattered light (<10%) (Figure 3.7). We have conducted a separate study to distinguish individual contributions from diffraction and scattering while a grating is present. The random scattering contribution in Region 2 is due to polymer crystallization yielding a heterogeneous assembly of randomly oriented crystallites with a size distribution ranging from 10 to 1000 nm. This resulted in isotropic scattering, with minor variances of 1-2% observed. This result may offer an alternative way to study crystallization-induced surface roughness.

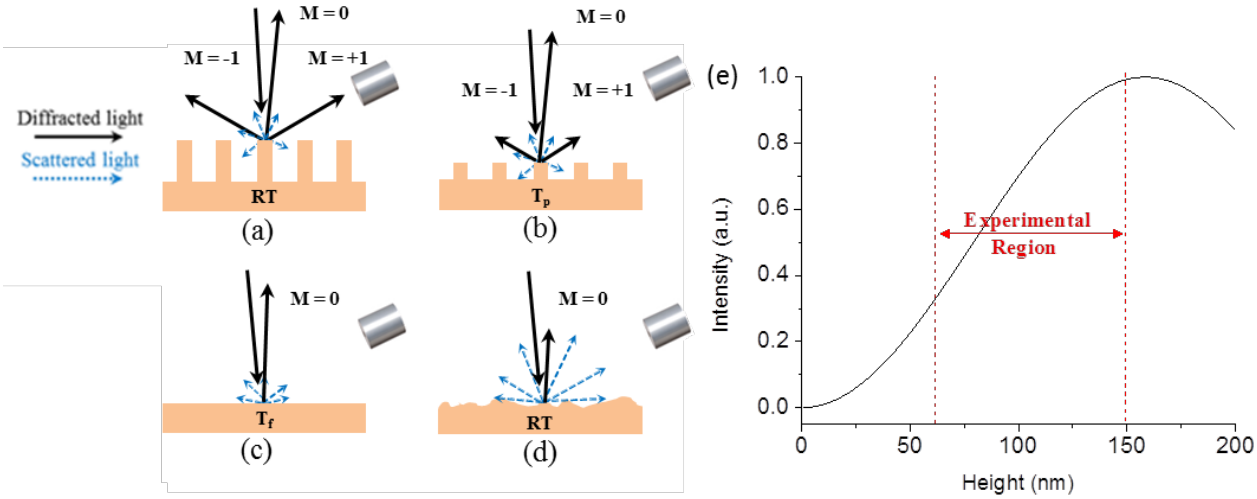

Figure 3.7 Schematic set-up and theoretical calculations. The diffraction and scattering intensity change with temperatures. The 1st diffraction order was monitored as the grating was cooled to RT **a)** and heated to a partial melting temperature T_p **b)**. Length of arrow indicates relative intensity which relates with grating's height. **c)** At T_f the surface returns to optically flat, detector only picks up scattering signal and when cooled back to RT **d)**, crystals form in an unrestricted fashion, resulting in an optically rough surface that more readily scatters light. **e)** Theoretical calculations indicate a sine-squared relationship between grating height and grating efficiency between 10 nm and 200 nm. As grating height decreases from ~150 nm to 60 nm, the measured intensity should decrease near linear fashion.

3.3.4 Theoretical diffractive mode intensity

The magnitude of the diffraction intensity change can be understood by analyzing the effect of the grating height. When a monochromatic laser beam is incident on a reflective diffraction grating surface, the reflected light interferes in a phase sensitive manner that depends on the grating spacing, height, and overall geometry; and produces a series of bright diffraction modes. For an ideal diffraction grating, the intensity of 0th and 1st order diffraction modes can be represented by Equations (2) and (3), respectively.[23]

$$I_0 \propto \cos^2(2\pi\delta / \lambda) \qquad (2)$$

$$I_1 \propto \sin^2(2\pi\delta / \lambda) \quad (3)$$

δ is the height of the grating, and λ is the wavelength of the laser beam. Figure 3.7e shows that the diffraction efficiency of 1st order diffraction mode increases with the grating height monotonically when the height is below 160 nm, which offers a wide operation range for a possible application. When the RSM grating is heated, its ridges decrease in height, reflecting weaker 1st order diffraction mode and higher 0th order diffraction mode. The slightly nonlinear optical response of the simulated grating efficiency, may contribute to the discrepancy between the height and optical reversibility.

3.4 Conclusion and outlook

Reversible shape memory (RSM) has been utilized to precisely replicate and control the shape of sub-μm features used in optical applications. This was determined by monitoring the diffraction efficiency as the patterned RSM substrate was subjected to heat-cool cycles, within the range $T_p < T_m$. The maximum optical reversibility was determined to be 36% when T_p is near T_m = 56 °C. The diffraction intensity can be controlled and always returns within 10% of the original intensity, unless $T_p > T_m$. The approach presented for the fabrication of the gratings can be applied to more complicated optical nanostructures for use in optical analytical equipment such as active blazed gratings. Furthermore, monitoring optical scattering intensity was also found to be a viable way to observe melting and crystallization induced roughness on the surface of semi-crystalline polymers. Additional studies need to be performed to determine relationships between crystallite size and scattering effects.

3.5 REFERENCES

1. Tippets, C. A.; Li, Q.; Fu, Y.; Donev, E. U.; Zhou, J.; Turner, S. A.; Jackson, A.-M. S.; Ashby, V. S.; Sheiko, S. S.; Lopez, R., Dynamic Optical Gratings Accessed by Reversible Shape Memory. *ACS applied materials & interfaces* **2015,** *7* (26), 14288-14293.

2. Aschwanden, M.; Beck, M.; Stemmer, A., Diffractive transmission grating tuned by dielectric elastomer actuator. *IEEE Photonics Technology Letters* **2007,** *19* (14), 1090-1092.

3. Ouyang, G.; Wang, K.; Henriksen, L.; Akram, M.; Chen, X., A novel tunable grating fabricated with viscoelastic polymer (PDMS) and conductive polymer (PEDOT). *Sensors and Actuators A: Physical* **2010,** *158* (2), 313-319.

4. Truxal, S.; Tung, Y.-C.; Kurabayashi, K. In *A PDMS-on-silicon deformable grating for spectral differentiation of mixed wavelength signals*, TRANSDUCERS 2007-2007 International Solid-State Sensors, Actuators and Microsystems Conference, IEEE: 2007; pp 1087-1090.

5. Werber, A.; Zappe, H., Tunable microfluidic microlenses. *Applied optics* **2005,** *44* (16), 3238-3245.

6. Xie, T., Recent advances in polymer shape memory. *Polymer* **2011,** *52* (22), 4985-5000.

7. Liu, Y.; Lv, H.; Lan, X.; Leng, J.; Du, S., Review of electro-active shape-memory polymer composite. *Composites Science and Technology* **2009,** *69* (13), 2064-2068.

8. Behl, M.; Razzaq, M. Y.; Lendlein, A., Multifunctional Shape-Memory Polymers. *Advanced materials* **2010,** *22* (31), 3388-3410.

9. Xie, T., Tunable polymer multi-shape memory effect. *Nature* **2010,** *464* (7286), 267-270.

10. Havens, E.; Snyder, E. A.; Tong, T. H. In *Light-activated shape memory polymers and associated applications*, Smart structures and materials, International Society for Optics and Photonics: 2005; pp 48-55.

11. Westbrook, K. K.; Mather, P. T.; Parakh, V.; Dunn, M. L.; Ge, Q.; Lee, B. M.; Qi, H. J., Two-way reversible shape memory effects in a free-standing polymer composite. *Smart Materials and Structures* **2011,** *20* (6), 065010.

12. Pandini, S.; Passera, S.; Messori, M.; Paderni, K.; Toselli, M.; Gianoncelli, A.; Bontempi, E.; Ricco, T., Two-way reversible shape memory behaviour of crosslinked poly (ε-caprolactone). *Polymer* **2012,** *53* (9), 1915-1924.

13. Chung, T.; Romo-Uribe, A.; Mather, P. T., Two-way reversible shape memory in a semicrystalline network. *Macromolecules* **2008,** *41* (1), 184-192.

14. Meng, Y.; Jiang, J.; Anthamatten, M., Shape actuation via internal stress-induced crystallization of dual-cure networks. *ACS Macro Letters* **2015,** *4* (1), 115-118.

15. Behl, M.; Kratz, K.; Noechel, U.; Sauter, T.; Lendlein, A., Temperature-memory polymer actuators. *Proceedings of the National Academy of Sciences* **2013,** *110* (31), 12555-12559.

16. Zhou, J.; Turner, S. A.; Brosnan, S. M.; Li, Q.; Carrillo, J.-M. Y.; Nykypanchuk, D.; Gang, O.; Ashby, V. S.; Dobrynin, A. V.; Sheiko, S. S., Shapeshifting: reversible shape memory in semicrystalline elastomers. *Macromolecules* **2014,** *47* (5), 1768-1776.

17. Espinha, A.; Serrano, M. C.; Blanco, Á.; López, C., Thermoresponsive Shape-Memory Photonic Nanostructures. *Advanced Optical Materials* **2014,** *2* (6), 516-521.

18. Turner, S. A.; Zhou, J.; Sheiko, S. S.; Ashby, V. S., Switchable micropatterned surface topographies mediated by reversible shape memory. *ACS applied materials & interfaces* **2014,** *6* (11), 8017-8021.

19. Xu, H.; Yu, C.; Wang, S.; Malyarchuk, V.; Xie, T.; Rogers, J. A., Deformable, programmable, and shape-memorizing micro-optics. *Advanced Functional Materials* **2013,** *23* (26), 3299-3306.

20. Wang, J.; Shao, J.; Wang, S.; He, H.; Fan, Z., Antireflective characteristics of triangular shaped gratings. *Chinese Optics Letters* **2005,** *3* (9), 497-499.

21. Chang, C.-H.; Heilmann, R.; Fleming, R.; Carter, J.; Murphy, E.; Schattenburg, M.; Bailey, T.; Ekerdt, J.; Frankel, R.; Voisin, R., Fabrication of sawtooth diffraction gratings using nanoimprint lithography. *Journal of Vacuum Science & Technology B* **2003,** *21* (6), 2755-2759.

22. Deka, B.; Sahu, P. P., Tooth-shaped grating-assisted structure for compact multimode interference coupler. *Applied Optics* **2011,** *50* (25), 193-199.

23. Chang, C.-L.; Acharya, G.; Savran, C. A., In situ assembled diffraction grating for biomolecular detection. *Applied physics letters* **2007,** *90* (23), 233901.

CHAPTER 4: HARD-TO-SOFT SEMI-CRYSTALLINE BOTTLEBRUSH NETWORKS[4]

4.1 Introduction and objectives

Hard-to-soft and soft-to-hard transition is ubiquitous in nature and vital for biology (echinoderms and reproductive organs),[1-8] food science (pasta, rice, corn),[9-11] and biomedical engineering (orthopedic casting).[12] Unlike solid-liquid transitions that lead to the loss of integrity and shape definition, the aforementioned applications rely on well-defined shapes, specific rigidity, and distinct functions in both the hard and the soft states. Typically, conventional hard-to-soft transitional organisms and materials demonstrate one to three orders of magnitude drop in modulus. For example, sea cucumber can demonstrate a modulus contrast between 50 MPa and 5 MPa,[13] semi-crystalline elastomers can change from GPa to MPa (Figure 2.9). However, for almost all dried polymeric networks and melts, there exists a lower modulus boundary on the order of 10^5 Pa, which is ascribed to polymer chains entanglement theory.[14-15] The design and manufacturing of materials with a modulus less than 10^5 Pa is not achievable without adding liquid to create polymer gels, which bring the challenge and the instability of swelling and deformation. Previous studies in our research group has shown that by employing bottlebrush structure, the network entanglements can be effectively eliminated and the material's modulus can be easily tuned to kPa range or even lower, without adding solvent.[14] Here, we endow a semi-crystalline polymer network with this new bottlebrush architecture. In this case, we can

[4]This chapter is in the process of patent application.

incorporate both the rigidity of crystalline state with a modulus on the order of GPa, and the softness of amorphous state with a modulus on the order of MPa, kPa or ever lower. The modulus drop becomes unprecedentedly huge, up to five-six orders of magnitude (from GPa to kPa). The stiffness enables high precision in materials' shape design, easy handling, penetration and piercing, while the softness can be adjusted to any softness of various bio-tissues (Figure 4.1).[16-17] In addition, unlike polymer gels, there is no incorporation of any type of solvent in the material, so there would be no volume change or phase separation upon the modulus transition.

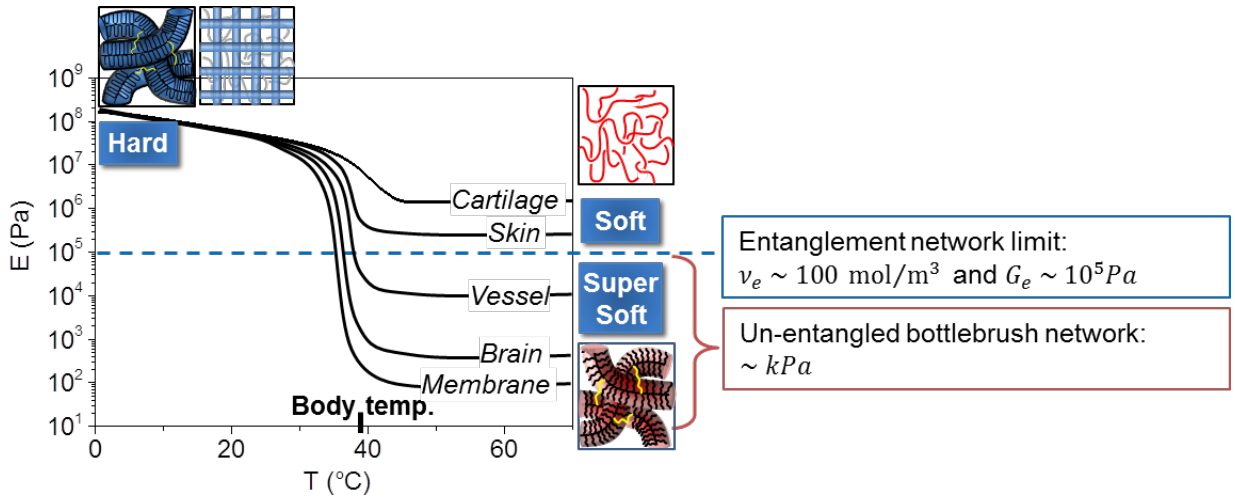

Figure 4.1 Modulus change with temperature of linear network and bottlebrush network. Above dashed line, linear semi-crystalline network demonstrates a typical modulus drop from GPa range to MPa range. Biological tissues such as cartilage and skin are located at MPa range. Due to the network entanglement, there is an intrinsic lower limit to linear network modulus, which is on the order of 10^5 Pa. By adopting bottlebrush architecture, the lower modulus can easily reach kPa range, or even lower down to hundreds of pascal. Many biological tissues are in this range, such as vessel, brain, and membrane.

The combination of rigidity and tissue-like softness of a dried polymeric material can benefit bio-medical implantation field dramatically. At room temperature, the material is expected to be "dormant" and rigid, which can be machined or programmed into a sharp shape;

upon insertion into body, the material warms up and melts, becoming as soft as surrounding tissues without any mechanical mismatch, diminishing interfacial scar tissue growth.[18-23] To bring bio-compatibility trait into our material, we choose FDA approved semi-crystalline poly(caprolactone) (PCL) to fabricate hard-soft semi-crystalline bottlebrush networks.[24] By varying the molecular weight of PCL, we can accurately control the melting transition, and adjust close to body temperature. Broadly speaking, all polymers with thermal transitions (T_g, T_c, T_m) are potential candidates for these kinds of heat-responsive modulus shifting.

We target two practical applications: brain implant and microneedles. Both cases require rigidity for penetration, and softness for tissue-compatibility. In addition, PCL demonstrates temperature related drug-diffusion property, namely, at crystalline state, drug diffuses very slow, whereas at amorphous state, diffusion becomes significantly fast.[25-26] This is especially ideal and useful for microneedle applications.

4.2 Experimental section

4.2.1 Materials

ε-Caprolactone, methacrylic anhydride (purity >97%), 4-Dimethylaminopyridine (DMAP), tin octoate, phenylbis(2,4,6-trimethyl-benzoyl)phosphine oxide, copper chloride, dichloromethane, dimethyl formaldehyde (DMF), tetrahydrofuran (THF), *p*-xylene (PX) were purchased from Aldrich and used as received. All other reagents and solvents were purchased from Aldrich and used as received without further purification.

4.2.2 One-end hydroxyl terminated PCL synthesis

In order to have a T_m around 37 ℃ (body temperature), we target to synthesize PCL with a molecular weight close to 1000 g/mol.[27] A solution of ethanol (1/*n* mol% with respect to *ε*-caprolactone, *n* is the target degree of polymerization) in *ε*-caprolactone (20 g, 175.22 mmol)

was prepared in an oven-dried flask. To the solution was added 3 Å molecular sieves and the mixture was dried for 48 h. The solution was filtered into a 250 mL round bottom flask using anhydrous toluene (20 mL) to aid in transferring the complete contents to the reaction vessel. Tin octoate (69 mg, 0.17 mmol) in 1mL of toluene was added via syringe. The reaction mixture was heated to 120 ℃. After 24 h of heating, the reaction was cooled to room temperature. THF (~10 mL) was added and the vessel sonicated to reduce the viscosity to a pouring consistency. The contents were then poured into methanol chilled in an ice bath to precipitate the polymer. The precipitation procedure was repeated two more times and the polymer was filtered and air dried, and then further dried under a vacuum to give ~19 g (>95% gravimetric conversion) of a white powder. ^{1}H-NMR is shown in Figure 4.2.

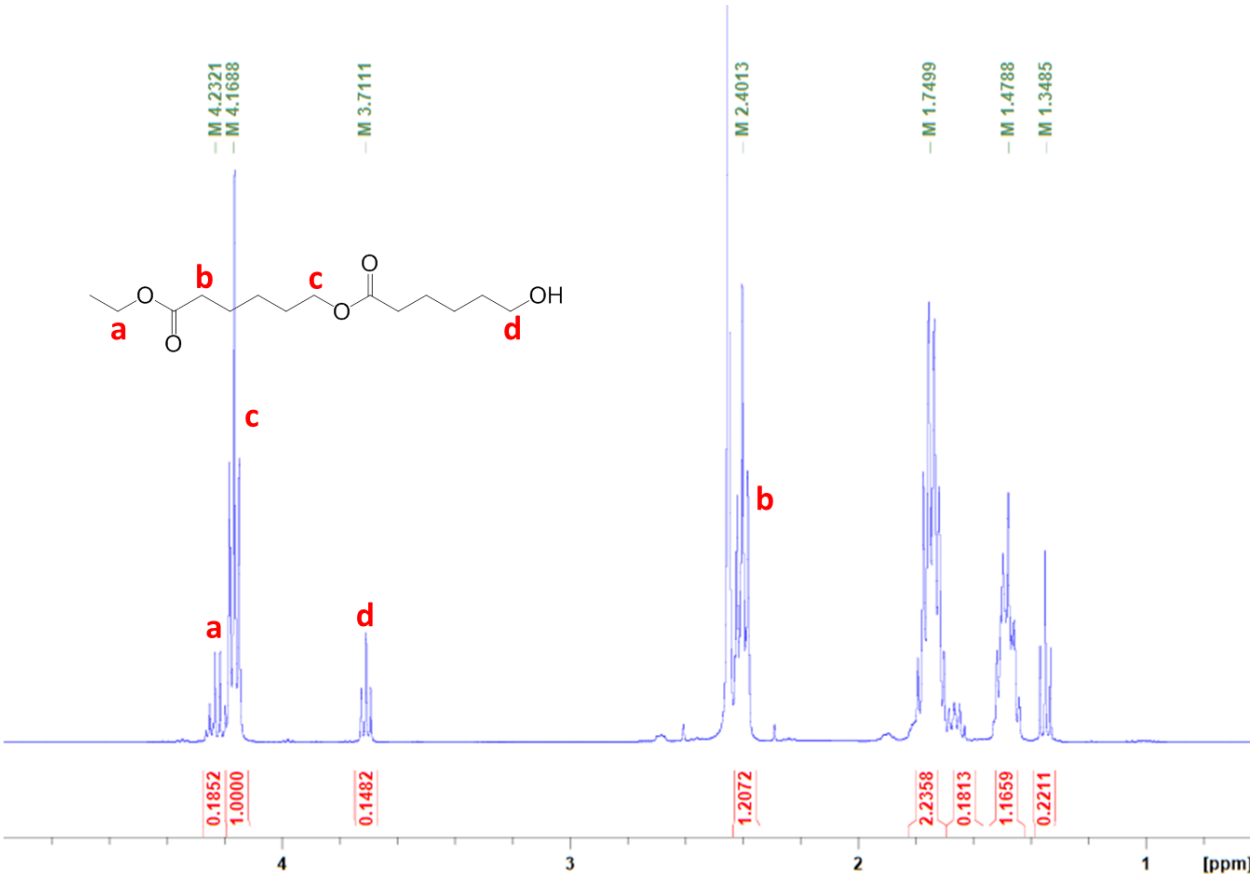

Figure 4.2 1H-NMR (400 MHz, $CDCl_3$) of one-end hydroxyl terminated PCL. Chemical structure is shown and related peaks are indicated in the figure. Degree of polymerization *n* is calculated as the ratio between integral of δ=4.17/ δ=3.71.

4.2.3 Both-end hydroxyl terminated PCL synthesis

The synthesis is similar to above procedure. Instead of ethanol, we used ethylene glycol to have two hydroxyl groups at each chain end. It is important for this polymer to have a molecular weight larger than two times of the mono PCL, because this both-end OH PCL will be later used as a crosslinker, which should have sufficient length to overcome steric hindrance. In this study, the crosslinker PCL was synthesized to be 4000 g/mol.

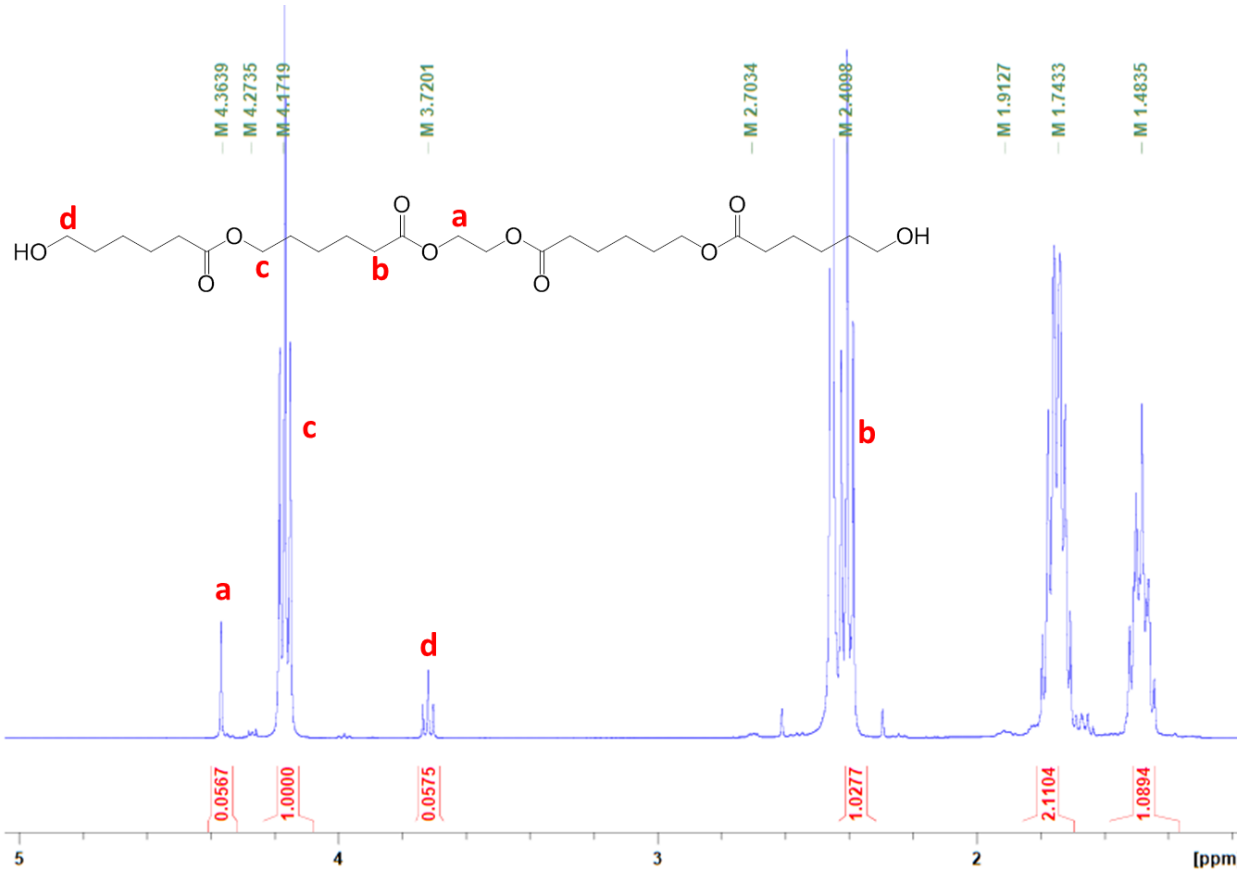

Figure 4.3 1H-NMR (400 MHz, $CDCl_3$) of both-end hydroxyl terminated PCL. Chemical structure is shown and related peaks are indicated in the figure. Degree of polymerization *n* is calculated as 2 times of the ratio between integral of δ=4.17/ δ=3.71.

4.2.4 End capping of PCL

Synthesized polymers are dissolved in anhydrous dichloromethane and 1.5 equivalents methacrylic anhydride and 2.0 equivalents DMAP respect to the hydroxyl group in polymer were added slowly while the solution stirring vigorously in an ice bath. The reaction continued for overnight. Then excess amount of CH_2Cl_2 was removed until the solution become very viscous, and then precipitated in cold methanol twice. The appearance of two peaks in 5.57 ppm and 6.11 ppm, and the disappearance in 3.71 ppm in 1H-NMR spectra of product showed that the successful end capping with methacrylate group.

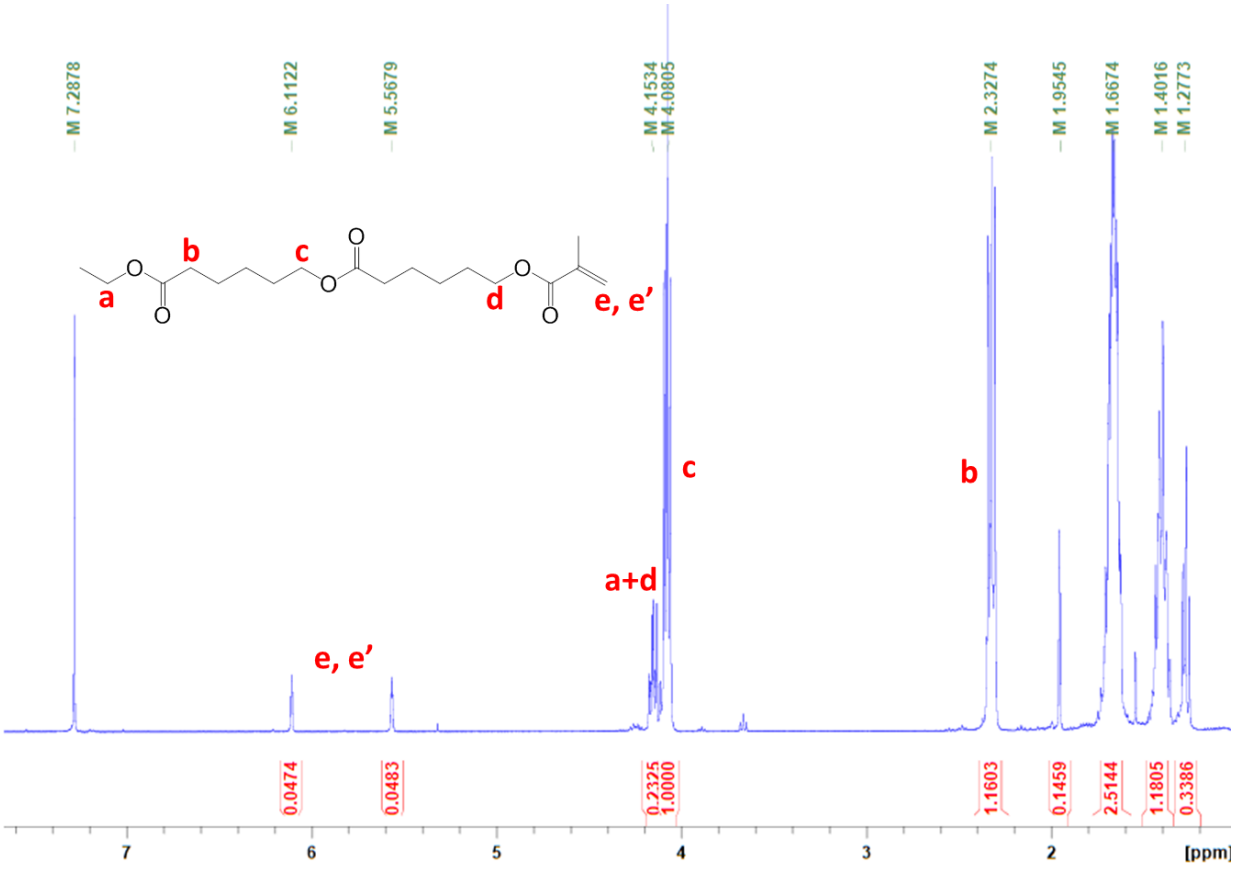

Figure 4.4 1H-NMR (400 MHz, $CDCl_3$) of mono-methacrylate capped PCL. The signature appearance of two peaks in 5.57 ppm and 6.11 ppm, and the disappearance in 3.71 ppm proved the successfully end-capping of hydroxyl group.

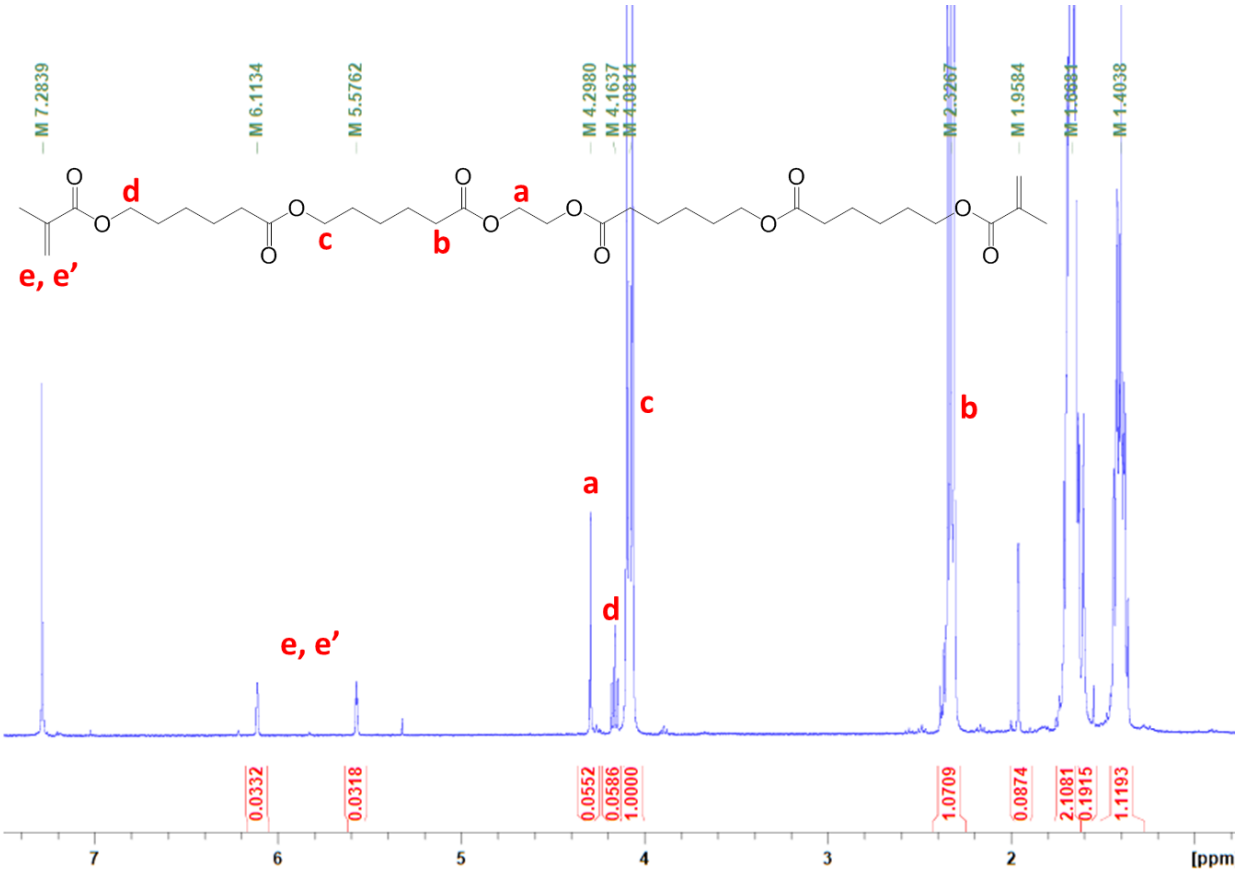

Figure 4.5 1H-NMR (400 MHz, $CDCl_3$) of both-methacrylate capped PCL. The signature appearance of two peaks in 5.57 ppm and 6.11 ppm, and the disappearance in 3.71 ppm proved the successfully end-capping of hydroxyl group.

4.2.5 Bottlebrush elastomer film and tube preparation

All elastomers were prepared by a one-step polymerization of monomethacryloxy terminated PCL with different molar ratios of both-end methacryloxy terminated PCL cross-linker as listed in Table 4.1. The initial reaction mixture contained 50 wt% of the monomers, 32 mg of phenylbis(2,4,6-trimethyl-benzoyl)phosphine oxide as photo-initiator, and 9 g of p-xylene as solvent. The mixtures of monomer, cross-linker and photoinitiator in p-xylene were bubbling in N_2 for 30 minutes. To prepare an elastomer film, the mixtures were injected between two glass plates with a 0.25, 0.5, 1.0 and 3 mm PDMS spacer. The elastomer films were then allowed to polymerize at room temperature under N_2 envrionment using a UV cross-linking chamber with

365 nm UV lamp for 12 hrs (0.1 mW/cm^{-2}, 10 cm distance). Elastomer tubes were prepared by injection of the above mixtures between two concentric cylindrical molds with inner and outer diameters of 2.0 mm and 4.0 mm respectively. The cylinders were then allowed to polymerize at similar condition as film preparation. Films and tubes were then swelled in chloroform in a glass petri dish. After every 8 hrs, the chloroform was replaced with fresh chloroform to remove unreacted monomers. Then, the samples were carefully deswelled with ethanol and dried in 50 °C oven. The conversion of monomers to elastomers (gel fraction) was measured by below equation and it was between 75 to 85 wt%. The fabrication process is shown in Figure 4.6.

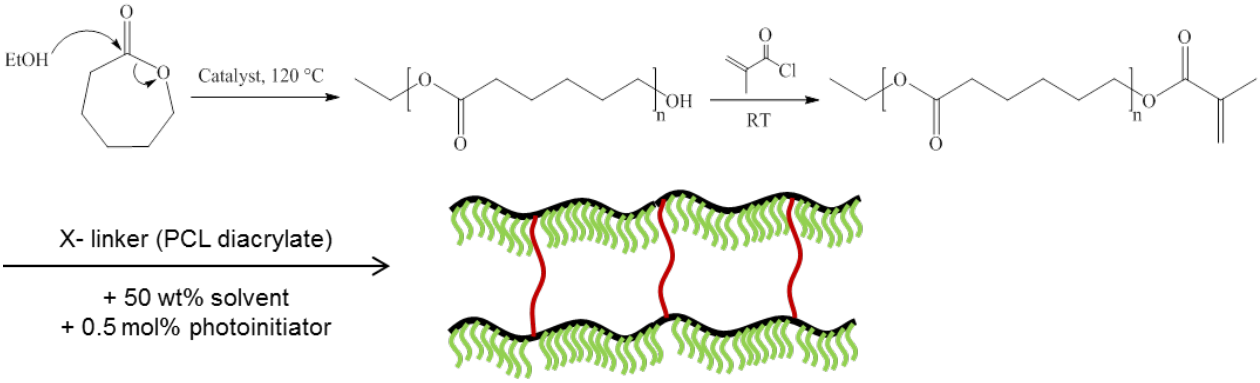

Figure 4.6 Synthetic route of PCL macromonomer and elastomer. A ring-opening polymerization was used to fabricate PCL macromonomer with desired molecular weight, and the elastomer was fabricated using UV assisted radical polymerization. Green strands represent PCL side chains, red strands represent PCL diacrylate crosslinkers, black strands represent methacrylate backbone.

4.2.6 Differential scanning calorimetry

A heat/cool/heat cycle with a ramp rate of 5 K/min from 0 °C to 80 °C was used for all samples by DSC 220 from Seiko Instruments, Inc. Second heating was used to determine the melting transition, while cooling was used to characterize the crystallization transition. The

crystallinity was calculated by the ratio of the integration of heating or cooling transition to the heat of fusion of caprolactone polymers, which is close to 150 J/g.[28]

4.2.7 Dynamic mechanical analysis

RSA-G2 dynamic mechanical analyzer from TA Instruments was used for mechanical tests. Before melting transition (T <36 °C), storage modulus was measured in oscillation mode at 1 Hz, 0.1% strain; after melting transition (T ≥36 °C), material become significantly softer, therefore higher strain was applied up to 5% in order to obtain an acceptable signal-noise ratio. Extensibility was measured at 80 °C with a constant strain rate of $2E^{-3}$/s.

Table 4.1 Composition and properties of PCL bottlebrush elastomer.

M_n (g/mol) [a]	Xlinker mol% [b]	$E_{0°C}$ [c] (Pa)	$E_{80°C}$ [d] (Pa)	T_c [e] (°C)	T_m [e] (°C)	ΔH_m [k] (J/g)
1000	0.25	7.6E8	4.4E3	4.4	35.0	57
	0.5	7.7E8	1.3E4	4.2	35.1	56
	1.0	7.3E8	3.4E4	3.8	36.1	56

[a] Side chain DP determined by H-NMR. [b] mole of PCL diacrylate / mole of side chain monomer. [c] measured by DMA at 0 °C, 0,1% strain, 1Hz. [d] measured by DMA at 80 °C, 2 % strain, 1 Hz. [e] measured by DSC at 5 °C/min second-heat/cool cycle. [k] calculated by DSC.

4.3 Results and discussion

4.3.1 From GPa to kPa

Poly(caprolactone), or PCL, is a very well-known and widely used semi-crystalline bio-degradable polymer. Depending on the molecular weight, its melting transition can be tuned within a broad range from 30 °C to 70 °C.[27] Typically, the higher the molecular is, the high T_m is.

For this study, we are targeting bio-medical applications, therefore it is necessary to tune the T_m close to body temperature. As shown in Figure 4.7, regardless of the crosslinker amount, all PCL bottlebrush network with 1000 g/mol PCL side chain show similar melting peaks, which are located near 36-37 °C. Note that we can easily tune T_m to be a higher value in case of other applications.

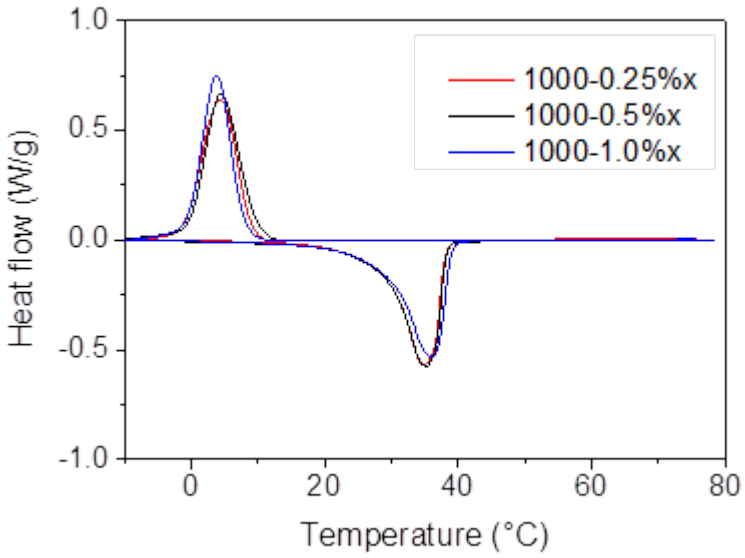

Figure 4.7 Melting and crystallization transition measured by DSC. Three polymers with different crosslinker usage showed similar melting transition around 37 °C and crystallization transition aroung 5 °C. The enthalpy is also similar, and it's calculated as the peak integration.

Like all semi-crystalline networks, PCL bottlebrush networks demonstrate a drop in modulus upon melting but with a considerably larger magnitude. As shown in Figure 4.8, at the crystalline state (0 °C), three PCL bottlebrush networks with different crosslinker amounts showed similar modulus 0.8 GPa, however, upon complete melting at 80 °C, they showed different modulus. The more crosslinker used, the higher the modulus is. As shown in Figure 4.8, 0.25% crosslinker sample shows the lowest modulus 4 kPa, whereas 0.5% crosslinker sample

shows 13 kPa and 1% crosslinker sample shows 34 kPa. In theory, the crosslinker usage should be proportional to the network modulus, as discussed in previous chapters. However in this case, we have to take into consideration of crosslinker conversion percentage, namely, not all crosslinker added were successfully incorporated into the network. Especially for 0.25% crosslinker usage, given that it is such a small amount of crosslinker, it is much more likely to obtain a network with lower gel-fraction. Regardless, all samples show transitions from GPa range to kPa range (six order or magnitude), and they all occur around body temperature.

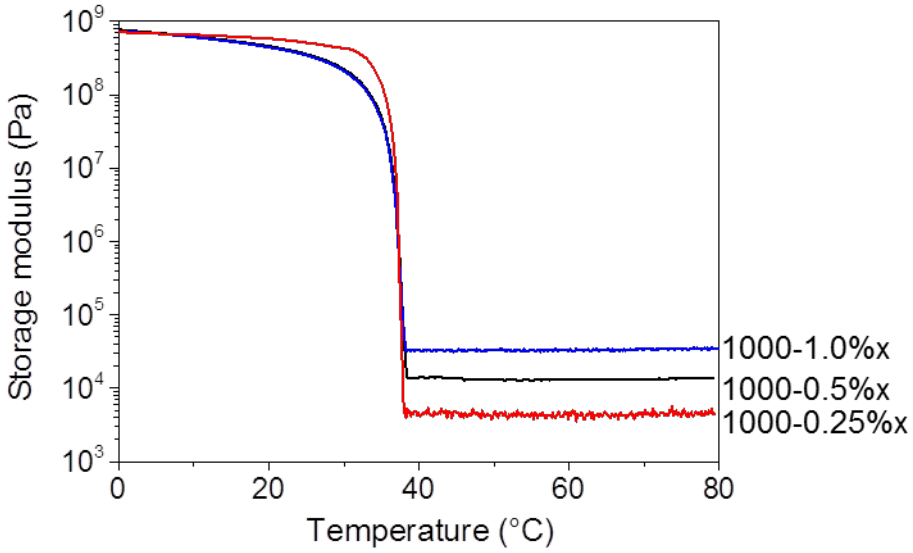

Figure 4.8 Storage modulus change with temperature measured by DMA. Starting from similar modulus around 0.8 GPa at 0 °C, three polymers all showed drop in modulus upon melting. The less amount of crosslinker, the lower the end modulus was. For 0.25% crosslinker sample, it showed the largest change in modulus, from 0.8 GPa to 4 kPa.

There are many materials possessing modulus-shifting properties, such conventional semi-crystalline elastomers, glassy linear polymer chains, hydrogels and composites. If we plot $G_{before\ transition}/\ G_{after\ transition}$, VS $G_{after\ transition}$, shown in Figure 4.9, we can see that PCL

bottlebrush clearly stands out with huge drop and low modulus after transition, and occupies an empty space where no other materials can achieve.[16-17, 29-46]

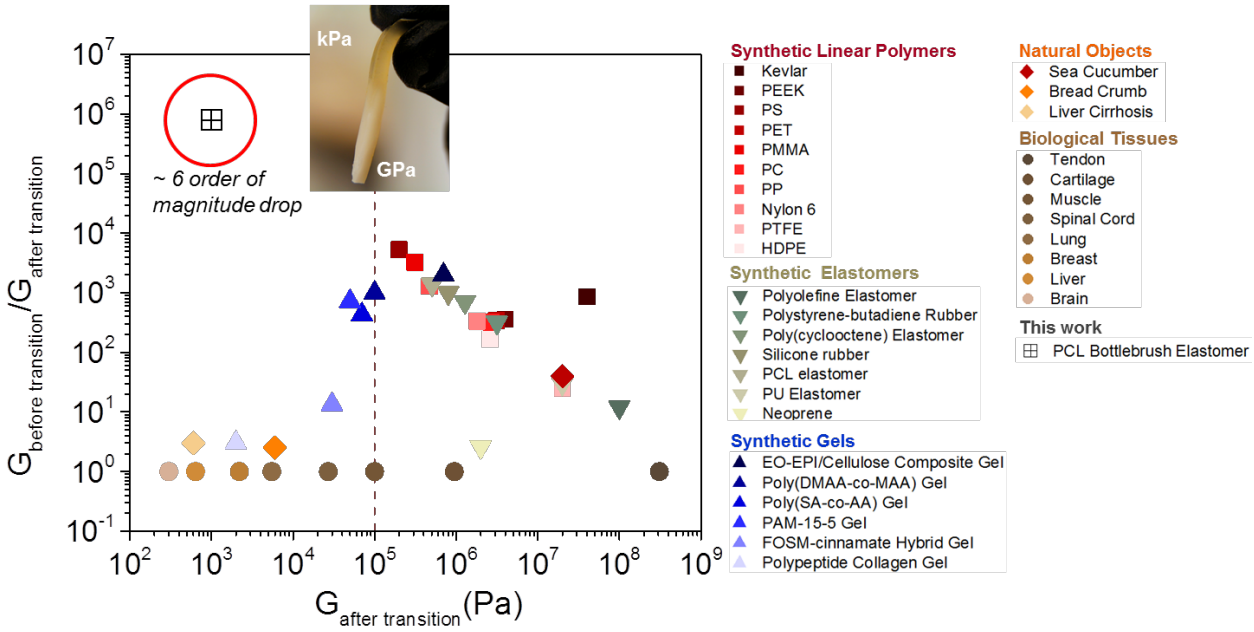

Figure 4.9 Comparison with other modulus changing materials. $G_{after\ transition}$ represents materials' high modulus before any modulus-dropping transition, such as melting transition, glass transition, or ionic interaction. $G_{after\ transition}$ represents materials' low modulus after the aforementioned transitions. Various groups of materials are listed, including synthetic linear polymers, elastomers, gels, and natural objects. Biological tissues don't possess modulus change, but are also listed as reference points. The PCL semi-crystalline bottlebrush elastomers show up to six orders of magnitude change in modulus, whereas all other materials show much less magnitude change. Also, to the left side of the dashed line, only hydrogels and PCL bottlebrush are able to match the exact modulus with soft tissues, whereas other synthetic dry materials fall to the right side of the dashed line. In the picture, the top section of the sample was heated to molten state, demonstrating kPa modulus, whereas the bottom section of the sample remained at its crystalline state, possessing GPa modulus.

4.3.2 Brain implants

A long-standing issue in brain implants, is the mismatch between the soft brain tissue (~500 Pa) and the rigid metal electrodes (GPa) that are widely used for deep brain stimulation.[22] Using the novel PCL semi-crystalline bottlebrush networks, we can fabricate a protection layer encapsulating the rigid electrodes inside. The material will serve both as a rigid shell for easy penetration at room temperature, and as a buffer layer segregating the rigid electrode and soft brain tissue. The material will have exactly the same softness as the brain after insertion, which can greatly reduce scar tissue growth and prolong the lifetime of the implant. A demo study is shown in Figure 4.10. We used thermocouple to represent the electrode, and a brain-shaped poly(acrylamide) hydrogel was synthesized with a modulus ~ 800 Pa to mimic brain tissue. As shown in the Figure 4.10, PCL semi-crystalline bottlebrush networks appear opaque, rigid and non-sticky at RT. After inserted into the pre-heated brain-gel (37 °C), the material became clear, significantly softer and sticky, securing the implant into the brain without mechanical mismatch. Further study will be conducted in a more realistic animal model.

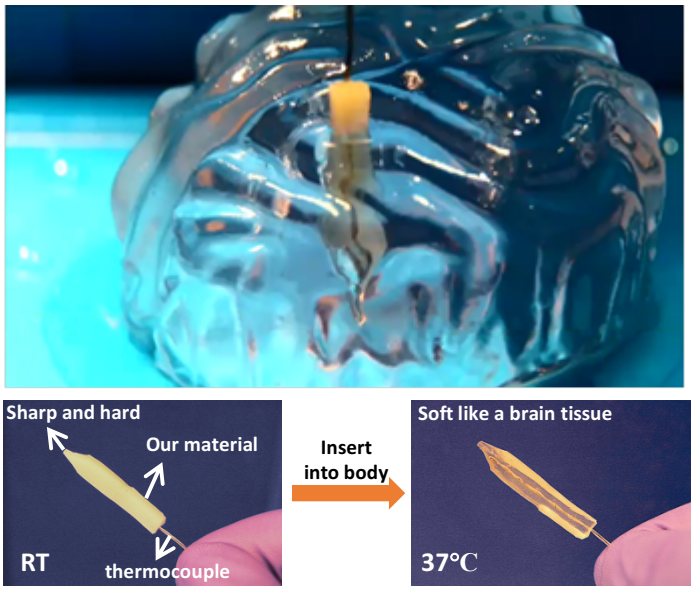

Figure 4.10 Brain implant demonstration. A polyacrylamide hydrogel with a modulus close to 500 Pa was fabricated with a brain-looking shape. The hydrogel has been preheated to body temperature. PCL semi-crystalline bottlebrush networks are used to encapsulate a rigid thermocouple. At room temperature, the material remains rigid and shape, and appear to be opaque. Upon insertion to the preheated brain gel, the material warms up, becoming as soft as the surrounding brain gel, sticky and hard to pull out. The thermocouple becomes visible as the material clears up.

4.3.3 Microneedles

Another application of hard-soft transition is the microneedles drug-delivery. Microneedles provide a novel transdermal drug delivery method, which can prolong drug-release and minimize pain sensation.[47-51] Silicone has been widely used for microneedle fabrication, as its rigidity helps to overcome skin-barrier.[52] However, due to the mismatch between the rigid needles and soft skin tissues, inflammation often occurs if the needles are kept for a long period of time.[53-54] Having the same modulus as soft skin and also having the rigidity to penetrate into skin, PCL semi-crystalline bottlebrush networks are great candidates for this application. There have been some works done on biodegradable PCL microneedles, and the drug release can be realized by heating-assisted diffusion behavior.[25-26, 55-57] However, these conventional PCL needles are not able to reach a modulus lower than 10^5 Pa, given their linear network topology. With the help of bottlebrush architecture, we aim to fabricate a new generation of microneedles with the exact modulus of soft skin tissues, which is expected to prolong the usage time and decrease discomfort to more extent.

As shown in Figure 4.11, at RT, the needles are dormant, rigid and drug-loaded. Upon patched onto skin, the needles become softer and sticky, and the drug start to diffuse out. This is an ongoing work, in future, we will systematically study release behavior and bio-compatibility.

In addition, PCL semi-crystalline bottlebrush networks shown great shape memory performance with high fixation ratio and recovery ratio. In future, we will combine this trait into applications as well.

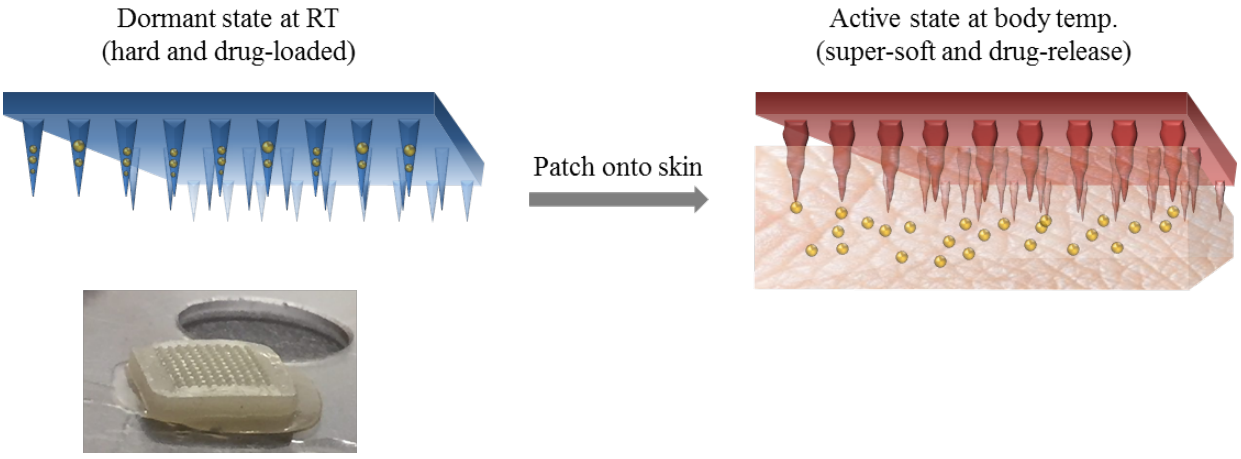

Figure 4.11 Microneedle concept and design. A PCL semi-crystalline bottlebrush network sheet has been programmed by compressing against a microneedle-shaped silicone mold (purchased from Micro-point Technologies) at molten state and then fixed by cooling. The dimensions are: needle height 800 μm, needle base 200 μm, needle pitch 680 μm. The sample with microneedle shape is shown in the picture. At room temperature, the sample remain dormant and hard, upon patching onto skin, the needles warm up and become as soft as skin, eliminating pain discomfort, and releasing the loaded drug.

4.4 Conclusion and outlook

In summary, we employed bottlebrush network architecture to the traditional semi-crystalline poly(caprolactone) elastomers. The synthesized material demonstrates huge modulus drop up to six order of magnitude, from GPa at room temperature (crystalline state), to kPa at body temperature (amorphous state). The uniqueness of both rigidity for easy handling and penetration and softness for tissue-mimicking makes this material a great candidate for many bio-medical applications. Also, like many semi-crystalline elastomers, this material shows great shape memory performance, which can further be tailored and adapted to specific applications.

In future, we will explore more practical applications using these materials, such as brain-implants, and microneedles.

Overall, semi-crystalline polymer networks are a promising and versatile group of functional materials. From traditional one-way irreversible shape memory, to two-way reversible shape memory, and to hard-soft bottlebrush networks, many interesting advances have been realized within this group of materials.

4.5 REFERENCES

1. Capadona, J. R.; Shanmuganathan, K.; Tyler, D. J.; Rowan, S. J.; Weder, C., Stimuli-responsive polymer nanocomposites inspired by the sea cucumber dermis. *Science* **2008,** *319* (5868), 1370-1374.

2. Russell, M.; Urbaniak, L.; Heinzeller, T.; Nebelsick, J. In *Does calcein affect estimates of growth rates in sea urchins?*, Echinoderms: Munchen: Proceedings of the 11th International Echinoderm Conference, 6-10 October 2003, Munich, Germany, CRC Press: 2004; p 53.

3. Motokawa, T., Effects of ionic environment on viscosity of Triton-extracted catch connective tissue of a sea cucumber body wall. *Comparative Biochemistry and Physiology Part B: Comparative Biochemistry* **1994,** *109* (4), 613-622.

4. Wilkie, I., Is muscle involved in the mechanical adaptability of echinoderm mutable collagenous tissue? *Journal of experimental biology* **2002,** *205* (2), 159-165.

5. Thurmond, F.; Trotter, J., Morphology and biomechanics of the microfibrillar network of sea cucumber dermis. *Journal of Experimental Biology* **1996,** *199* (8), 1817-1828.

6. Luo, H.; Goldstein, I.; Udelson, D., A three-dimensional theoretical model of the relationship between cavernosal expandability and percent cavernosal smooth muscle. *The journal of sexual medicine* **2007,** *4* (3), 644-655.

7. Venegas, J.; Sullivan, M.; Yalla, S. V.; Vickers, M., Assessment and modeling of the physical components of human corporovenous function. *American Journal of Physiology-Heart and Circulatory Physiology* **1995,** *269* (6), H2109-H2123.

8. Gefen, A.; Chen, J.; Elad, D., Stresses in the normal and diabetic human penis following implantation of an inflatable prosthesis. *Medical & biological engineering & computing* **1999,** *37* (5), 625-631.

9. Hammerle, J.; Mohsenin, N., Tensile relaxation modulus of corn horny endosperm as a function of time, temperature and moisture content. *TRANSACTIONS of the ASAE* **1970,** *13* (3), 372-0375.

10. Perdon, A.; Siebenmorgen, T.; Mauromoustakos, A., Glassy State Transition and Rice Drying: Development of a Brown Rice State Diagram 1. *Cereal Chemistry* **2000,** *77* (6), 708-713.

11. Takhar, P. S.; Kulkarni, M. V.; Huber, K., Dynamic viscoelastic properties of pasta as a function of temperature and water content. *Journal of texture studies* **2006,** *37* (6), 696-710.

12. Mihalko, W. M.; Beaudoin, A. J.; Krause, W. R., Mechanical properties and material characteristics of orthopaedic casting material. *Journal of orthopaedic trauma* **1989,** *3* (1), 57-63.

13. Trotter, J.; Tipper, J.; Lyons-Levy, G.; Chino, K.; Heuer, A.; Liu, Z.; Mrksich, M.; Hodneland, C.; Dillmore, W. S.; Koob, T., Towards a fibrous composite with dynamically controlled stiffness: lessons from echinoderms. *Biochemical Society Transactions* **2000,** *28* (4), 357-362.

14. Daniel, W. F.; Burdyńska, J.; Vatankhah-Varnoosfaderani, M.; Matyjaszewski, K.; Paturej, J.; Rubinstein, M.; Dobrynin, A. V.; Sheiko, S. S., Solvent-free, supersoft and superelastic bottlebrush melts and networks. *Nature materials* **2016,** *15* (2), 183-189.

15. Colby, R.; Rubinstein, M., Polymer physics. *New-York: Oxford University* **2003**, 274-281.

16. Levental, I.; Georges, P. C.; Janmey, P. A., Soft biological materials and their impact on cell function. *Soft Matter* **2007,** *3* (3), 299-306.

17. Wegst, U.; Ashby, M., The mechanical efficiency of natural materials. *Philosophical Magazine* **2004,** *84* (21), 2167-2186.

18. Harris, J.; Capadona, J.; Miller, R. H.; Healy, B.; Shanmuganathan, K.; Rowan, S. J.; Weder, C.; Tyler, D. J., Mechanically adaptive intracortical implants improve the proximity of neuronal cell bodies. *Journal of neural engineering* **2011,** *8* (6), 066011.

19. Moshayedi, P.; Ng, G.; Kwok, J. C.; Yeo, G. S.; Bryant, C. E.; Fawcett, J. W.; Franze, K.; Guck, J., The relationship between glial cell mechanosensitivity and foreign body reactions in the central nervous system. *Biomaterials* **2014,** *35* (13), 3919-3925.

20. Lee, H.; Bellamkonda, R. V.; Sun, W.; Levenston, M. E., Biomechanical analysis of silicon microelectrode-induced strain in the brain. *Journal of neural engineering* **2005,** *2* (4), 81.

21. Rohman, G.; Pettit, J. J.; Isaure, F.; Cameron, N. R.; Southgate, J., Influence of the physical properties of two-dimensional polyester substrates on the growth of normal human urothelial and urinary smooth muscle cells in vitro. *Biomaterials* **2007,** *28* (14), 2264-2274.

22. Sridharan, A.; Rajan, S. D.; Muthuswamy, J., Long-term changes in the material properties of brain tissue at the implant–tissue interface. *Journal of neural engineering* **2013,** *10* (6), 066001.

23. Roch, T.; Cui, J.; Kratz, K.; Lendlein, A.; Jung, F., Immuno-compatibility of soft hydrophobic poly (n-butyl acrylate) networks with elastic moduli for regeneration of functional tissues. *Clinical hemorheology and microcirculation* **2012,** *50* (1-2), 131-142.

24. Sun, H.; Mei, L.; Song, C.; Cui, X.; Wang, P., The in vivo degradation, absorption and excretion of PCL-based implant. *Biomaterials* **2006,** *27* (9), 1735-1740.

25. Chen, M.-C.; Ling, M.-H.; Wang, K.-W.; Lin, Z.-W.; Lai, B.-H.; Chen, D.-H., Near-infrared light-responsive composite microneedles for on-demand transdermal drug delivery. *Biomacromolecules* **2015,** *16* (5), 1598-1607.

26. Lao, L. L.; Venkatraman, S. S.; Peppas, N. A., Modeling of drug release from biodegradable polymer blends. *European Journal of Pharmaceutics and Biopharmaceutics* **2008,** *70* (3), 796-803.

27. Huang, Y.-p.; Xu, X.; Luo, X.-l.; Ma, D.-z., Molecular weight dependence of the melting behavior of poly (ε-caprolactone). *Chinese Journal of Polymer Science* **2002,** *20* (1), 45-51.

28. Flory, P.; Garrett, R.; Newman, S.; Mandelkern, L., Thermodynamics of crystallization in high polymers. Cellulose trinitrate. *Journal of Polymer Science* **1954,** *12* (1), 97-107.

29. Han, Y.; Bai, T.; Liu, Y.; Zhai, X.; Liu, W., Zinc ion uniquely induced triple shape memory effect of dipole–dipole reinforced ultra-high strength hydrogels. *Macromolecular rapid communications* **2012,** *33* (3), 225-231.

30. Skrzeszewska, P. J.; Jong, L. N.; de Wolf, F. A.; Cohen Stuart, M. A.; van der Gucht, J., Shape-memory effects in biopolymer networks with collagen-like transient nodes. *Biomacromolecules* **2011,** *12* (6), 2285-2292.

31. Hao, J.; Weiss, R., Mechanical behavior of hybrid hydrogels composed of a physical and a chemical network. *Polymer* **2013,** *54* (8), 2174-2182.

32. Gao, Z.; Varshney, S. K.; Wong, S.; Eisenberg, A., Block copolymer" crew-cut" micelles in water. *Macromolecules* **1994,** *27* (26), 7923-7927.

33. Yue, C.; Sui, G.; Looi, H., Effects of heat treatment on the mechanical properties of Kevlar-29 fibre. *Composites Science and Technology* **2000,** *60* (3), 421-427.

34. Kutty, S. K.; Nando, G. B., Short kevlar fiber–thermoplastic polyurethane composite. *Journal of applied polymer science* **1991,** *43* (10), 1913-1923.

35. Cheng, S. Z.; Wu, Z.; Mark, E., A high-performance aromatic polyimide fibre: 1. Structure, properties and mechanical-history dependence. *Polymer* **1991,** *32* (10), 1803-1810.

36. Zhang, Z.; Chen, X.; Wang, Y., Uniaxial ratcheting behavior of polytetrafluoroethylene at elevated temperature. *Polymer Testing* **2010,** *29* (3), 352-357.

37. Lagakos, N.; Jarzynski, J.; Cole, J.; Bucaro, J., Frequency and temperature dependence of elastic moduli of polymers. *Journal of applied physics* **1986,** *59* (12), 4017-4031.

38. Fetters, L.; Lohse, D.; Richter, D.; Witten, T.; Zirkel, A., Connection between polymer molecular weight, density, chain dimensions, and melt viscoelastic properties. *Macromolecules* **1994,** *27* (17), 4639-4647.

39. Everaers, R.; Sukumaran, S. K.; Grest, G. S.; Svaneborg, C.; Sivasubramanian, A.; Kremer, K., Rheology and microscopic topology of entangled polymeric liquids. *Science* **2004,** *303* (5659), 823-826.

40. Brown, J.; Ennis, B., Thermal Analysis of Nomex® and Kevlar® Fibers. *Textile Research Journal* **1977,** *47* (1), 62-66.

41. Chae, H. G.; Kumar, S., Rigid-rod polymeric fibers. *Journal of Applied Polymer Science* **2006,** *100* (1), 791-802.

42. The Engineering Tool Box Modulus of Elasticity or Young's Modulus - and Tensile Modulus for common Materials. http://www.engineeringtoolbox.com/young-modulus-d_417.html.

43. MatWeb, M. P. D. Tensile Property Testing of Plastics. http://www.matweb.com/reference/tensilestrength.aspx.

44. Corporation, M. E.-P. Thermal properties http://www.m-ep.co.jp/en/pdf/product/iupi_nova/physicality_04.pdf.

45. Poly-Tech PET (Thermoplastic Polyester). http://www.polytechindustrial.com/products/plastic-stock-shapes/pet-thermoplastic-polyester.

46. Plastics, P. Ketron PEEK 1000 Data Sheet,. https://www.professionalplastics.com/professionalplastics/KetronPEEK1000DataSheet.pdf.

47. Henry, S.; McAllister, D. V.; Allen, M. G.; Prausnitz, M. R., Microfabricated microneedles: a novel approach to transdermal drug delivery. *Journal of pharmaceutical sciences* **1998,** *87* (8), 922-925.

48. Park, J.-H.; Allen, M. G.; Prausnitz, M. R., Biodegradable polymer microneedles: fabrication, mechanics and transdermal drug delivery. *Journal of Controlled Release* **2005,** *104* (1), 51-66.

49. Kaushik, S.; Hord, A. H.; Denson, D. D.; McAllister, D. V.; Smitra, S.; Allen, M. G.; Prausnitz, M. R., Lack of pain associated with microfabricated microneedles. *Anesthesia & Analgesia* **2001,** *92* (2), 502-504.

50. Prausnitz, M. R., Microneedles for transdermal drug delivery. *Advanced drug delivery reviews* **2004,** *56* (5), 581-587.

51. Park, J.-H.; Allen, M. G.; Prausnitz, M. R., Polymer microneedles for controlled-release drug delivery. *Pharmaceutical research* **2006,** *23* (5), 1008-1019.

52. Lin, L.; Pisano, A. P., Silicon-processed microneedles. *Journal of Microelectromechanical Systems* **1999,** *8* (1), 78-84.

53. Bal, S. M.; Caussin, J.; Pavel, S.; Bouwstra, J. A., In vivo assessment of safety of microneedle arrays in human skin. *european journal of pharmaceutical sciences* **2008,** *35* (3), 193-202.

54. Liebl, H.; Kloth, L. C., Skin cell proliferation stimulated by microneedles. *Journal of the American College of Clinical Wound Specialists* **2012,** *4* (1), 2-6.

55. Chen, M.-C.; Wang, K.-W.; Chen, D.-H.; Ling, M.-H.; Liu, C.-Y., Remotely triggered release of small molecules from LaB 6@ SiO 2-loaded polycaprolactone microneedles. *Acta biomaterialia* **2015,** *13*, 344-353.

56. Nayak, A.; Das, D. B., Potential of biodegradable microneedles as a transdermal delivery vehicle for lidocaine. *Biotechnology letters* **2013,** *35* (9), 1351-1363.

57. Park, J.-H.; Davis, S.; Yoon, Y.-K.; Prausnitz, M. R.; Allen, M. G. In *Micromachined biodegradable microstructures*, Micro Electro Mechanical Systems, 2003. MEMS-03 Kyoto. IEEE The Sixteenth Annual International Conference on, IEEE: 2003; pp 371-374.